technische universität
dortmund

The Effect of Quantum Confinement on the Spin Properties of Lead Halide Perovskites Probed by Resonant Raman Spectroscopy

Carolin Sophie Harkort
2025

A document submitted in partial fulfillment of the requirements for the degree of
Doctor rerum naturalium
at
Fakultät Physik, Technische Universität Dortmund

Supervised by
Dmitri R. Yakovlev

Accepted by the Faculty of Physics of the TU Dortmund University, Germany.

Day of the oral examination: April 29th, 2025.

Examination board:
Dmitri R. Yakovlev
Doris E. Reiter
Jan Kierfeld
Dominik Mitzel

Abstract

Lead halide perovskites have emerged as exceptional semiconductor materials for photovoltaic and optoelectronic applications, offering easy tunability and lower production costs than conventional semiconductors. Their band gap energy can be adjusted through compositional changes, particularly by modifying the halide content, and through quantum confinement in low-dimensional systems. While the effects of composition and dimensionality on optical properties are well established, their influence on spin properties is far from being well understood. In this work, the technique of spin-flip Raman spectroscopy is employed to investigate three-, two-, and zero-dimensional lead halide perovskites, focusing on a key band structure parameter defining the coupling of spins to external magnetic fields: the Landé *g*-factor. In particular, the impact of quantum confinement on the carrier *g*-factor is examined in Ruddlesdon-Popper type two-dimensional perovskites and zero-dimensional $CsPbBr_3$ perovskite nanocrystals. The dependence of their *g*-factors on the effective band gap energy is compared to the universal dependence of the electron and hole *g*-factors in three-dimensional lead halide perovskites. This work reveals that while the general trend of both electron and hole *g*-factors follows the bulk dependence, significant deviations in their absolute values occur in two- and zero-dimensional lead halide perovskites, highlighting the pronounced impact of quantum confinement on spin properties. From a technological perspective, it is particularly interesting that the *g*-factor can be engineered by adjusting the number of inorganic layers in 2D perovskites or the size of the nanocrystals. Spin-flip Raman spectroscopy also reveals the domain structure of a bulk $MAPbI_3$ single crystal by identifying the presence of domains with different crystal orientations through the *g*-factor anisotropy. Furthermore, rare double spin-flip processes involving two electrons or two holes are detected. Next to spin-flip processes, confined acoustic phonon modes are discovered in the Raman spectra of $CsPbBr_3$ nanocrystals. A comparison of experimental results and density functional theory calculations enable the identification of these phonon modes and offers a complementary optical tool to probe structural properties such as the shape, structural phase, and size of the nanocrystals that are, in turn, key to understanding spin interactions.

Zusammenfassung

Blei-Halogen-Perowskite haben sich als herausragende Halbleitermaterialien für Photovoltaik- und Optoelektronik-Anwendungen etabliert, da sie im Vergleich zu konventionellen Halbleitern eine einfache Anpassbarkeit und geringere Produktionskosten bieten. Ihre Bandlückenenergie kann durch Kompositionsänderungen, insbesondere durch Modifikation des Halogens, und durch quantenmechanische Einschränkung in niedrigdimensionalen Systemen angepasst werden. Während die Auswirkungen der Zusammensetzung und Dimensionalität auf die optischen Eigenschaften weitestgehend bekannt sind, ist ihr Einfluss auf die Spin-Eigenschaften nicht vollständig verstanden. In dieser Arbeit wird die Technik der Spin-Flip-Raman-Spektroskopie verwendet, um drei-, zwei- und null-dimensionale Blei-Halogen-Perowskite zu untersuchen, wobei ein wichtiger Bandstrukturparameter im Fokus steht, der die Kopplung der Spins an äußere Magnetfelder beschreibt: der Landé *g*-Faktor. Besonders wird der Einfluss der quantenmechanischen Einschränkung auf den *g*-Faktor der Ladungsträger in zwei-dimensionalen Ruddlesdon-Popper Perowskiten und null-dimensionalen $CsPbBr_3$-Perowskit-Nanokristallen untersucht. Die Abhängigkeit ihrer *g*-Faktoren von der effektiven Bandlückenenergie wird mit der universellen Abhängigkeit der *g*-Faktoren von Elektronen und Löchern in dreidimensionalen Blei-Halogen-Perowskiten verglichen. Diese Arbeit zeigt, dass, obwohl der allgemeine Trend der *g*-Faktoren für Elektronen und Löcher der Bulk-Abhängigkeit folgt, signifikante Abweichungen in ihren absoluten Werten in zwei- und null-dimensionalen Blei-Halogen-Perowskiten auftreten, was den starken Einfluss der quantenmechanische Einschränkung auf die Spin-Eigenschaften verdeutlicht. Aus technologischer Sicht ist es besonders interessant, dass der *g*-Faktor durch Anpassung der Anzahl der anorganischen Schichten in 2D-Perowskiten oder der Größe der Nanokristalle gezielt eingestellt werden kann. Des Weiteren wird Spin-Flip-Raman-Spektroskopie verwendet um die strukturelle Domänenstruktur eines $MAPbI_3$-Einkristalls zu untersuchen und anhand einer *g*-Faktor-Anisotropie Bereiche mit unterschiedlichen Kristallorientierungen zu identifizieren. Darüber hinaus werden seltene Doppel-Spin-Flip-Prozesse beobachtet, in denen zwei Elektronen oder zwei Löcher involviert sind. Neben Spin-Flip-Prozessen werden in den Raman-Spektren von $CsPbBr_3$-Nanokristallen eingeschränkte akustische Phonon-Moden entdeckt. Ein Vergleich der experimentellen Ergebnisse mit Dichtefunktional-Berechnungen ermöglicht die Identifikation dieser Phonon-Moden und bietet ein ergänzendes optisches Werkzeug zur Untersuchung der Form, strukturellen Phase und Größe der Nanokristalle, die wiederum entscheidend sind, um Spin-Wechselwirkungen zu verstehen.

Contents

Introduction

Perovskite crystals refer to a broad class of materials with the general composition ABX_3, consisting of more than 300 known compounds, which include both fully inorganic and hybrid inorganic-organic structures, offering a variety of optical properties [1, 2]. This thesis focuses on hybrid organic-inorganic lead halide perovskites where A is an organic cation, such as methylammonium, B is lead, and X is a halide such as iodine or bromide. Lead halide perovskites have attracted significant attention in recent years due to their high performance in photovoltaic and light emitting applications [3, 4], as well as their remarkable optoelectronic properties, including a high light absorption coefficient and long carrier diffusion lengths [5, 6]. Prominent materials such as methylammonium and formamidinium lead iodide ($MAPbI_3$ and $FAPbI_3$) have driven a significant increase in the efficiency of prototype solar cells from 4% in 2009 [7] to 26% in 2021 [8, 9]. Recent technological achievements have opened up an interesting field of research on the fundamental aspects of light-matter interaction in lead halide perovskites, particularly focusing on the properties of excitons and photogenerated charge carriers near the band gap [10]. The optical properties of lead halide perovskites can be widely manipulated either through compositional engineering or by reducing the dimensionality to thin layers or nanocrystals [11, 12]. Beyond optoelectronic applications, lead halide perovskites are highly promising materials for spin-optoelectronic applications due to their unique properties: they consist of heavy-element components that enable significant spin-orbit coupling for efficient spin manipulation, they exhibit long spin relaxation times for efficient spin transport, and they demonstrate strong, tunable photoluminescence emission [13, 14]. While the influence of composition and dimensionality on the optical properties of this material class is well established, its fundamental spin properties are far from being fully understood. Recent studies have demonstrated that optical spin control in lead halide perovskites can be achieved similarly to conventional semiconductors [15]. This includes various optical and magneto-optical techniques such as optical orientation [16, 17], time-resolved Faraday/Kerr rotation [18, 19], and resonant spin-flip Raman spectroscopy [20]. Among these, spin-flip Raman spectroscopy is a powerful magneto-optical technique for analyzing the spin properties and interactions of charge carriers through inelastic light scattering, where the spin orientation of one or more charge carriers is inverted in the presence of a magnetic field [21]. This spin inversion is associated with an energy shift corresponding to the Zeeman energy. By using a narrow single-mode laser in combination with a high-resolution spectrometer, inelastic scattering processes with energy shifts as small as a few hundred of μeV can be explored. From the Zeeman energy, a key band structure parameter, the Landé g-factor, which characterizes the coupling of the spin to an external magnetic field, can be determined. Thus, this method provides direct insight into the Zeeman splitting of electrons, holes, and excitons, as well as their optical selection rules [22–24], enabling the determination of g-factors for all carriers within a single experiment [25]. Spin-flip Raman spectroscopy was first applied in 1968 on CdS to study bound electrons and holes [26]. Since then, the technique has been widely applied to investigate conventional semiconductors across various dimensionalities, such as quantum wells [24, 27], quantum dots [28–30], and colloidal nanoplatelets [31]. However, its application to lead halide perovskites has rarely been demonstrated so far. In this thesis, we apply spin-flip Raman spectroscopy to three-, two-, and zero-dimensional lead halide perovskites. Through systematic experimental investigations for different degrees of quantum confinement, a comprehensive picture of the

effect of quantum confinement on the spin properties of lead halide perovskites is established. Chapters 1 and 2 provide an overview of the theoretical background and experimental method of spin-flip Raman spectroscopy in lead halide perovskites. In the following, the experimental results, presented in Chapters 3 to 5 are set into context with existing literature.

$MAPbI_3$ is one of the most widely studied materials in the family of lead halide perovskites [2]. A detailed understanding of its structural microstructure is crucial for elucidating its intrinsic properties and potential applications in spintronics and related technologies [32]. Techniques such as atomic force microscopy (AFM) and scanning tunneling microscopy (STM) enable detailed analysis of a sample's structure and surface morphology [33, 34]. However, STM faces significant challenges when applied to lead halide perovskites due to their (semi-)conducting nature, which can affect the reliability of tunneling-based measurements [35]. Additionally, accurate surface characterization requires atomically flat surfaces, which are difficult to achieve with commonly used synthesis methods such as spin-coating [36]. Moreover, the strong electric field between the tip and the sample is sufficient to displace ions in the perovskite materials, leading to lattice distortions and potentially altering the material's intrinsic properties [36]. Therefore, an alternative experimental technique is needed that enables the structural analysis without modifying the sample's characteristics. In Chapter 3, we demonstrate that the technique of spin-flip Raman spectroscopy not only provides insights into the Zeeman splitting of carriers and their interaction but also serves as a powerful tool for investigating the structural domain orientation of a $MAPbI_3$ single crystal. Traces of different structural orientations are revealed through spin-flip lines that exhibit different g-factor anisotropies. Notably, the intensities of the electron and hole spin-flips from one structural domain are approximately an order of magnitude stronger than those from the other domain, indicating that the $MAPbI_3$ single crystals are primarily a single domain. Besides the presence of different structural domains, we observe strongly polarization-dependent spin-flip Raman scattering spectra for both the electron and hole. A systematic polarization analysis combining a four-level excitation scheme with resident carriers in the ground states and excited three-particle states, and a slightly tilted magnetic field from Faraday geometry successfully reproduces the main features of the strongly polarization-dependent spin-flip Raman spectra. This analysis provides further evidence that the observed spin-flips originate from resident carriers in the lead halide perovskite crystal and offers a powerful approach for determining the sign of g-factors in so far unexplored materials. In $MAPbI_3$, Zeeman splittings from double spin-flips (twice the electron and twice the hole Raman shifts) and combined electron-hole spin-flips have been observed. The observation of combined and double spin-flips is rare, as their intensities are approximately one order of magnitude lower than that of single spin-flips [31, 37].

While three-dimensional structures continue to attract interest, modern growth techniques, such as molecular beam epitaxy, enable the minimization of spintronic devices and the construction of nanostructures, thus opening up a new field of research and forming the basis of nanotechnology [38, 39]. The trend of downsizing materials from 3D to 0D serves as a bridge between bulk materials and atomic or molecular systems [40]. Quantum confinement affects not only the electronic and optical properties but also the spin properties [41]. Different low-dimensional structures, such as 2D materials and nanocrystals, can be formed depending on the degree of quantum confinement and the number of free dimensions. In zero-dimensional nanocrystals, the movement of electrons is confined within a volume, typically with a nanometer-sized diameter, resulting in a full quantization as in natural atoms [39]. Already in 1937, Herbert Fröhlich theoretically predicted that the size of the quantum dots would determine their optoelectronic properties [42]. However, the synthesis of quantum dots, discovered independently by two of three Noble Price winners in Chemistry in 2023, Louis Brus and Alexei Yekimov, was first established in the mid-1980s. With both techniques, Brus's wet-chemical method for solution-grown samples and Yekimov's high-temperature precipitation in a glass matrix, it was experimentally

observed that decreasing the quantum dot size leads to a shift of the emission to shorter wavelengths [43, 44]. However, these fabrication methods lacked control over the size and shape of the quantum dots. In 1993, Moungi Bawendi achieved a breakthrough by developing a synthesis method that allowed precise control over monodispersive quantum dots with well-defined size and shape [45], for which he was awarded a third share of the Nobel Prize. This innovation revolutionized the use of quantum dots, enabling applications such as laser diodes [46] and displays [47].

Lead halide perovskite nanocrystals are highly promising materials for spintronic applications due to their remarkable quantum yield of up to 90 %, broadly tunable photoluminescence through compositional changes and confinement of charge carriers [48, 49]. However, a significant limitation of lead halide perovskite nanocrystals is their low stability under ambient conditions [50], particularly for nanocrystals containing organic cations, which are highly volatile due to their hydrophilic nature [51, 52]. Consequently, all-inorganic caesium lead halide perovskites have garnered considerable attention. One effective approach to protect these nanocrystals from environmental degradation is to synthesize them within a glass matrix [53, 54]. A suitable option is the fluorophosphate glass matrix, which offers high chemical resistance to harmful environmental conditions and enables the incorporation of high concentrations of halides, thereby ensuring a high quantum yield of nanocrystals [55]. Spin-dependent phenomena in perovskite nanocrystals have been reported for lead halide nanocrystals synthesized with wet-chemical methods [56], as well as for those embedded in a glass matrix [51, 57, 58].

In conventional low-dimensional semiconductor systems, such as In(Ga)As quantum dots [59] and InAs nanowire quantum dots [60], it is well established that quantum confinement induces a renormalization of the g-factor [61]. Similarly, in lead halide perovskites, the effect of quantum confinement is expected to modify the spin properties. This thesis aims to investigate the Landé g-factors in two- and zero-dimensional lead halide perovskites and to explore their dependence on the effective band gap energy, which can be tuned not only through compositional changes but also through quantum confinement. In our group, it has been found that for bulk lead halide perovskites, the g-factors of both electron and hole exhibit a dependence on compositional changes, which can be described by a universal dependence on the band gap energy [62]. A conceptually different approach explored in this thesis is to tune the effective band gap energy through quantum confinement. This is particularly interesting for technological applications, as it enables the engineering of spin properties by the variety of perovskite materials and quantum confinement. Furthermore, this approach is more robust than compositional engineering, as only a limited number of lead-halide perovskite compositions demonstrate good quality in terms of crystal phase stability, moisture resistance, and toxicity [63–65]. To systematically study spin properties under the effect of quantum confinement, a variety of lead halide perovskites will be investigated using the technique of spin-flip Raman spectroscopy. In Chapter 4, the technique of spin-flip Raman spectroscopy is applied to 2D Ruddlesdon-Popper (RP) type perovskites, $PEA_2(MA, FA)_{n-1}Pb_nX_{3n+1}$, where X represents the halides bromide and iodine. Here, the impact of the quantum confinement on the carrier g-factors is investigated across a broad energy range from 1.8 eV to 3.1 eV by combining the results from the iodine and bromide material series. It is found that both the electron and hole g-factors deviate significantly from the bulk universal dependence, indicating that quantum confinement strongly influences the spin properties.

Building up on the investigations of the g-factor on the strength of quantum confinement, $CsPbBr_3$ nanocrystals grown in solution are investigated in Chapter 5. The nanocrystal ensemble provides information about the average spin properties and their dispersion due to inhomogeneous broadening [66]. By resonantly exciting subensembles, changes of the g-factors with the nanocrystal size can be measured. It has been found that both the electron and hole g-factors are strongly

affected by the quantum confinement and deviate from the bulk universal dependence. Besides the spin-flips of resident carriers, optically-active acoustic phonon modes confined in the nanocrystals were observed due to their interaction with photogenerated excitons in the resonant Raman spectra. The phonon Raman spectra exhibit a pronounced nanocrystal size dependence, establishing Raman spectroscopy as a highly important characterization tool for nanoparticles [67]. Confined acoustic phonons in semiconductor quantum dots were first reported in the mid-1990s, especially in CdSe nanocrystals embedded in glass [68] and CdS doped glasses [69], with additional studies in the early 2000s [70, 71]. However, experimental advancements in this field have not been reported for nearly two decades. The discovery of optically-active confined acoustic phonon modes in $CsPbBr_3$ nanocrystals has sparked new interest in this research topic. The investigation of the size-dependent behavior of acoustic phonon modes in $CsPbBr_3$ nanocrystals has been extended to include $CsPbI_3$ nanocrystals embedded in a glass matrix. A detailed analysis of the Raman spectra with density functional theory enables the computation of Raman spectra for optically-active confined acoustic phonon modes in nanocrystals of various shapes and structural phases. This approach provides a complementary optical method to probe structural properties such as the shape, structural phase, and size of nanocrystals through resonant Raman scattering, which are, in turn, key to understanding spin interactions.

List of publications

Part of the results presented in this thesis have been or will be published in the following articles:

E. Kirstein, E. A. Zhukov, D. R. Yakovlev, N. E. Kopteva, C. Harkort, D. Kudlacik, O. Hordiichuk, M. V. Kovalenko, and M. Bayer, "Coherent Spin Dynamics of Electrons in Two-Dimensional $(PEA)_2PbI_4$ Perovskites", Nano Letters **23**, 205 (2023)
DOI: 10.1021/acs.nanolett.2c03975

C. Harkort, D. Kudlacik, N. E. Kopteva, D. R. Yakovlev, M. Karzel, E. Kirstein, O. Hordiichuk, M. V. Kovalenko, and M. Bayer, "Spin-flip Raman Scattering on Electrons and Holes in Two-Dimensional $(PEA)_2PbI_4$ Perovskites", Small **19**, 2300988 (2023)
DOI: 10.1002/smll.202300988,

D. Kudlacik, N. E. Kopteva, M. Kotur, D. R. Yakovlev, K. V. Kavokin, C. Harkort, M. Karzel, E. A. Zhukov, E. Evers, V. V. Belykh, and M. Bayer, "Optical Spin Orientation of Localized Electrons and Holes Interacting with Nuclei in a $FA_{0.9}Cs_{0.1}PbI_{2.8}Br_{0.2}$ Perovskite Crystal", ACS Photonics **11**, 2757 (2024)
DOI: 10.1021/acsphotonics.4c00637

C. Harkort, I. V. Kalitukha, D. Kudlacik, N. E. Kopteva, D. R. Yakovlev, B. Turedi, D. N. Dirin, M. V. Kovalenko, and M. Bayer, "Spin-flip Raman scattering on electrons and holes in $MAPbI_3$ single crystals", In preparation (2025)

C. Harkort, I. V. Kalitukha, N. E. Kopteva, M. O. Nestoklon, L. S. Goupalov, L. Saviot, D. Kudlacik, D. R. Yakovlev, E. V. Kolobkova, M. S. Kuznetsova, and M. Bayer, "Optically-active confined acoustic phonons in $CsPbI_3$ nanocrystals explored by resonant Raman scattering", Submitted (2025)

1 Theoretical background

This chapter introduces the theoretical background on spin properties of lead halide perovskites, covering Landé g-factors in bulk and low-dimensional structures, as well as acoustic phonons in perovskite nanocrystals revealed by resonant spin-flip Raman spectroscopy and Raman scattering. Section 1.1 covers the fundamental electronic properties of lead halide perovskites, including excitons and nanostructures. Sections 1.2–1.5 investigate various aspects of spins in semiconductors, focussing on their optical orientation, their interactions with magnetic fields, and interactions with lattice nuclei, respectively. In Section 1.6, inelastic scattering of light is introduced, focussing on the concept of phonons (Section 1.6.1) and resonant Raman scattering (Section 1.6.2). Finally, Section 1.6.3 presents the technique of spin-flip Raman spectroscopy, which is experimentally used in Chapters 3–5 to investigate the spin properties of lead halide perovskites in various dimensions.

1.1 Band structure of lead halide perovskites

The optical properties of semiconductor materials are primarily determined by interband transitions of electrons between the highest occupied band (valence band) and the lowest unoccupied band (conduction band). The valence band (VB) and conduction band (CB) arise from the hybridization of atomic orbitals that occurs when atoms are brought into proximity. This leads to an overlap of valence electronic, resulting in the formation of energy bands separated by an energy gap. Semiconductors typically exhibit a band gap energy E_g in the order of 1 eV with the nearest energy extrema of the VB and CB occurring at a wave vector of $k = 0$ in direct semiconductors. There, the maximum of the VB coincides with the minimum of CB in momentum space, enabling the excitation of an electron from the VB to the CB through the absorption of a photon with energy $E_{\text{photon}} \geq E_g$. This excitation leaves an unoccupied state in the VB, which can be described as a hole, a positively charged quasiparticle. Thus, an interband transition can also be understood as the creation of an electron-hole pair. When the Coulomb interaction is taken into account, this pair forms a neutral bound state known as an exciton (see Section 1.1.2). In contrast, in indirect semiconductors, where the maximum of the VB and the minimum of CB differ in momentum space, a phonon is required to conserve momentum during the electron transition which consequently reduces the probability of optical transitions. Therefore, in direct semiconductors, where the absorption of a photon is sufficient to generate an electron-hole pair, the light-matter interaction is significantly enhanced, making optical investigations particularly interesting. Lead halide perovskites such as $MAPbI_3$, $CsPb(Br, I)_3$ and $(PEA)_2(MA, FA)_{n-1}Pb_n(Br, I)_{3n+1}$ belong to the class of direct semiconductors and will be the focus of investigations in this thesis. Additional properties related to the band structure of these materials are discussed in the following. [76–78]

Perovskites refer to materials with the general composition ABX_3. In lead halide perovskites, presented in this thesis, A represents a cation such as methylammonium (MA: CH_3NH_3), formamidinium (FA: NH_2CH), phenethylammonium (PEA: $(C_6H_5)C_2H_4NH_3$) or caesium (Cs), B is lead (Pb) and X is a halide, such as bromide (Br) or iodine (I). The crystal structure consists of corner-sharing octahedra PbX_6^-, with lead at the center and halogen atoms at the corners, while an additional cation A^+ stabilizes the space between the octahedral structures [2], see Figure 1.1(a). The chemical bonds within the perovskite structure predominantly exhibit ionic character [79], enabling the band gap formation to be considered only based on the atomic orbital structures of lead and halide ions. In particular, the valence band (VB) is formed by hybridized lead 6*s*- and halide *p*-orbitals, while the conduction band (CB) mainly originates from the lead 6*p*-orbitals with an admixture of halide *s*-orbitals [18, 80], see Figure 1.1(b). Since the contributions to the VB maximum from lead and iodine are in a ratio of approximately 3:1 [80], the lead 6*s*-orbitals predominantly determine the top of the VB. Therefore, the holes are characterized by an *s*-type wave function, while the electrons are characterized by a *p*-type wave function. Figure 1.1(c) presents the simplified representation of the band and spin structure near the band gap at the *R*-point in the Brillouin zone.

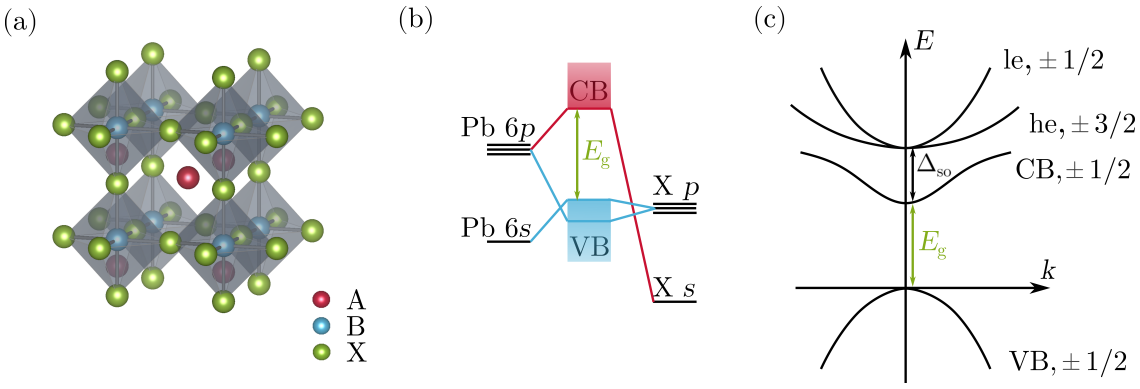

Figure 1.1: (a) Schematic bulk perovskite ABX_3 structure composed of corner-sharing BX_6 octahedra stabilized by central cations A. The visualization is performed with VESTA3 [81] based on structural data from the Crytallographic Open Database [82]. (b) Formation of VB and CB from the antibonding orbitals between lead (Pb, left) and halide (X, right), adapted from [83–85]. (c) Simplified band structure for cubic perovskites, with the bands labeled as VB, CB, heavy electron (he), and light electrons (le). The optical band gap is formed between the VB and CB at the *R*-point, with a band gap energy of E_g, and split-off bands separated by the spin-orbit coupling energy Δ_{so}, adapted from [58].

The conduction bands of cubic lead halide perovskites consist of the lowest energy electron band (CB) and two higher energy electron bands, the heavy-electron (he) and light-electron (le) bands, as shown in Figure 1.1(c). Note that for lead halide perovskites with lower symmetry, the he and le bands are initially non-degenerate [62]. Spin-orbit coupling causes a splitting that separates the he and le bands from the CB band. Coupling of the orbital angular momentum L to the spin S via the spin-orbit interaction results in the total angular momentum $J = L + S$ [86]. For the VB with an *s*-type wave function (corresponding to an angular momentum of $L = 0$), no spin-orbit coupling occurs, resulting in a total angular momentum $J = 1/2$. This configuration features doubly degenerate states ($j = 1/2, j_Z = \pm 1/2$), where j_Z denotes the *z*-component of J [87]. For the conduction bands, characterized by a *p*-type wave function ($L = 1$), the higher $J_1 = 3/2$ bands, with states $(3/2, \pm 3/2)$ (he) and $(3/2, \pm 1/2)$ (le), are energetically separated by the spin-orbit coupling energy Δ_{so} from the CB $J_2 = 1/2$ with $(1/2, \pm 1/2)$ [88]. Since the spin-orbit coupling energy is comparable to the band gap energy itself ($\Delta_{so} \sim 1 - 1.5$ eV [62, 80,

88]), the higher-energy electron bands (he, le) can be neglected. Thus, for the optical properties near the band gap, the lowest energy transitions occur between the VB and lowest CB, where both electron and hole have $j = 1/2$.

The band gap energy of lead halide perovskites can be tuned from the infrared to the ultraviolet spectral range by changing the halide composition. For instance, the difference in band gap energy can exceed 1 eV when comparing materials based on iodine to those containing chlorine. [11] Fine tuning of the band gap energy can be achieved by employing halide mixtures with varying ratios [89]. The energy of the CB minimum is primarily governed by the position of the lead *p*-level, while the energy of the VB maximum is influenced by three competing effects: electronegativity, confinement, and the hybridization strength between lead *s*- and halide *p*-orbitals, as described in Reference [90]. First, the VB maximum experiences a downward shift, going from iodine to chlorine, reflecting the increasing electronegativity of the halides [91]. Although electronegativity lowers the VB maximum, this effect is countered by two other factors: the decreasing lead-halide distance from iodine to chlorine, which confines an electron in the lead atom more strongly and raises its energy, and the enhanced hybridization strength. Nevertheless, the dominant factor remains the downward shift of the VB maximum and the upward shift of the CB minimum due to electronegativity, leading to a progressive increase of the band gap energy as the halide is tuned from iodine to chlorine. Note that changing the cation A does not directly affect the electronic states [2], as it does not participate in the bonding interactions. However, it can indirectly influence the electronic structure by modifying the lattice volume or introducing lattice distortions in the perovskite structure. [90]

1.1.1 Structural phase transitions in lead halide perovskites

In general, the perovskite structure is flexible concerning component substitution as long as the ionic radii are compatible with the lattice and charge neutrality is preserved. If the ionic radii do not fit perfectly, deviations from the cubic perovskite structure ($a = b = c$) can occur, leading to the formation of tetragonal ($a = b \neq c$) or orthorhombic ($a \neq b \neq c$) phases, where a, b, and c represent the crystallographic axes. Despite these variations, the characteristic perovskite structure of corner-sharing BX_6 octahedra is preserved. [2] Phase transitions can occur due to temperature changes, leading to the formation of new structural phases through octahedral tilting, distortion, or cation displacement [92–94]. For the widely used organic-inorganic lead halide perovskites $MAPbI_3$ and $FAPbI_3$, the ideal cubic α-phase remains thermodynamically stable at temperatures above room temperature, as structures with higher symmetry are favored at elevated temperatures [95]. Structural stability in perovskites is indicated by the Goldschmidt tolerance factor t, which is calculated based on the ionic radii, r_i, of the ions (A, B, X) in the compound [63]:

$$t = \frac{r_A + r_X}{\sqrt{2}(r_B + r_X)}. \tag{1.1}$$

Typically, a tolerance factor in the range of $0.8 \leq t \leq 1$ indicates stable perovskite structures, where $t = 0.9$–1 corresponds to an ideal cubic structure [96]. Values in the range of $0.8 \leq t \leq 0.9$ tend to favor lower-symmetry structures, while values outside this range cause the perovskite structure to become increasingly unstable [2]. For the lead halide perovskites studied in this thesis, the tolerance factors are: $MAPbI_3$ ($t = 0.912$), $CsPbI_3$ ($t = 0.851$), and $CsPbBr_3$ ($t = 0.862$) [97].

1.1.2 Excitons in bulk perovskites

Optical excitation of semiconductor materials results in the formation of excitons, which dominate the optical properties near the band gap. These excitons are formed through the attractive Coulomb interaction between negatively charged electrons and positively charged holes, which can be treated analogously to hydrogen atoms. As a result, the excitation energy required for the optical transition is reduced by the Coulomb interaction. [76]

The excitonic levels form a multiplet of states with distinct spin configurations of the carriers [98]. The exchange interaction, which couples the electron and hole spins, leads to the formation of a singlet-triplet structure of the exciton [48]. In the absence of a magnetic field, the singlet-triplet splitting is primarily determined by the exchange energy [98]. In cubic lead halide perovskite structures, the exchange interaction separates the excitonic states into a spin-forbidden dark singlet ($J = 0$) and spin-allowed bright triplet ($J = 1$), where the two of the three triplet levels ($J_z = \pm 1$) can be selectively addressed with circularly polarized light [99]. For lower-symmetry crystal structures, such as tetragonal or orthorhombic phases, an anisotropic exchange interaction lifts the degeneracy of the triplet states [100]. This results in a bright exciton fine structure consisting of three orthogonal spatial states, $|x\rangle$, $|y\rangle$, and $|z\rangle$, which couple to linearly polarized light with an exciton dipole moment oscillating along the x-, y-, or z- axis, respectively [101]. Further fine structure splitting can be induced by external or internal magnetic fields through the Zeeman interaction between the electron and hole spins and the magnetic field [98]. In strong magnetic fields, where the Zeeman splitting exceeds the exchange interaction, the $J_z = \pm 1$ states experience a Zeeman splitting proportional to the sum of the electron and hole g-factors, while the $J_z = 0$ states (which include the singlet and one of the triplet states) split proportionally to their difference.

1.1.3 Excitons in low dimensions

In systems with reduced dimensionality, excitons are spatially confined when the size of the system is comparable to or smaller than the exciton Bohr radius. In such systems, the energy levels are quantized along the direction of the confinement. Based on the number of free dimensions, these systems are classified as quantum wells (2D), quantum wires (1D), and quantum dots (0D). [76] This section explores the properties of two-dimensional and zero-dimensional lead halide perovskites.

In 2D lead halide perovskites, the spatial confinement is achieved in one direction by periodically interrupting the structure of the three-dimensional perovskite $APbX_3$ with layers of organic molecules. As shown in Figure 1.2(a) the planes of lead halide octahedra are surrounded by barriers of organic spacers. [2] Perovskites in the Ruddlesdon-Popper (RP) phase that incorporate monovalent cations such as the organic molecule phenylethylammonium (PEA), which has a large ionic radius, preferentially form layered 2D structures rather than 3D perovskites [102]. This 2D structure requires a bilayer arrangement of organic spacer cations. Due to the molecular structure of PEA, the organic molecules cannot interlink with each other, typically resulting in larger interlayer distances, often exceeding twice the length of the cation. As a result, the layers, defined as lead halide octahedra separated by van der Waals-bonded pairs of PEA, remain well-separated. This separation suppresses tunneling and limits interactions of electrons, holes, and excitons between individual layers. [103] Therefore, the structure shown in Figure 1.2(a) effectively behaves as a quantum well as schematically depicted in Figure 1.2(b). Within this thesis, the focus is set on lead halide 2D perovskites in the RP phase with the composition $A'_2 A_{n-1} Pb_n X_{3n+1}$ [104], where A' is PEA, A is a monovalent cation (MA, FA), X is a halide (Br or I), and

n is the number of inorganic layers. The case of $n = 1$ corresponds to a purely two-dimensional system. As the number of layers increases ($n \to \infty$), the system tends towards a three-dimensional system.

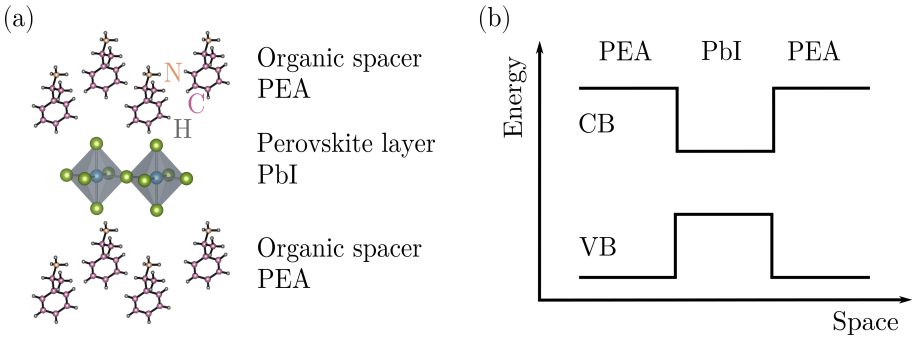

Figure 1.2: 2D layered perovskite $(PEA)_2PbI_4$ for $n = 1$: (a) Arrangement of the lead iodine octahedra separated by organic spacers PEA, (b) forming a quantum well for electrons and holes along the stacking direction. Adapted from [105, 106].

As the number n of inorganic layers (lead halide octahedra) increases, the optical absorption edge of 2D perovskites shifts to lower energies with an increasing number of PbI_6 octahedra [103]. This energy shift can be explained by the analogy between 2D perovskites and QWs, where the width of the QW (d) determines the strength of confinement experienced by the carriers: a narrower QW induces stronger confinement, leading to a larger confinement energy. Consequently, the effective band gap energy increases due to quantum confinement relative to the unconfined bulk band gap following the relation $E_g \propto E_g^0 + 1/(d)^2$, where E_g^0 is the bulk band gap energy. [107]

2D perovskites exhibit an enhanced exciton binding energy due to the spatial confinement of electrons and holes, resulting in an increased overlap of their wave functions. Additionally, selecting a barrier material with a smaller dielectric constant ϵ_b compared to the well's dielectric constant ϵ_w can further enhance the exciton binding energy, referred to as dielectric confinement [108]. For the material $(PEA)_2PbI_4$, the dielectric constants are $\epsilon_w = 6.1$ for PbI_4 [108] and $\epsilon_b = 3.3$ for PEA [109]. This results in a significantly increased exciton binding energy, reaching approximately 260 meV for $(PEA)_2PbI_4$ with $n = 1$, in contrast to only 16 meV observed in bulk $MAPbI_3$ [110]. Consequently, excitons govern the optical properties of 2D perovskites even at room temperature [106]. However, as the thickness of the quantum well (QW) increases, the exciton binding energy decreases due to the expansion of the exciton radius.

In lead halide perovskite nanocrystal (NC) with typical sizes of only several nanometers, the spatial confinement in all three directions strongly affects their electronic and optical properties. The strength of the confinement depends on the size of the NC relative to the exciton Bohr radius. As the NC diameter decreases and approaches the exciton Bohr radius of the specific material, quantum confinement becomes stronger, leading to an increase in band gap energy [111].

While the fine structure splitting in bulk semiconductor materials is relatively small (< 0.1 meV), it is significantly enhanced in confined systems where the exciton is tightly bound [112]. In the 2D perovskite $(PEA)_2PbI_4$ a bright-dark splitting of several tens of meV has been reported [113]. In NCs, the bright-exciton fine structure arises from the interplay between the shape anisotropy and crystalline phase anisotropy [66, 114]. In Chapter 5, the focus is set on all-inorganic $CsPbBr_3$ and $CsPbI_3$ NCs. In these materials, splitting of the bright exciton levels has been reported to

be on the order of 1 meV for $CsPbBr_3$ NCs and several hundreds of μeV for $CsPbI_3$ NCs, with a mean size of approximately 10 nm [17].

1.2 Optical spin orientation and recombination of excitons

The absorption of circularly polarized light can generate spin-oriented excitons and charge carriers, referred to as optical orientation. Optical orientation is based on the transfer of angular momentum from circularly polarized light to the carriers due to angular momentum conservation, with the light's angular momentum projections of $J_{z,\sigma^\pm} = \pm 1$ (in units of $\hbar$). [76] In an optical experiment, excitation with circularly polarized light ($\sigma^\pm$) induces optical transitions that generate $|\pm 1\rangle$ excitons, corresponding to the spin configurations ($|\uparrow\Uparrow\rangle$, $|\downarrow\Downarrow\rangle$) in lead halide perovskites. Here, $\uparrow, \downarrow$ represent the electron spins, while $\Uparrow, \Downarrow$ denote the hole spins. Recombination of photoexcited electrons and holes can only occur if the optical selection rules are fulfilled. The circular polarization of the luminescence is then analyzed, providing a direct indication of the carrier spin polarization [87].

In the specific case of lead halide perovskites, where both the electron and hole have a spin of 1/2, the selection rules enable a maximum spin polarization of 100 % immediately after photogeneration and during polarized luminescence [73, 115]. In contrast, conventional III-V and II-VI bulk semiconductors are limited to a maximum spin polarization of 50 % in absorption and only 25 % in emission [115]. Between the creation of spin-polarized carriers and their recombination, the spin orientation of the carriers decreases to its equilibrium state due to various relaxation processes [116]. In direct-band semiconductors like gallium arsenide, these timescales are typically in the order of nanoseconds [87]. The complete dissipation of the initial non-equilibrium spin polarization, referred to as spin lifetime T_s, is governed by both the exciton recombination time τ and the spin relaxation time τ_s, as expressed by [116]

$$\frac{1}{T_s} = \frac{1}{\tau} + \frac{1}{\tau_s}. \tag{1.2}$$

Here, τ_s is determined by the spin relaxation mechanisms.

In general, carriers lose their spin orientation primarily through their transfer to the crystalline lattice, mediated by spin-orbit and hyperfine interactions [117]. Several mechanisms can lead to spin relaxation, including the Dyakonov-Perel, Elliott-Yafet, and Bir-Aronov-Pikus mechanisms, as well as the hyperfine interactions with randomly oriented nuclei [73, 87]. However, as the Dyakonov-Perel, Elliott-Yafet, and Bir-Aronov-Pikus mechanisms are based on the free motion of carriers within the crystal, their contribution is suppressed for localized carriers in lead halide perovskites at low temperatures. Consequently, spin depolarization in these materials is predominantly caused by the hyperfine interaction with randomly oriented nuclei [18].

In addition, when a weak magnetic field is applied perpendicular to the light's wave vector, the carrier spins start to precess around the magnetic field, leading to a spin depolarization known as the Hanle effect [117]. Conversely, applying a longitudinal external magnetic field can counteract spin depolarization by aligning the carrier spins along the magnetic field orientation, a process referred to as polarization recovery effect [73].

1.3 Spin in magnetic field

As discussed in Section 1.1, the lowest energy transition in lead halide perovskites occurs between VB and CB resulting in both electron and hole spins of 1/2. The spin eigenstates are commonly referred to as spin-up ↑ ($s_z = +1/2$), aligned with the quantization-axis (z), and spin-down ↓ ($s_z = -1/2$), aligned antiparallel to the z-axis. In a zero magnetic field, the spin levels degenerate. If an external magnetic field is applied, the degeneracy is lifted, and the energy levels split due to the Zeeman effect, see Figure 1.3(a).

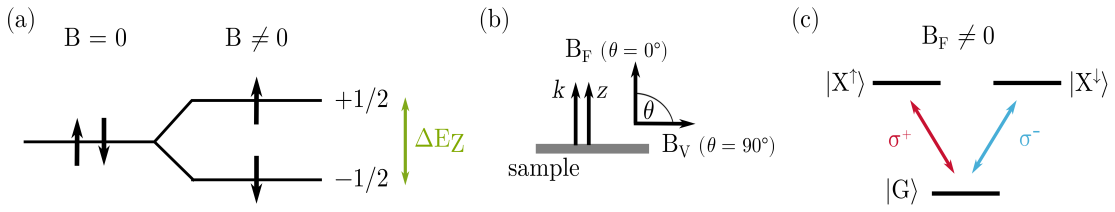

Figure 1.3: (a) Schematic of the Zeeman splitting with two initially degenerate spin levels separated by the Zeeman energy ΔE_Z for $g > 0$. (b) Magnetic field orientations for the pure geometries: Faraday geometry, with the magnetic field B_F aligned longitudinally to the direction of light propagation $\mathbf{k}$, and Voigt geometry, with the magnetic field B_V, oriented transversely. The angle θ denotes the tilt of the magnetic field relative to the direction of light propagation. (c) Optical selection rules for the generation of bright exciton states $|X^{\uparrow\downarrow}\rangle$ from the crystal's ground state $|G\rangle$ with circularly polarized light $\sigma^{\pm}$, adapted from [78].

The Zeeman effect for a spin-1/2 particle is described by the Hamiltonian [61]

$$\hat{H}_Z = \frac{1}{2}\mu_B \sum_{\alpha,\beta} g_{\alpha,\beta}\sigma_\alpha B_\beta \tag{1.3}$$

with the Bohr magneton μ_B, the tensor of g-factors $g_{\alpha,\beta}$, Pauli matrices σ_α, and magnetic field components B_β for the Cartesian coordinates $\alpha, \beta = x, y, z$. The number of independent components of $g_{\alpha,\beta}$ is determined by the symmetry of the crystal. For cubic symmetry, isotropic in all three spatial directions, the tensor simplifies to $g_{\alpha,\beta} = g\delta_{\alpha,\beta}$, where $\delta_{\alpha,\beta}$ is the Kronecker delta, thereby reducing to a scalar g [117]. For reduced symmetry, a g-factor anisotropy can be expected. For example, lead halide perovskites are known to undergo a phase transition from cubic to tetragonal or orthorhombic structures at low temperatures [118]. In the case of symmetry breaking, such as in 2D materials, the g-factor along the sample growth direction, $g_\parallel = g_{zz}$, can differ from the g-factor perpendicular to it, $g_\perp = g_{xx} = g_{yy}$. Thus, observing a g-factor anisotropy can provide insights into the crystal symmetry, while the magnitude of the g-factor is connected to key band structure parameters such as the band gap E_g [62] and the momentum interband matrix element p [119]. In vacuum, the free electron g-factor is $g_{e,0} = 2.0023$ [120]. Spin-orbit coupling modifies the g-factor, leading to significant differences between the electron g-factor in vacuum and semiconductors [121]. For instance, the g-factor for CB electrons is approximately −50 in InSb [121] and −0.44 in GaAs [119]. Consequently, the Zeeman splitting can be significantly reduced or enhanced due to the influence of the spin-orbit coupling [86] as well as the energetic arrangement of the Zeeman energy levels. The band gap energy-dependent variations of the g-factor for lead halide bulk perovskites and perovskite NCs will be discussed in Section 1.4.

In Equation (1.3), the Hamiltonian of the Zeeman effect for one spin-1/2 particle is presented. When an electron and a hole form an exciton, Equation (1.3) extends to describe the exciton Hamiltonian in the presence of an external magnetic field to [122]

$$\hat{H}_{\mathrm{Z,X}} = \underbrace{\frac{1}{2}\mu_{\mathrm{B}} \sum_{\alpha,\beta} (g_{e,\alpha,\beta} + g_{h,\alpha,\beta})\sigma_{\alpha} B_{\beta}}_{H_{\mathrm{Z,e}}+H_{\mathrm{Z,h}}} + \underbrace{\frac{1}{4} J_{e-h} \sum_{\alpha} \sigma_{e,\alpha}\sigma_{h,\alpha}}_{H_{\mathrm{exch}}}, \tag{1.4}$$

where H_{exch} denotes the Hamiltonian for the exchange interaction. The exchange interaction J_{e-h} couples the electron and hole spins, accounting for the electron-hole interaction. As the Zeeman splitting is defined by the scalar product of the magnetic field and the spin, the relative orientation of the spin with respect to the magnetic field must be considered. The direction of light propagation $\mathbf{k}$ is assumed to be parallel to the sample's quantization z-axis ($\mathbf{k} \parallel z$). We distinguish between the pure magnetic field geometries, Faraday ($\theta = 0^{\circ}$) and Voigt geometry ($\theta = 90^{\circ}$), and tilted geometries denoted by the angle θ, as illustrated in Figure 1.3(b). In Faraday geometry, where the magnetic field is aligned with the direction of light propagation (longitudinal magnetic field), circularly polarized light can excite the optically active exciton states $|X^{\uparrow}\rangle$ and $|X^{\downarrow}\rangle$, which are formed by parallel electron and hole spins in lead halide perovskites, as shown in Figure 1.3(c). A magnetic field applied in Voigt geometry induces a mixing of the exciton states $|X^{\uparrow}\rangle$ and $|X^{\downarrow}\rangle$. The system is diagonal in the base defined by the states

$$|X^{\pm}\rangle = \frac{1}{\sqrt{2}} \left(|X^{\uparrow}\rangle \pm |X^{\downarrow}\rangle \right), \tag{1.5}$$

which can be individually addressed by horizontal and vertical linear polarizations. As a result, when analyzing the polarization dependence in a magnetic field, such as with the technique of spin-flip Raman scattering (see Section 2.1.3), circularly polarized light is selected for measurements in Faraday geometry, while linearly polarized light is used in Voigt geometry [123].

1.4 Landé g-factors of carriers

In Section 1.3, the Landé g-factor, a fundamental parameter of the band structure that defines the coupling between spins and external magnetic fields is introduced. This section focuses on the influence of various band structure parameters on the electron and hole g-factors, highlighting a band gap energy dependence of the g-factors observed in semiconductors, bulk lead halide perovskites, and perovskite NCs, based on References [58, 62, 121].

In conventional III-V and II-VI semiconductors with a zinc-blende crystal structure, the dependence of the electron g-factor on the band gap energy E_{g} is described by the Roth-Lax-Zwerdling equation [121, 124]

$$g_{\mathrm{e}} = g_0 \left[1 - \frac{2p^2}{m_0} \frac{\Delta_{\mathrm{so}}}{E_{\mathrm{g}}(E_{\mathrm{g}} + \Delta_{\mathrm{so}})} \right], \tag{1.6}$$

where p denotes the interband momentum matrix element, which indicates the interaction strength between the VB and the CB. Δ_{so} denotes the spin-orbit splitting of the VB. As the band gap energy increases, the electron g-factor also increases, approaching the value of the free electron g-factor g_0. In contrast to lead halide perovskites, conventional semiconductors with a zinc-blende structure contain holes in the VB that exhibit a p-type wave function and a degenerate

VB at $k = 0$. As a result, holes in these semiconductors experience fast spin relaxation [116], and their g-factor dependence is typically not considered. This situation changes in lead halide perovskites.

In lead halide perovskites, both photogenerated resident electrons and holes are present. Therefore, in Reference [62], the g-factors of electrons and holes in various bulk lead halide perovskites are investigated. This study reveals that the g-factors of both electrons and holes depend on the band gap energy, which can be tuned through compositional changes (see Figure 1.4(a)). As the band gap energy increases, the electron g-factor decreases, while the hole g-factor increases, transitioning from negative to positive values and crossing zero at approximately 1.8 eV. The dependence of the electron g-factor on the band gap energy in lead halide perovskites is reversed compared to conventional semiconductors. Density functional theory (DFT) calculations combined with tight-binding and $\mathbf{k} \cdot \mathbf{p}$ approaches are used to microscopically calculate the g-factors, providing a theoretically description of the experimental dependence (see solid lines in Figure 1.4(a)).

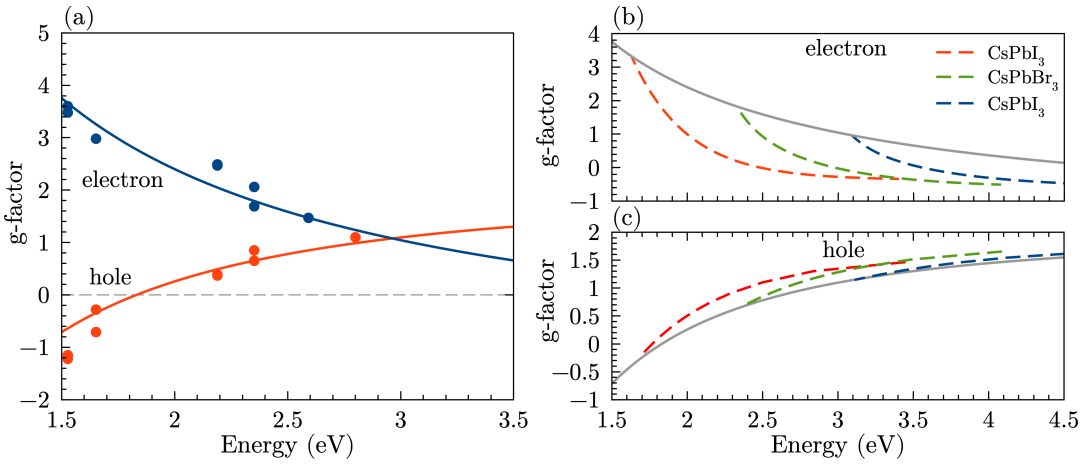

Figure 1.4: (a) Dependence of the electron (blue) and hole (red) g-factors on the band gap energy (dots) along with the theoretical curves for bulk lead halide perovskites (solid lines), adapted from Reference [62]. (b) and (c) g-factor dependence of $CsPb(I, Br, Cl)_3$ perovskite NCs (dashed lines), adapted from Reference [58], with (b) for electrons and (c) for holes. Bulk dependences from (a) are indicated by gray lines.

For bulk lead halide perovskites with cubic symmetry, the dependence of the hole and electron on the band gap energy is defined by

$$g_\mathrm{h} = 2 - \frac{4p^2}{3m_0}\left(\frac{1}{E_\mathrm{g}} - \frac{1}{E_\mathrm{g} + \Delta_\mathrm{so}}\right), \tag{1.7}$$

$$g_\mathrm{e} = -\frac{2}{3} + \frac{4p^2}{3m_0}\frac{1}{E_\mathrm{g}} + \Delta g_\mathrm{rem}, \tag{1.8}$$

where m_0 is the free electron mass, Δ_so represents the spin-orbit splitting of the CB, and Δg_rem accounts for the contributions from higher energy bands (remote bands). Based on the analysis of the influence of the different bands, the main contributions to the g-factor can be identified. For both electrons and holes, the mixing between the CB and VB decreases with increasing band gap energy. While the mixing with the CB is the main contribution for the holes in the VB,

for the electrons, contributions from remote bands need to be considered. In contrast, these remote band effects for holes are rather small. For the holes in the VB, the third term arises from the interaction with the higher-energy, four-fold degenerate le and he conduction bands at the R-point. However, as Δ_{so} is in the range of 1.5 eV, the separation of the CB and the split-off he and le bands is relatively large. To achieve a good alignment of the experimental data with theoretical predictions, as shown in Figure 1.4(a), Δ_{so} is set to 1.5 eV, and the other parameters are set to $\hbar p/m_0 = 6.8\,\text{eV·Å}$ and $\Delta g_{\text{rem}} = -1$. The g-factor of the bright exciton, defined as the sum of the electron and hole g-factor, remains nearly constant and independent of the band gap energy because the individual contributions of the electron and hole, which are both proportional to $1/E_g$, approximately compensate each other [125].

In Reference [58], the electron and hole g-factors of all-inorganic lead halide $CsPbX_3$ (X = I, Br, Cl) perovskites NCs are investigated, and their dependence on the band gap energy is modeled. The effective band gap energy is varied not only through halide exchange but also by altering the NC size, as discussed in Section 1.1.3. The electron g-factor exhibits a strong effect on the quantum confinement, significantly decreasing with increasing effective band gap energy (decrease of the NC size) (see Figure 1.4(b)). In contrast, the hole g-factor shows only minor deviations from the bulk values (see Figure 1.4(c)). Due to the pronounced renormalization of the electron g-factor caused by quantum confinement, the theoretical model for bulk lead halide perovskites needs to be extended to include size quantization effects in spherical perovskite NCs, resulting in the following expressions for the electron and hole g-factors:

$$g_h(E_h) = 2 - \frac{4p^2}{3m_0} w_h \left(\underbrace{\frac{1}{E_g + E_h}}_{\text{VB-CB}} - \underbrace{\frac{1}{E_g + E_h + \Delta_{so}}}_{\text{VB-(he/le)}} \right) \tag{1.9}$$

$$g_e(E_e) = -\frac{2}{3} + \frac{4p^2}{3m_0} \underbrace{\frac{w_e}{E_g + E_e}}_{\text{CB-VB}} + \Delta g_{\text{rem}} + \delta g_e^{so}. \tag{1.10}$$

However, the effect of the NC shape on the g-factor is expected to be relatively weak. The quantization energies of hole and electron are denoted as $E_{h,e}$, respectively, while the confinement-induced band mixing is represented by $w_{h,e}$. In NCs, the degeneracy between the heavy and light electrons is lifted, enabling mixing with the CB in the presence of a magnetic field. This leads to an additional contribution to the electron g-factor from the mixing with the split-off electron bands, denoted as δg_e^{so}. As a result, quantum confinement strongly renormalizes the electron g-factor, resulting in a significant decrease of g_e as the electron size-quantization energy increases.

This section quantifies the influences on the g-factor of both electrons and holes in bulk lead halide perovskites, as well as in perovskite NCs, considering the effects of band gap energy, the mixing of CB and VB and confinement-induced mixing with the split-off band. Chapter 4 investigates the dependence of the electron and hole g-factors in 2D RP type lead halide perovskites, while Chapter 5.1 focuses on $CsPbBr_3$ NCs. For both material systems, the calculated dependences shown in Figure 1.4 are used for comparison.

1.5 Carrier-nuclei spin interaction in perovskites

While the hyperfine interaction is introduced in Section 1.2 as the primary spin relaxation mechanism for localized carriers, it also gives rise to an effective nuclear field in the presence of optically oriented carriers [116]. This section explores the hyperfine interaction between carrier and nuclear spin systems, focusing on dynamic nuclear polarization (DNP), based on References [15, 116]. Due to the low energy of nuclear spin resonances at photon energies corresponding to the optical band gap in semiconductors, nuclear spins cannot directly interact with photons. Instead, their resonance occurs in the radio frequency range, requiring indirect methods such as DNP to optically achieve an effective nuclear polarization, as further explained in this section. [117]

Spin transfer from the carrier to the nuclei system is mediated by the hyperfine interaction [117]. Essentially, hyperfine interaction involves the transfer of angular momentum from carriers to nuclei while conserving the total spin of the interacting particles [87]. The strength of the hyperfine interaction is characterized by the hyperfine coupling constant, which is proportional to the square of the carrier wave function at the location of the nucleus [87], and therefore it depends on the specific type of the carrier wave function. In general, the hyperfine interaction between the carrier and nuclear spin is given by the Hamiltonian [117, 126]

$$\hat{H}_{\mathrm{hf}} = \frac{2\mu_{\mathrm{B}}\mu_{\mathrm{I}}}{I}\hat{\mathbf{I}}\Bigg(\underbrace{\frac{\hat{\mathbf{L}}}{r^3} - \frac{\hat{\mathbf{s}}}{r^3} + 3\frac{\mathbf{r}(\mathbf{r}\cdot\hat{\mathbf{s}})}{r^5}}_{\text{dipole-dipole}} + \underbrace{\frac{8\pi}{3}\hat{\mathbf{s}}\delta(\mathbf{r})}_{\text{Fermi contact}}\Bigg), \tag{1.11}$$

with the magnetic moment μ_{I} of the nucleus, nuclear spin operator $\hat{\mathbf{I}}$, angular momentum operator $\hat{\mathbf{L}}$, carrier spin operator $\hat{\mathbf{s}}$, the vector between the carrier and nucleus $\mathbf{r}$, and the Dirac δ-function $\delta(\mathbf{r})$. The Hamiltonian consists of two parts: the dipole-dipole and Fermi contact interaction, as highlighted in Equation (1.11). First, the dipole-dipole interaction depends on the distance $\mathbf{r}$ between the carrier and nucleus. As the distance increases, the contribution of the dipole-dipole interaction rapidly decreases [127]. Second, the Fermi contact interaction provides the main contribution to the hyperfine interaction. It is proportional to the carrier density at the nucleus $\propto (\hat{\mathbf{I}}\cdot\hat{\mathbf{s}})\delta(\mathbf{r})$ and contributes when $\delta(\mathbf{r}) \neq 0$ at $\mathbf{r} = 0$, which requires a spherically symmetric carrier wave function [126]. As discussed in Section 1.1, the hole wave function in lead halide perovskites has an *s*-orbital character, resulting in a significant overlap between the wave function of the hole and the nucleus. Consequently, the hyperfine interaction between the holes and nuclei is expected to be stronger. In contrast, the Fermi contact interaction is negligible in the coupling of electrons with *p*-orbital character to nuclear spins, which interact instead via the weak dipole-dipole interaction [87]. Note that in bulk lead halide perovskites, both electrons and holes have been observed to interact with the nuclei [18, 73]. Therefore, the equations presented in this section, which are formulated for the typically stronger interaction between the nuclei and the holes, are equally valid for electrons.

Continuous optical pumping of the hole spin polarization in the presence of an external longitudinal magnetic field in Faraday geometry can lead to a nuclear spin polarization, as described by Equation 1.12, and simultaneously suppresses hole spin relaxation within the effective nuclear fluctuation field [116, 117]. Circularly polarized is used to spin-polarize the holes and induce a nuclear spin polarization. The resulting spin-polarized holes $\langle \mathbf{S}_{\mathrm{h}} \rangle$ generate a Knight field $\mathbf{B}_{\mathrm{K}}$, which acts as an effective magnetic field on the nuclei, transferring the spin orientation to the nuclei and aligning them in the same direction as the holes (see Figure 1.5).

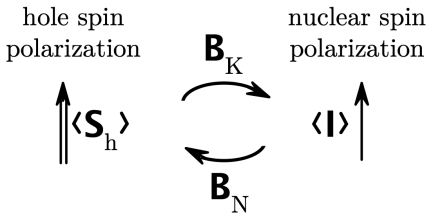

Figure 1.5: Schematic illustration of the hyperfine interaction between holes and nuclei via DNP. The holes are spin-polarized by circularly polarized light $\langle \mathbf{S}_\mathrm{h} \rangle$. The effective Knight field $\mathbf{B}_\mathrm{K}$ transfers the spin-polarization of the hole to the nuclei, thereby the nuclei become polarized leading to an average nuclear polarization $\langle \mathbf{I} \rangle$. This nuclear polarization induces an Overhauser field $\mathbf{B}_\mathrm{N}$ that acts on the hole spin, either reducing or increasing the Zeeman splitting depending on the sign of the g-factor. The scheme is adapted from [15].

The average nuclear spin polarization transferred from the hole to the nuclei is given by [116]

$$\langle \mathbf{I} \rangle = l \frac{4I(I+1)}{3} \frac{\mathbf{B}(\mathbf{B} \cdot \langle \mathbf{S}_\mathrm{h} \rangle)}{B^2}, \tag{1.12}$$

where the leakage factor l, which ranges from $0 < l < 1$, accounts for the DNP losses due to other relaxation processes. The limiting case $\langle \mathbf{I} \rangle = 0$ for $\mathbf{B} \perp \langle \mathbf{S}_\mathrm{h} \rangle$ occurs in Voigt geometry. In contrast, in Faraday geometry, the strength of DNP is maximized. The exchange interaction among the lattice nuclei, which arises from their dipole-dipole coupling of the localized magnetic moments, is generally negligible due to the minimal overlap of nuclear wave functions [117]. Consequently, the focus is set on the influence of the nuclear spin system on the carrier spin system, while internal effects within the nuclear spin system are neglected. A single carrier typically interacts with a large ensemble of nuclei simultaneously, on the order of 10^4 to 10^6 nuclei [117], which collectively act as an effective magnetic field known as the Overhauser field $\mathbf{B}_\mathrm{N,h}$. The Overhauser field is expressed by

$$\mathbf{B}_\mathrm{N,h} = \frac{\alpha A_\mathrm{h} \langle \mathbf{I} \rangle}{g_\mathrm{h} \mu_\mathrm{B}}, \tag{1.13}$$

which acts back on the hole spin, as illustrated in Figure 1.5. Here, we introduced the abundance of nuclear isotopes with non-zero spin α and the hyperfine coupling constant A_h. In lead halide perovskites, it has been found in Reference [18] that the hyperfine coupling is predominantly influenced by ^{207}Pb isotopes, which have an abundance of $\alpha = 22.1\,\%$. As a consequence of $A_\mathrm{h} > 0$ [18], the sign of $\mathbf{B}_\mathrm{N,h}$ is only determined by the sign of the carrier g-factor. This provides an experimental method to determine the g-factor sign by identifying the sign of the Overhauser field through the Zeeman splitting. Thus, we define the effect of the hyperfine interaction on the Zeeman splitting as

$$\Delta E_\mathrm{Z} = g \mu_B (B_\mathrm{ext} \pm B_\mathrm{N,h}), \tag{1.14}$$

where the effective Overhauser field $B_\mathrm{N,h}$ can either increase or decrease the Zeeman splitting, thereby influencing the Raman shift induced by an external magnetic field B_ext. In Section 4.1.3, the experimental procedure for measuring the effect of DNP on the Zeeman splitting with the technique of spin-flip Raman spectroscopy is outlined.

1.6 Inelastic scattering of light

This thesis focuses on spin-flip Raman scattering (SFRS), where the spin orientation of a carrier of the photo-excited material is reversed, leading to an energy shift of the scattered light. A general introduction to resonant Raman spectroscopy is provided in Section 1.6, followed by an overview of spin-flip Raman spectroscopy in Section 1.6.3. In addition to spin-flips, inelastic scattering processes in solids typically involve optical or acoustic phonons. As such scattering processes are observed for $CsPbBr_3$ and $CsPbI_3$ NCs in Section 5.2, a brief introduction to phonons is presented in the following.

1.6.1 Phonons

In general, phonons can be present in any solid with a periodic lattice structure. Phonons represent vibrational modes in which atoms are displaced from their equilibrium positions, experiencing a restoring force that causes the lattice to vibrate at characteristic frequencies. These phonon modes are typically in the infrared spectral range. [76]

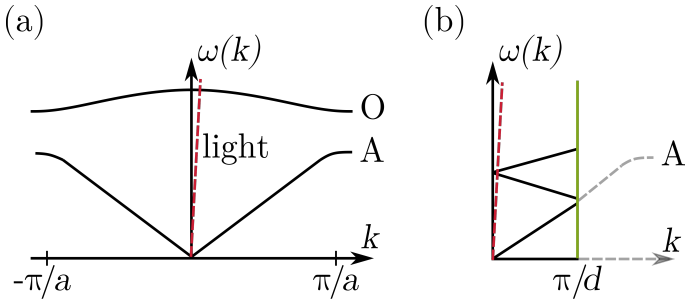

Figure 1.6: (a) Dispersion of the acoustic (A) and optical (O) phonon modes in the first Brillouin zone ($\pm\pi/a$). The red dashed line represents the dispersion of light. Note that the refractive index of light is chosen to be very high to show the dispersion of photons and phonons in the same plot. (b) Folding of the acoustic modes due to confinement within the NC with diameter d. Adapted from [76] (a) and [128] (b).

Phonon modes in a crystal can be classified as either optical or acoustic and further distinguished as transverse or longitudinal. The latter distinction indicates whether the atomic displacements are perpendicular or parallel to the direction of the wave vector, while the former determines whether a phonon can absorb light at its resonance frequency. Optical phonons, in which the atoms are displaced in anti-phase, are associated with an oscillating electric dipole. This dipole can couple to electromagnetic waves (at least for transverse eigenmodes) [77], provided that the phonon and photon share the same frequency and wave vector (momentum selection rule). This requirement is fulfilled at the crossing points of the dispersion relations for optical phonons with photons, as schematically shown in Figure 1.6(a). Note that the dispersion of light $\omega = c/n \cdot k$ is depicted with a very high refractive index n to display the photon and phonon dispersions on the same scale. For acoustic phonon modes, the atomic displacement occurs in-phase. In contrast to optical modes, which are nearly dispersionless for small wave vectors k, acoustic modes have zero frequency at the center of the Brillouin zone and exhibit a linear dispersion relation proportional to the speed of sound in the medium v_s for small k. As $c \gg v_s$, the only crossing point for acoustic modes is at the origin. Therefore, acoustic modes cannot directly couple with light. [76]

The number of acoustic phonon branches is determined by the number of atoms N in the unit cell. In a three-dimensional crystal, the acoustic phonon dispersion consists of three branches, while the optical phonon dispersion consists of $3N - 3$ branches. In the low-temperature orthorhombic phase of lead halide perovskites, the unequal lengths of the crystallographic axes a, b, c result in distinct sound velocities along each axis. In NCs, the dispersion of acoustic phonons is modified due to folding into a mini-Brillouin zone [129], as illustrated in Figure 1.6(b). This folding depends

on the NC size, with the energy of the confined acoustic phonon being inversely proportional to the NC diameter d [71]. Conceptually, the folding is similar to the effect of superlattices on phonons [61]. However, the confinement in NCs extends in all three dimensions. As a result, additional crossing points emerge between the folded phonon dispersion and the light dispersion. Moreover, the increased number of atoms in the primitive unit cell leads to slight differences in the dispersion of all acoustic phonon branches. This combination of effects gives rise to multiple crossing points, resulting in a complex phonon spectrum. Phenomenologically, the low-frequency Raman scattering observed in NCs can be attributed to the breathing modes of the whole NC [130].

In lead halide perovskites with reduced dimensionality, there is not only a significant increase in the exciton binding energy, but also an enhancement of other effects, such as the carrier-phonon interaction. Different vibrational modes have been observed, which are associated with the motion of the inorganic lead halide cage as well as the rotations and bending of the organic cations [131]. Excitons can strongly couple with longitudinal-optical phonons through the Fröhlich interaction, which is driven by the internal electric field that interacts with the charges within the exciton [123], generated by the longitudinal vibrational motion of the lattice [132, 133]. In contrast, coupling with acoustic phonons primarily occurs via the deformation potential interaction [134]. In Section 1.1, the formation of the electronic band structure arising from the periodic arrangement of atoms is discussed. Long-wavelength acoustic phonons modify this periodicity by inducing atomic displacements that correspond to deformations and strains within the crystal lattice [86], which significantly influences the electronic band structure of the crystal [135]. In NCs, both excitons and phonons are confined, where only phonons with wavelengths comparable to the NC size can interact effectively with the exciton [70]. As a result, the quantum confinement of acoustic phonons can be observed via low-frequency Raman scattering [70].

In Section 1.6, inelastic scattering on phonons is introduced through resonant Raman scattering. Light-scattering experiments are predominantly performed with photons in the visible range, exhibiting a relative energy difference of approximately 1–10% compared to the phonons. Consequently, the momentum transfer in the scattering process is small, leading to the optical excitation of phonons near $k = 0$. [136]

1.6.2 Resonant Raman scattering

Inelastic (Raman) scattering is a weak phenomenon compared to elastic (Rayleigh) scattering, as typically only one in 10^6 to 10^8 photons is inelastically scattered [137, 138]. To enhance the scattering efficiency, the laser can be tuned into the resonance of the electronic interband transition, a technique known as resonant Raman scattering [86]. As a result, the intensity of the scattered light can be increased by up to eight orders of magnitude compared to non-resonant Raman scattering, significantly improving the signal-to-noise ratio [138]. Resonant light scattering serves as a powerful method for investigating excitons and their interaction with phonons in semiconductors [123].

The kinetics of any scattering process are governed by the conservation of energy and momentum, expressed as

$$\hbar\omega_\mathrm{s} = \hbar\omega_i \pm \hbar\omega_\mathrm{phonon}, \tag{1.15}$$

$$\mathbf{k}_\mathrm{s} = \mathbf{k_i} \pm \mathbf{q}_\mathrm{phonon}, \tag{1.16}$$

where the subscripts *i* and s refer to the initial and scattered frequencies ω and wave vectors $\mathbf{k}, \mathbf{q}$, respectively. The phonon frequency and wave vector sign determines whether the energy of the emitted photon is reduced or increased, thus distinguishing between Stokes scattering and anti-Stokes scattering, shown in Figure 1.7 [136]. In resonant Raman scattering, the absorption of a photon induces a transition from the ground state $|G\rangle$ to an excited state. In a typical experiment, a spectrally narrow laser is used so that resonance conditions may be met for either the Stokes or anti-Stokes process but not necessarily for both. However, since the spectral broadening of the optical excitation exceeds the energy splitting of the excited states between the Stokes and anti-Stokes processes, resonance conditions can be simultaneously satisfied for both processes.

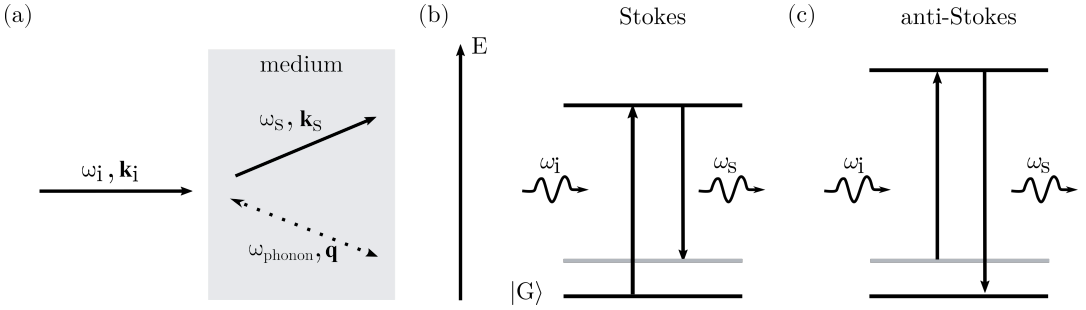

Figure 1.7: (a) Schematic of resonant inelastic scattering of light. Solid lines represent photons with frequencies $\omega_{i,s}$ and wave vectors $\mathbf{k}_{i,s}$, where the subscripts denote the initial and scattered states, respectively. The dotted line depicts a phonon with frequency ω_{phonon} and wave vector $\mathbf{q}$. The (anti)-Stokes processes, which involve phonon absorption or emission, are indicated by a bidirectional arrow. Adapted from [76]. (b) Stokes and (c) Anti-Stokes processes with ground state $|G\rangle$ and excited states. The excitation energy is indicated by an upward arrow and the scattered energy by a downward arrow. Adapted from [139].

Raman scattering typically involves an inelastic scattering process mediated by optical phonons. In sufficiently large scattering samples, such as bulk crystals, the condition for momentum-conservation (see Equation (1.16)) strictly applies [140]. In these systems, momentum conservation restricts Raman-active modes to zone-center modes, resulting in effectively zero Raman intensities for acoustic phonons. In contrast, in confined systems such as NCs, the conservation of momentum for the scattering process breaks down, enabling the observation of confined acoustic phonons through (low-frequency) Raman scattering [67, 141], as observed in $CsPbBr_3$ and $CsPbI_3$ NCs in Section 5.2.

1.6.3 Spin-flip Raman spectroscopy

In spin-flip Raman scattering (SFRS), inelastic light scattering is accompanied by the inversion of the spin orientation of one or more charge carriers in the presence of a magnetic field. In lead halide perovskites like $CsPbBr_3$ [142], $FA_{0.9}Cs_{0.1}PbI_{2.8}Br_{0.2}$ [18] and $MAPbI_3$ [143], the presence of resident carriers weakly localized at different crystal sites has been demonstrated. These carriers can originate from unintentional doping in solution-grown crystals or photogeneration [142]. In general, various processes can mediate a spin-flip (SF), including exciton-acoustic phonon interactions [144], carrier-carrier interactions [22], and isotropic exchange interactions [145]. The dominant SF mechanism depends on the specific properties of the investigated material. In this thesis, the spin inversion of resident carriers is expected to represent the main contribution to the spin-flip Raman process in three-, two- and zero-dimensional lead halide perovskite structures, as discussed in Chapters 3–5. A schematic SF process based on resident carriers is

presented in Figure 1.8(a). First, the incident photon excites an electron-hole pair, where the photon energy is tuned into resonance with the electron-hole transition, thereby enhancing the scattering efficiency, as discussed in Section 1.6. The SFRS processes involving resident carriers are mediated by excitons interacting with localized resident carriers, forming an intermediate three-particle state composed of an exciton plus a localized resident carrier [146]. Due to a spatial overlap between the wave functions of the resident carrier and the photoexcited carriers, an exchange interaction may occur, thereby inducing a SF of the resident carrier [24]. As a result, the resident carrier changes its spin orientation from its initial to its final state. The SF requires either the absorption or emission of the energy equal to the Zeeman splitting, depending on the direction of the SF. A SF from the lower to the upper energy level results in a Stokes shift, while a SF from the upper to the lower level leads to an anti-Stokes shift. In the final step, the electron and hole recombine radiatively, emitting a photon whose energy is shifted by the Zeeman splitting relative to the energy of the initial photon. Consequently, a SFRS spectrum exhibits SF peaks shifted from the laser energy (referred to as zero energy) to the Stokes and anti-Stokes sides due to the Zeeman splitting. This shift relative to the laser energy is known as the Raman shift, as illustrated in Figure 1.8(b). The SFRS spectra are measured in the vicinity of the laser line, extending towards lower energies (Stokes, positive Raman shift) and higher energies (anti-Stokes, negative Raman shifts) [147]. Note that in Figure 1.8(a), the SFRS for a single carrier is presented. However, it is also possible to observe the Raman shift corresponding to twice the carrier Zeeman splitting in the SFRS spectra, referred to as a double SF, which requires the presence of at least two resident carriers localized at different sites within the material [146]. In addition, simultaneous SFs of both localized electrons and holes, denoted as combined SFs, have been reported in bulk [62] and 2D lead halide perovskites [15]. However, the observation of both combined and double SFs is extremely rare, as their intensities are about an order of magnitude lower than those of single SFs due to the lower efficiency of the higher-order processes involving an additional carrier [31, 37].

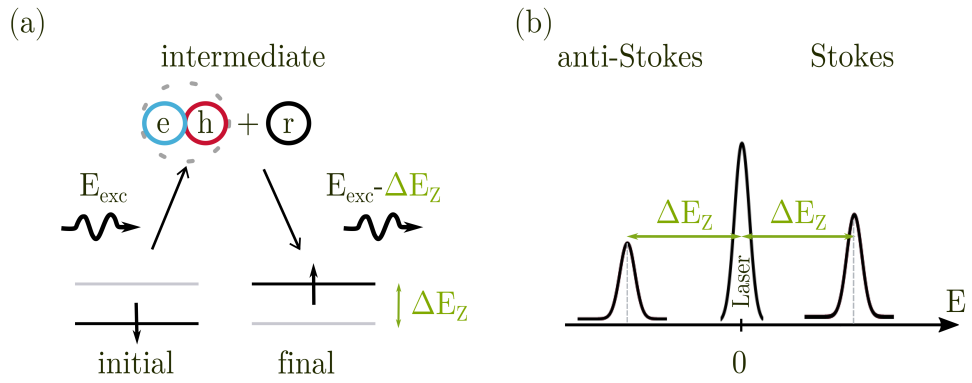

Figure 1.8: (a) Schematic illustration of the SFRS mechanism (Stokes process) based on the interaction between a photogenerated exciton (indicated by gray dashed line encircling the electron (e) and hole (h)) with a resident carrier. The process involves: (1) excitation of an electron-hole pair, (2) SF between Zeeman split sublevels of the resident carrier, and (3) emission of a photon with an energy reduced by the Zeeman energy ΔE_Z. Figure adapted from [74]. (b) Resulting SFRS spectrum for $B \neq 0$: The laser energy is set to zero, with SF peaks appearing on anti-Stokes and Stokes sides, shifted away from the laser energy by the Zeeman energy ΔE_Z.

With the technique of SFRS, we can determine the g-factors of charge carriers by measuring the Raman shift as a function of the magnetic field strength B and applying the Zeeman equation $\Delta E_Z = g\mu_B B$. In general, extrapolating the Raman shift to zero magnetic field reveals a negligible

offset. If a nonzero offset is observed, it indicates the influence of external factors, such as an exchange interaction between the involved carriers [31]. It should be noted that from the Raman shift alone, the underlying SF process cannot be fully revealed, especially when the g-factors of different carriers are identical. Therefore, it is necessary to concentrate on other SFRS parameters to gain an understanding of the underlying SF process.

Insights into the SF process can be gained by analyzing the selection rules for electric-dipole transitions in the presence of an external magnetic field. As discussed in Section 1.3, circular polarization is preferred in Faraday geometry to probe the pure eigenstates, while linear polarization in Voigt geometry is used to analyze the mixed states. To determine polarization selection rules, all four (circular/linear) polarization configurations are measured, and the corresponding SF intensities are compared. Note that the intensity of the anti-Stokes SF is typically weaker than that of the Stokes process, as the anti-Stokes process has a lower probability due to the Boltzmann distribution of populated spin sublevels [29]. In tilted geometries, the polarization selection rules are weakened [27], enabling SFs to appear in additional polarization configurations, depending on the strength of mixing between the exciton states [24]. In the experiment, to determine the carrier g-factors, a crossed polarization configuration for excitation and detection is typically used to minimize laser stray light in the SFRS spectra. This polarization configuration enables the observation of SFs even close to the laser line without being hidden by a significant background of stray light. It is important to note that any initial change of the SF peak intensity might originate from variations in the background signal beneath the peaks. On anti-Stokes side, contributions from the photoluminescence (PL) are negligible at low temperatures, enabling a clear identification of the SFs [62]. In contrast, the Stokes side often displays a background arising from resonant PL. Therefore, it is essential to take the relative peak intensity into account to distinguish them from the background contributions. The fitting procedure for the SFRS spectra is demonstrated in Section 2.3.

SFRS experiments are typically performed in backscattering geometry, where the propagation directions of the incident and scattered light are opposite. The differential cross-section for backscattering in Faraday geometry is defined by [140]

$$\frac{d\sigma}{d\Omega} \propto \left|(\mathbf{e}_\mathrm{s} \times \mathbf{e}_\mathrm{i}) \times \mathbf{B}\right|^2, \tag{1.17}$$

with the unit vector $\mathbf{e}_{\mathrm{s,i}}$ of the electric field directions $E_{s,i}$ for the incident and scattered light. For Faraday geometry, Equation (1.17) only differs from zero if the magnetic field has a nonzero component perpendicular to the light propagation direction [61]. Thus, the observation of SFs is forbidden in pure Faraday geometry. Tilting the magnetic field so that the spin quantization direction is no longer aligned with the direction of the incident light [61], leads to an increase in the SF probability and relaxes the restrictions imposed by the selection rules. To quantify the relative amplitudes of SFs in various polarization configurations in Chapter 3, the Kramers-Heisenberg equation [148]

$$A(E_k) = \sum_{|n\rangle} \left| \frac{\langle f|\hat{\mu}|n\rangle\langle n|\hat{\mu}|i\rangle}{E_i - E_n + E_k + i\frac{\Gamma_n}{2}} \right|^2 \delta(E_i - E_f + E_k - E_k') \tag{1.18}$$

is used. The Kramers-Heisenberg equation describes the probability of photon emission with energy $E_{k'}$, after the excitation with photons of an energy E_k. The initial, intermediate, and final states are denoted by $|i\rangle, |n\rangle, |f\rangle$, with energies E_i, E_n, and E_f, respectively. The dipole operator for the transition is represented by $\hat{\mu}$, and Γ denotes the intrinsic line width of the intermediate state. As discussed in Section 1.6, the line width of the intermediate state is small compared to excitation.

2 Experimental methods

This chapter introduces the experimental setups for characterizing the optical properties of the lead halide perovskite samples, including stationary and time-resolved photoluminescence, absorption and reflectivity spectra, and spin-flip Raman scattering with high spectral resolution. A description of the composition of the studied three-dimensional, two-dimensional, and zero-dimensional lead halide perovskite structures is given in Section 2.2. Further, Section 2.3 describes the fitting procedure for analyzing the Raman spectra used in Sections 3-5.

2.1 Experimental setups

2.1.1 Photoluminescence, absorption and reflectivity spectroscopy

The photoluminescence (PL), absorption, and reflectivity spectra of the studied samples are measured to characterize their optical properties using the experimental setup schematically shown in Figure 2.1. This characterization serves to identify the exciton resonance, thereby providing a reference point for selecting the excitation energy for spin-flip Raman scattering (SFRS). For the PL measurements, the sample is excited by a continuous-wave laser in the blue spectral range with an energy of 3.49 eV, which exceeds the band gap energy of all studied samples. A white light lamp is used to measure the absorption and reflectivity spectra. Depending on the spectral range of interest, the material of the white light source, such as halogen or deuterium lamps, is selected to provide a continuous spectrum within that range. The white light is directed in two ways: either it passes through the sample to measure absorption spectra, or it illuminates the sample from the front, enabling the measurement of reflectivity spectra.

A half ($\lambda/2$)- or quarter ($\lambda/4$)-wave plate and a Glan-Thompson (GT) prism are placed in the detection path, if the polarization properties of the PL, absorption, or reflectivity spectra are of interest. The emitted or reflected light is collected by a lens and focused on the entrance slit of a spectrometer (Princeton Instruments Acton SP2500i). This spectrometer is equipped with a charge-coupled device (CCD) that converts the incoming photons into an electrical signal. The CCD is cooled down to $-120\,^{\circ}\mathrm{C}$ using liquid nitrogen to reduce the dark current (noise) of the individual pixels. A major advantage of the CCD camera is that large spectral ranges can be measured at once, thereby significantly reducing the data acquisition time. The spectrometer is equipped with three different gratings: 300, 600, and 1200 grooves per millimeter. The 1200 grooves per millimeter grating provides the highest resolution, reaching 0.3 meV [149].

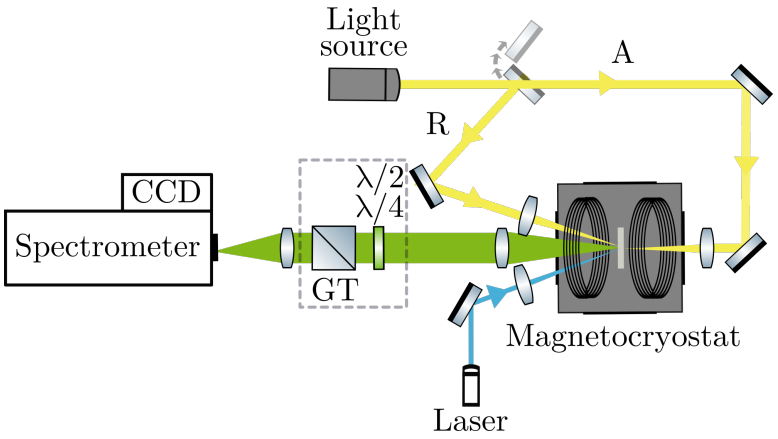

Figure 2.1: Scheme of the experimental setup for measurements of PL, absorption (A), and reflectivity (R) spectra. By flipping the mirror directly after the white light source, both absorption and reflectivity spectra can be measured with this setup. A $\lambda/2$- or $\lambda/4$-wave plate and a Glan-Thompson (GT) prism are positioned in the detection path for polarization-dependent measurements (enclosed by gray dashed line).

2.1.2 Time-resolved photoluminescence

The PL dynamics of excitons in perovskites are analyzed to identify the different contributions to the radiate recombination channels in the PL spectra based on their characteristic lifetimes. The idea is to measure the PL intensity as a function of time after the laser pulse. Therefore, the experimental setup for stationary PL measurements, illustrated in Figure 2.1, is extended with a pulsed laser (Laser2000), synchronized with a time-resolved detection system, along with a function generator (Tektronix AFG3022), to measure PL dynamics in the µs range. The PL dynamics are typically measured at the PL maximum or exciton resonance, with the detection wavelength selected by the U1000. For single photocounting, the photomultiplier tube (PMT) detects light dispersed by the double-spectrometer U1000, and the amplified signal is sent to a multiple-event time digitizer MCS6A from Fast ComTec GmbH. The MCS6A provides a nominal time resolution of 100 ps per time interval [150]. Photocounting is synchronized with the laser pulses by a function generator operating in rectangular mode.

2.1.3 Spin-flip Raman spectroscopy

This section introduces the experimental setup for SFRS. The setup is schematically shown in Figure 2.2. The efficiency of an inelastic scattering process such as SFRS is maximized when the samples are optically excited at the exciton resonance, as discussed in Section 1.6. Therefore, a laser that is spectrally narrow and has good tunability across a broad energy range is required. Depending on the band gap energy of the investigated sample, different parts of the laser system are used (see the part in Figure 2.2 enclosed by gray dashed line). As most of the investigated samples have exciton resonances in the green spectral range, a continuous-wave TiSa laser (Matisse-CR, Sirah) and a fiber laser with a fixed wavelength of either 1950 nm or 1550 nm are used to provide the optical excitation of the samples. In the MixTrain, the sum frequency of the tunable single-frequency titan sapphire laser and the fiber laser is generated, covering an energy range from $1.77 - 2.58$ eV. In addition, for specific samples, excitation in the blue and infrared ranges is achieved through the second harmonic generation (SHG) unit or the TiSa laser. The laser intensity can be continuously adjusted with a combination of a $\lambda/2$-plate and a GT prism.

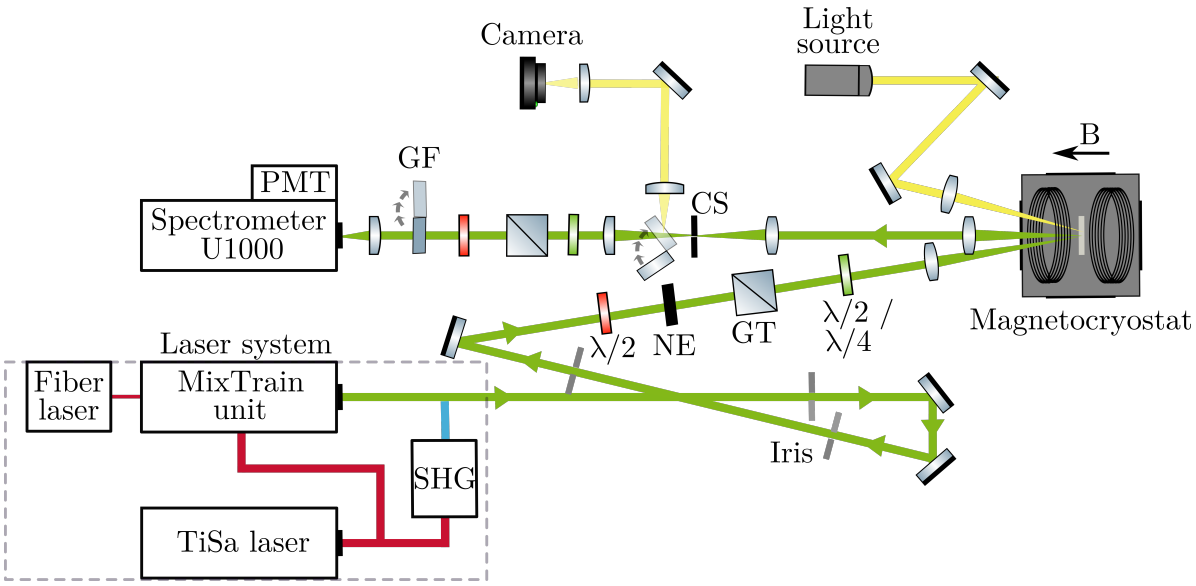

Figure 2.2: Scheme of the experimental setup for spin-flip Raman spectroscopy as described in detail in the text. Abbreviations: Second harmonic generation (SHG) unit, titan-sapphire (TiSa) laser, noise eater (NE), Glan-Thompson (GT) prism, cross slit (CS), and gray filter (GF). The different laser units within the laser system (enclosed by gray dashed line), with the mirrors used for the laser units omitted for simplicity.

The $\lambda/2$-plate rotates the polarization axis of the linearly polarized laser light. By rotating the half-wave plate relative to the transmission axis of the GT prism, the intensity of the transmitted light can be regulated. To minimize the laser stray light entering the spectrometer and ensure that only the scattered light from the sample is analyzed, a second GT prism, cross-polarized with respect to the GT prism in the excitation path is placed in the detection path.

During the scan of a SFRS spectrum, the spectrometer sequentially measures the intensity at each wavelength. Consequently, maintaining a stable laser intensity throughout the scan is essential. To achieve this, a combination of a $\lambda/2$-plate and a liquid crystal noise eater (NE) from Thorlabs is used. The NE, combined with an internal photodiode for power measurements and a feedback control circuit, provides amplitude stabilization within 0.05 % of the selected output power [151]. For operation, the NE requires linearly polarized input light, which is ensured by the aforementioned half-wave plate. A $\lambda/2$- or $\lambda/4$ retardation plate is used to selectively excite the sample with linear or circular polarization. A lens with a focal length of 250 mm is used to focus the laser light to a spot diameter of roughly 300 µm on the sample.

The sample is placed inside the variable temperature insert (VTI) of a helium bath cryostat, where temperatures of 1.6 K (superfluid phase of helium) can be reached by reducing the pressure to several millibars. A split-coil superconducting magnet immersed in liquid helium generates magnetic fields up to 10 T. Optical windows on each side of the cryostat provide optical access to the sample. The sample in the magnetocryostat can be oriented in either Faraday geometry (longitudinal magnetic field), where the magnetic field $\mathbf{B}$ is aligned with the sample's quantization axis z ($\mathbf{B} \parallel z$), or in Voigt geometry, where the magnetic field is applied transversely. The direction of light propagation $\mathbf{k}$ is assumed to be parallel to the sample's quantization axis ($\mathbf{k} \parallel z$). By manually rotating the sample holder, angles with an accuracy of $\pm 2^\circ$ between Faraday and Voigt geometry can be achieved, enabling measurements of the g-factor anisotropy, i.e., the dependence of the g-factor on the angle of rotation relative to the magnetic field. As discussed in Section 1.6.3,

the observation of spin-flips (SFs) is restricted in pure Faraday geometry. In the experiment, pure Faraday geometry is not achievable, as the wave vector k of the incident light forms a small angle with the magnetic field, which is approximately 5°. Within the sample, the wave vector remains nearly conserved due to the small difference in refractive indices between liquid helium ($n = 1.00$, [152]) and, for example, $CsPbBr_3$ ($n = 1.5$, [153]). Therefore, we refer to the configurations as Faraday and Voigt geometries, and a SF signal might be observed in Faraday geometry.

In backscattering geometry, the inelastically scattered light from the sample is collected by a lens with a focal length of 250 mm. The focal length of the lens is selected to position it as close to the sample as possible, optimizing the collimation of the scattered light. However, its placement is constrained by the external dimensions of the cryostat. The collimated light is then focussed on a cross slit by a second lens. To adjust the laser position on the sample, white light illuminates the sample, and the resulting image is recorded by a camera. Therefore, a flip mirror can be placed in the detection path to redirect the light through a collecting lens onto the camera. After confirming that the laser remains consistently focused on the same position on the sample for all measurements, the cross slit is minimized to the size of the laser spot to ensure that only scattered light from that specific part of the sample is detected. The mirror is then flipped back.

For detection, the linear polarization of the light entering the spectrometer is adjusted by a $\lambda/2$-plate (see Figure 2.3), as the diffraction efficiency depends on the polarization of the light relative to the grating grooves [154] and the grating's blaze wavelength. According to the U1000 manual [155], the maximum diffraction efficiency is achieved when the light is polarized perpendicular to the grating grooves for wavelengths above 500 nm, while for shorter wavelengths, parallel polarization provides higher efficiency.

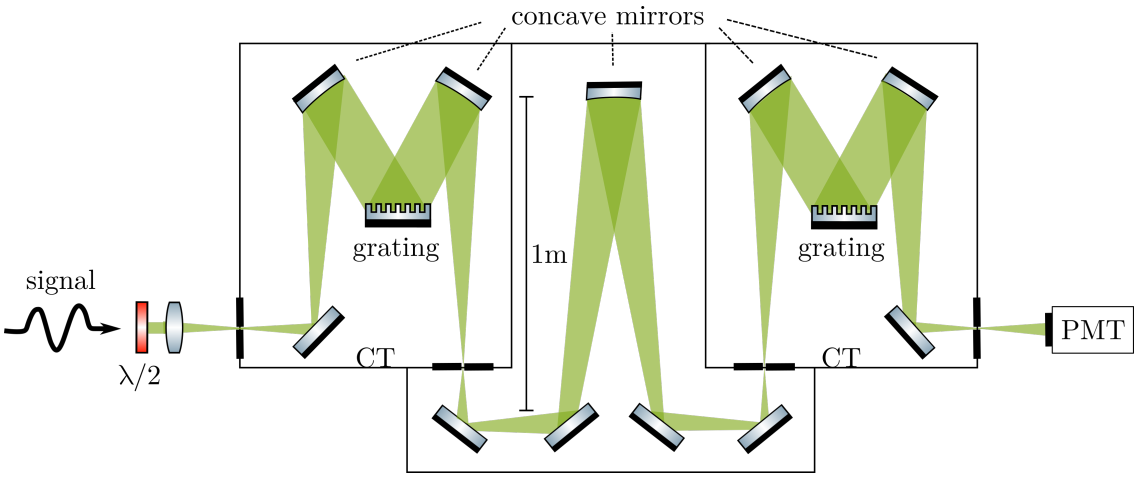

Figure 2.3: Scheme of the light pathway in the U1000 spectrometer, consisting of two identical monochromators arranged in an asymmetric Czerny-Turner (CT) configuration and equipped with plane holographic grating. Figure adapted from [156].

The light is focused by a lens onto the entrance slit of the double monochromator (Horiba Yobin-Yvon U1000), whose operating principle is schematically shown in Figure 2.3. The U1000 is composed of two identical monochromators arranged in an additive mount. Each monochromator is designed as an asymmetric Czerny-Turner (CT) configuration, comprising two mirrors, the first for collimating light and the second for focusing it, along with a plane holographic grating [140]. In the first monochromator stage, the incoming light is collected by a spherical mirror and directed towards the optical grating, where it is horizontally dispersed into its constituent

wavelengths. The diffracted light is then collected by a second spherical mirror and focussed onto the intermediate slit. To suppress stray light, an additional optical path between the first and second monochromator stage includes a spherical intermediate mirror located at the focal points of the intermediate slits. The exit slit of the first monochromator stage is imaged on the entrance slit of the second monochromator by a concave mirror. The light undergoes further dispersion in the second monochromator stage before being detected from a Peltier-cooled gallium arsenide (GaAs) PMT (Hamamatsu R943-02), which is optimized for the detection of weak signals [157]. GaAs-coated photocathodes exhibit a strong response, characterized by high quantum efficiency, from 400 nm up to 900 nm [140]. The operation of a PMT is based on the photoelectric effect, in which electrons are emitted from the surface of the photocathode material when illuminated by light. These emitted electrons are accelerated by an electric field created by applying a high voltage of 1900 V and multiplied through secondary emission. The electron current output of the PMT is sent to a pulse-shaping preamplifier (F-100T Advanced Research Instruments Corporation), which generates pulses with a fixed width and amplitude proportional to the number of incident photons. In addition, the built-in discriminator filters out low-amplitude pulses caused by thermal electrons [140], thereby enhancing the signal-to-noise ratio and ensuring that only signal pulses are counted by the spectrometer's control unit. The resolution of the spectrometer is mainly determined by the focal length, grating, and the sizes of the entrance and exit slits [140]. For this work, slit sizes of 70/150/150/70 µm are primarily used, depending on the required spectral resolution and signal intensity, in combination with two gratings with 1800 grooves per millimeter. These gratings cover a spectral range from $450 - 850$ nm and achieve a maximum resolution of 0.15 cm^{-1}(19 µeV) [155].

As SFRS spectra are measured over a range from several tens of µeV to a few meV from the laser line, and the laser line itself must also be recorded to determine the Raman shift, it is essential to protect the PMT from the intense laser light. This is accomplished by manually placing a neutral density filter in front of the U1000 while scanning the detected wavelength of the laser.

2.2 Description of samples

This section presents a brief description of the studied lead halide perovskite samples and their synthesis based on the protocols provided by the respective synthesis groups.

2.2.1 Bulk $MAPbI_3$ single crystals

Bulk $MAPbI_3$ single crystals were grown in the group of M. Kovalenko at ETH Zürich. The perovskite precursors, MAI and PbI_2, were injected between polytetrafluoroethylene-coated glass substrates and slowly heated to 120 °C, where the $MAPbI_3$ single crystals formed. By controlling the ratio of MAI to PbI_2, $MAPbI_3$ single crystals with a preferred orientation were obtained [158]. The resulting sample has approximate dimensions of 2:2 mm with a thickness of 23.1 µm along the (001) direction and exhibits a black color. Room temperature X-ray diffraction analysis revealed a tetragonal crystal phase.

2.2.2 2D Ruddlesdon-Popper type perovskites

The experiments described in Chapter 4 are performed on Ruddlesdon-Popper (RP) type 2D perovskites of the composition $PEA_2(MA, FA)_{n-1}Pb_nX_{3n+1}$, where X = Br, I, deposited on glass

substrates. The samples contain a mixture of different n phases, where n denotes the number of inorganic layers (lead halide octahedra). The exact ratio of the n-phases within a sample is unknown. The synthesis process of these materials prepared within the group of M. Kovalenko at ETH Zürich are outlined below.

$(PEA)_2FA_{n-1}Pb_nI_{3n+1}$ thin films

For the synthesis of the $(PEA)_2FA_{n-1}Pb_nI_{3n+1}$ thin films, (PEA)I, (FA)I and PbI_2, were dissolved in N,N-dimethylformamide in the stoichiometric molar ratio to prepare a solution of 8.3 wt. % concentration of $(PEA)_2FA_{n-1}Pb_nI_{3n+1}$. Inside a nitrogen-filled glovebox, the solution was spin-coated on glass substrates for 5 s at 400 rpm, followed by 30 s at 3000 rpm. The samples were then annealed on a hot plate at 100 °C for ten minutes.

$(PEA)_2(MA)_{n-1}Pb_nI_{3n+1}$ single crystals

The synthesis of $(PEA)_2(MA)_{n-1}Pb_nI_{3n+1}$ single crystals is based on the cooling method described in Reference [159]. Precursors, including lead oxide, methylammonium iodide, and phenethylamine, were dissolved in hydriodic acid at specific molar ratios and maintained at approximately 110 °C for 4 h. The solutions were then gradually cooled to room temperature at a controlled rate of 1 °C per hour. The molar ratios of lead oxide, methylammonium iodide, and phenethylamine in the sample were 10/24/1 mmol, respectively. The obtained crystals were filtered under vacuum and then dried with diethyl ether.

$(PEA)_2FA_{n-1}Pb_nBr_{3n+1}$

A precursor solution was prepared in the glovebox using 40 mg PEABr, 12.5 mg FABr, and 73 mg $PbBr_2$. The components were dissolved in 2 mL of anhydrous DMF and stirred overnight. The quartz substrates were sequentially washed with soap, water, acetone, and isopropanol for 10 min each at 50 °C under sonication. They were then treated in an ozone cleaner for 10 min. The substrates were immediately transferred to the glovebox, where 50 µL of the precursor solution was spin-coated at 3000 rpm for 30 s. The films were subsequently annealed at 100 °C for 10 min.

2.2.3 Nanocrystals

The synthesis of $CsPbBr_3$ and $CsPbI_3$ nanocrystals (NCs) is described below, along with an initial characterization of their sizes. The $CsPbBr_3$ NCs were synthesized by M. Kovalenko's group at ETH Zürich, while the $CsPbI_3$ NCs were synthesized by E. Kolobkova at ITMO University. The $CsPbI_3$ NCs exhibit a broader size distribution ($4-13$nm), than $CsPbBr_3$ NCs ranging from $8-11$nm. In addition to variations in size distribution and halide composition, $CsPbBr_3$ NCs are synthesized in solution, whereas $CsPbI_3$ NCs are embedded in a glass matrix. Notably, the surfaces of NCs in glass are free from organic ligands [160] and can be easily polished to achieve surfaces with high optical properties [161].

$CsPbBr_3$ nanocrystals grown in solution

Details of the growth method for the $CsPbBr_3$ NCs were adopted with minor modifications from Reference [49]. There, a novel strategy is presented, which involves combining cationic and anionic groups into a single zwitterionic molecule, such as 3-(N,N-dimethyloctadecylammonio) propanesulfonate. This approach results in efficient surface ligand capping of $CsPbBr_3$ NCs. First, solutions of caesium-oleate and lead-oleate octadecene (ODE), along with 1.5 mL TOP-Br_2, were prepared. Second, in a three-neck flask equipped with a stir bar, 107.5 mg of the long-chain sulfobetaine ASC18 (3-(N,N-dimethyloctadecylammonio) propanesulfonate, $\geq$ 99%), 1.2 mL caesium-oleate, 1.5 mL lead-oleate and 5.5 mL ODE were combined. The mixture was evacuated and refilled with nitrogen three times, then heated to 130°C under a nitrogen atmosphere. Adding 1.5 mL of TOP-Br_2 under stirring resulted in the formation of a yellow solution. Then the solution was rapidly cooled to room temperature in an ice-water bath and subjected to centrifugation at 12.1 krpm for 10 min. The supernatant was taken into another centrifuge. The amount of ethyl acetate (EtOAc) was varied to grow nanocrystals of different sizes. This set of $CsPbBr_3$ NCs includes three samples (#1-#3) with varying NC sizes, identified by their technical codes Yes1408A, Yes1408B, and Yes1408C, respectively. For sample #1, 20 mL of EtOAc was added to the supernatant and centrifuged at 12.1 krpm for 10 min. For sample #2, an additional 10 mL of EtOAc was added and sample #3 was prepared with a total of 40 mL of EtOAc. All centrifuged at 12.1 krpm for 10 min to remove insobules. All precipitates were dispersed in 2 mL of anhydrous toluene in a glovebox and centrifuged at 14.5 rpm for 3 min to eliminate turbidity and big particles. For the optical experiments, the solutions were drop-cast onto glass substrates.

The NC sizes were determined by absorption measurements at ETH Zürich to be 11.1 nm for sample #1, 9.6 nm for sample #2 and 7.9 nm for sample #3. The exciton Bohr radius in $CsPbBr_3$ bulk crystals is estimated to be approximately 7 nm [162].

$CsPbI_3$ nanocrystals in glass

The studied $CsPbI_3$ NCs embedded in fluorophosphate $Ba(PO_3)_2$-AlF_3 glass were synthesized using a melt-quench technique. In this process, the glass melt, enriched with the necessary components for the perovskite crystallization, is rapidly cooled [66]. Details of the method are provided in Reference [50]. The glass, with the composition $35P_2O_5$–35BaO–$5AlF_3$–$10Ga_2O_3$–$10PbF_2$–$5Cs_2O$ (mol. %) doped with BaI_2, was melted at 1050 °C in a closed crucible for 20 min − 30 min. After melting, the glass was cast and pressed into plates of 2 mm thickness, then annealed at 50 °C to relieve internal stresses.

$CsPbI_3$ NCs formed during pouring out of transparent melt, with their sizes controlled by the iodine concentration and cooling rate of the melt. Due to the high tendency of iodine compounds to evaporate and the low viscosity of the glass-forming fluorophosphate melt at elevated temperatures, extending the synthesis time results in a decrease in the iodine concentration within the equilibrium melt. As a result, the original composition can be preserved while only adjusting the iodine concentration, enabling the growth of NCs of varying sizes through modification in the synthesis duration [161]. In this thesis, four samples labeled as #1, #2, #3 and #4, corresponding to their respective technology codes, EK8, EK201, EK203 and EK205, are investigated. These NCs differ in size, as evidenced by the relative spectral shifts in their optical spectra, with sizes ranging from 4 to 13 nm. The exciton Bohr radius in $CsPbI_3$ bulk crystals is estimated to be approximately 12 nm [162]. Section 5.2 introduces an alternative method to determine the NC size, based on the phonon energy of optically-active confined acoustic phonons.

2.3 Spectra analysis

The fitting procedure for determining the Raman shifts of SFs and phonons is demonstrated in Figure 2.4 by an exemplary SFRS spectrum on anti-Stokes side. First, any background contributions arising from stray light or resonant PL are subtracted, as indicated by the red dashed line in Figure 2.4(a), resulting in the spectrum shown in Figure 2.4(b). Next, the peak positions of the SF signals and the laser line are determined through Gaussian fits of the form

$$f(x) = A\mathrm{e}^{\left(-\ln(2)\frac{(x-x_0)^2}{dx^2}\right)}, \tag{2.1}$$

where A denotes the amplitude, x_0 the center and dx the half width at half maximum of the Gaussian. To measure the resonance profile and identify the exciton resonance, where the SF intensity typically reaches its maximum, the amplitude A is evaluated for varying excitation energies. The focus of this thesis is set on determining the g-factors for electrons and holes in three-, two-, and zero-dimensional lead halide perovskites. Therefore, the energetic positions of the Gaussian fit x_0, relative to the laser line, denoted as Raman shift ΔE are plotted against the magnetic field B. The g-factor is derived from the slope of a linear fit by the Zeeman equation

$$\Delta E = g\mu_\mathrm{B}B. \tag{2.2}$$

In general, it is assumed that the linear fit has no offset due to exchange interactions [31]. The linewidth of the SFs is limited by the spectral width of the laser and the resolution of the spectrometer, which together define the minimal detectable SF width. Thus, Equation (2.1) provides an effective fit for both the laser and SF peaks. The evaluation of the SFRS and resonant Raman spectra in Chapters 3-5 follows this analysis procedure. However, not all spectra are presented in such a way that the background is subtracted.

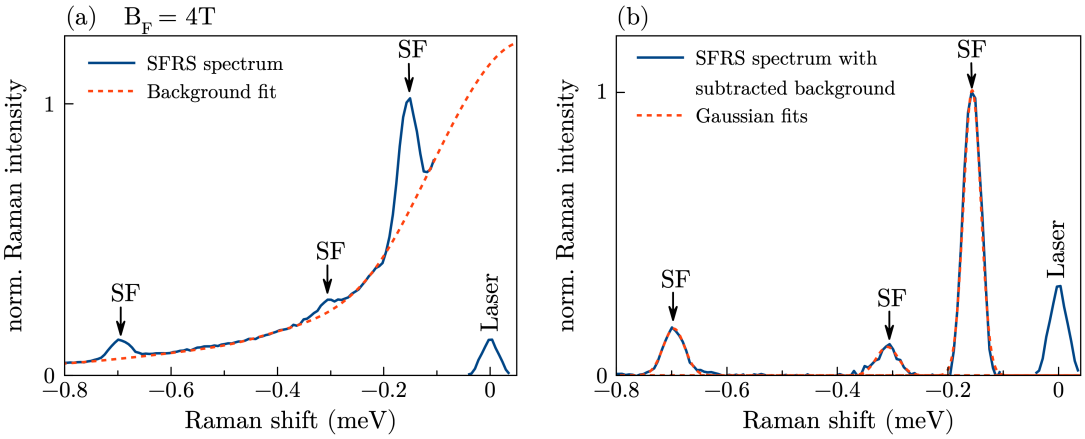

Figure 2.4: SFRS spectra analysis: (a) Fitting of the background, (b) SFRS spectrum with subtracted background to determine the Raman shifts of the SFs using Gaussian fits based on Equation (2.1) (red dashed lines).

Spin-flip Raman spectroscopy of bulk $MAPbI_3$ single crystals

3

In this chapter, the technique of spin-flip Raman spectroscopy is applied to a bulk $MAPbI_3$ single crystal. From the strongly polarization-dependent spin-flip Raman scattering (SFRS) spectra, we perform a systematic polarization analysis based on a simplified model to identify the optical selection rules for both Faraday and Voigt geometries. In addition, we observe not only single spin-flips but also combined spin-flips, as well as double electron and hole spin-flips, which are a distinct feature of perovskites due to their abundance of resident electrons and holes. SFRS provides access to structural domains and their orientations. Spin-flips (SFs) with smaller intensities, located near the electron and hole SF lines exhibit different g-factor anisotropy, which suggests that the sample consists of two orientations of orthorhombic domains.

3.1 Optical properties of $MAPbI_3$ single crystals

As a first step, we investigate the optical properties of a thin $MAPbI_3$ single crystal at a temperature of $T = 1.6\,\mathrm{K}$. The reflectivity (R) spectrum, shown in Figure 3.1(a), reveals an exciton resonance at $E_X = 1.636\,\mathrm{eV}$. At this energy, the transmission spectrum reaches saturation, indicating that the 23 µm thick sample is optically dense. As the energy decreases towards the tail of the exciton resonance, the sample gradually absorbs more light. The photoluminescence (PL) exhibits an asymmetric lineshape with a peak at 1.627 eV and full width at half maximum (FWHM) of 10 meV. The PL dynamics are measured near the exciton resonance at 1.631 eV, where the SFRS signals of the electron and hole reach their maximum (see blue and red dots, respectively, in Figure 3.1(a)). The long PL dynamics, extending up to 1.8 µs, are presented in Figure 3.1(b)) and consist of two exponential decay components, indicating the presence of multiple recombination processes. The faster component has a decay time of $\tau_1 = 80\,\mathrm{ns}$, whereas the slower component decays with $\tau_2 = 730\,\mathrm{ns}$. Exciton recombination is also expected but occurs on a much shorter timescale that cannot be resolved within the limits of this experiment. With the typical lifetime of bright excitons in this material reported as $\tau_X = 15 - 80$ ns [163], the significantly longer observed decay times suggest that the PL dynamics originate from recombination processes that involve spatially separated electrons and holes. A similar behavior has been observed in various lead halide perovskite structures [15, 18, 62]. Additional contributions to the long recombination dynamics are discussed in References [164, 165].

Applying a longitudinal magnetic field of $B_F = 8\,\mathrm{T}$ in Faraday geometry ($\mathbf{B}_F \parallel \mathbf{k} \parallel c$), the transmission spectrum exhibits a Zeeman splitting $\Delta E_{X,Z}$ of 1.1 meV, observed in Figure 3.1(c) as an energy shift between the σ^+ and σ^- polarized spectra. The Zeeman splitting of the bright exciton is defined as $\Delta E_{X,Z} = g_X \mu_B B$, where g_X is the bright exciton g-factor and μ_B is the Bohr magneton. In lead halide perovskites, the bright exciton g-factor is given by $g_X = g_e + g_h$, with g_e and g_h representing the electron and hole g-factors, respectively. Consequently, the Zeeman splitting of the band-to-band transition is expected to have the same value as the exciton Zeeman splitting. By extracting the energies of the Zeeman-split transmission spectra at different magnetic fields, a linear dependence is observed in Figure 3.1(d), which results in a bright exciton

g-factor of $g_X = +2.3$. The positive sign of the exciton g-factor is evident in Figure 3.1(c), as it corresponds to a higher energy shift of the σ^+ polarized transmission spectrum relative to the σ^- polarized transmission spectrum. The exciton g-factor is in good agreement with the previously reported $g_X = +2.3$ from magneto-reflectivity measurements in $MAPbI_3$ single crystals [143].

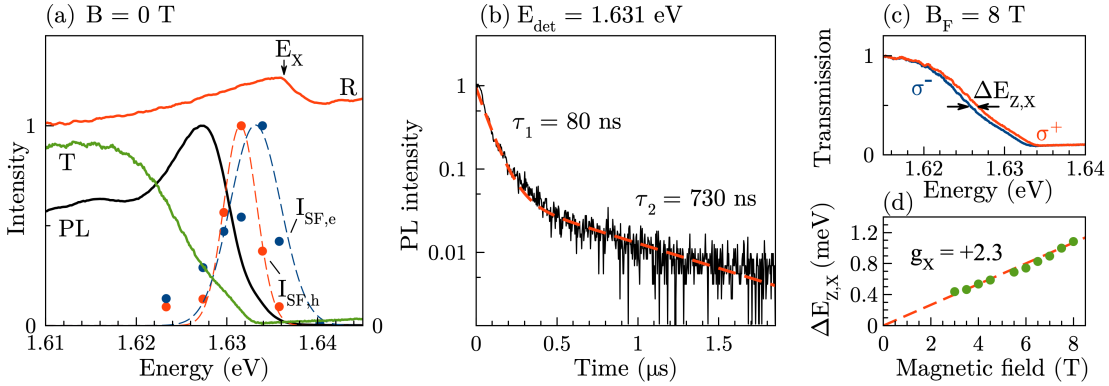

Figure 3.1: (a) Normalized PL (black), transmission (green), and reflectivity (red) spectrum of the studied $MAPbI_3$ crystal in zero magnetic field. Exciton resonance E_X is indicated by a vertical arrow in the reflectivity spectrum. Resonance profiles of the electron (blue) and hole (red) SF, with intensities denoted as $I_{SF,(e,h)}$. Dashed lines are guides for the eye. (b) Decay of the PL measured at the maximum of the resonance profiles for both the electron and hole, at an energy of $E_{det} = 1.631\,eV$, excited using a pulsed laser with energy $E_{exc} = 3.493\,eV$ at a laser repetition frequency of 4 kHz. Fit to a double exponential function (red line). (c) Zeeman splitting $\Delta E_{Z,X}$ of the transmission spectra in a longitudinal magnetic field of $B_F = 8\,T$. (d) Magnetic field dependence of the Zeeman splitting (green dots) and fit to a linear function (red dashed line).

3.2 Spin-flip Raman scattering of $MAPbI_3$ single crystals

We begin by systematically analyzing the SFRS spectra, first in Faraday geometry and then in Voigt geometry, with the excitation energy set to the exciton resonance. From the strongly polarized SFRS spectra, we perform a polarization analysis to identify optical selection rules. The g-factors of all carriers are determined, and their angular dependences are traced to reveal the orientation of the g-factor tensor for two structural domains with different orientations.

To resonantly excite the $MAPbI_3$ crystal, the excitation energy is tuned in the vicinity of the exciton resonance. By slightly adjusting the photon energy, the resonance profile of the SF intensity $I_{SF,(e,h)}$ for both electron and hole is obtained, as depicted by the blue and red dots, respectively, in Figure 3.1(a). Accordingly, an excitation energy of $E_{exc} = 1.633\,eV$, corresponding to the maximum of Raman scattering intensity, is selected to measure the SFRS spectra throughout this chapter.

3.2.1 Faraday geometry

In Figure 3.2(a) and (b), the SFRS spectra in Faraday geometry at $B_F = 4$ T are shown for different circular polarizations. As discussed in Section 2.1.3, the experimental geometry deviates slightly from pure Faraday geometry, enabling the observation of a SF signal. In particular, two SF lines can be identified on anti-Stokes and Stokes side. The smaller Raman shift of $|E_h| = 0.16$ meV corresponds to the SF of the hole, with a g-factor of $|g_h| = 0.66$, while the SF with the larger Raman shift of $|E_e| = 0.70$ meV corresponds to the electron, with $|g_e| = 3.00$. Both SFs are absent at zero magnetic field, as expected due to the vanishing Zeeman splitting. As the magnetic field increases, the SF lines shift linearly relative to the laser energy (referred to as zero), as shown in Figure 3.2(c), enabling us to calculate the g-factor values according to the Zeeman equation (Equation (2.2)). The assignment of the SF lines to the electron and hole is based on Reference [143]. There, time-resolved Kerr rotation (TRKR) measurements on $MAPbI_3$ single crystals yielded a hole g-factor of $g_h = -0.68$ and an electron g-factor of $g_e = +2.78$ was determined. While with SFRS the value of the g-factor can be accurately determined, a single SFRS spectrum does not provide any information on the g-factor sign. However, in Reference [143], the sign of the g-factor was determined through dynamic nuclear polarization (DNP), revealing that the electron and hole have opposite signs, with $g_e = +3.00$ and $g_h = -0.66$.

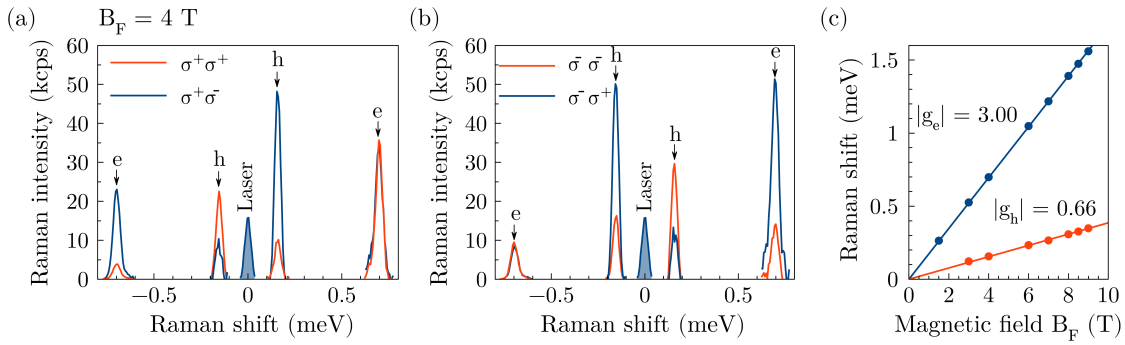

Figure 3.2: Polarization dependence of the electron and hole SFs in Faraday geometry at $B_F = 4$ T, excited at the exciton resonance of $E_{exc} = 1.633$ eV with a power density of $P = 0.6$ W/cm^2. (a) corresponds to σ^+ excitation, while (b) corresponds to σ^- excitation. Red represents co-circular polarization, and blue represents cross-circular polarization. (c) Magnetic field dependence of the electron and hole Raman shifts, along with the determined g-factors.

The SF intensities are measured for both co- and cross-circular polarizations at a magnetic field of $B_F = 4$ T, revealing strongly polarization-dependent SFRS spectra as shown in Figures 3.2(a) and (b). Here, the polarization configuration is represented by two letters, where the first one indicates the excitation polarization, and the second one denotes the detection polarization. To enhance the comparability of the SF peaks for different polarizations, the background is subtracted following the analysis procedure outlined in Section 2.3. We begin by analyzing the SFRS spectra presented in Figure 3.2(a) for σ^+ excitation. In this polarization configuration, the hole SF line on anti-Stokes side is most prominent in (σ^+/σ^+) polarization, whereas, on Stokes side, the hole SF is stronger in (σ^+/σ^-). The electron SF on anti-Stokes side exhibits an opposite behavior compared to that of the hole: the electron SF is stronger in (σ^+/σ^-) polarization configuration. On Stokes side, only a slightly larger signal in co-polarization (σ^+/σ^+) than in cross-polarization (σ^+/σ^-) is observed. For σ^- excitation, as presented in Figure 3.2(b), the hole shows the reverse trend. On anti-Stokes side, the SF intensity is stronger in cross-polarization (σ^-/σ^+), while on Stokes side, the intensity is greater in co-polarization (σ^-/σ^-). For the electron SF, the situation is again reversed compared to the hole: on Stokes side, the intensity is slightly larger in co-polarized

configuration, while on anti-Stokes side, cross-polarization (σ^-/σ^+) yields a stronger signal. To summarize and quantify the observed non-trivial behavior, the polarization degree for all SFs is calculated using [163]

$$PD = \frac{I_{\mathrm{co}} - I_{\mathrm{cross}}}{I_{\mathrm{co}} + I_{\mathrm{cross}}}, \tag{3.1}$$

where I_{co} denotes the intensity for co-circular polarization and I_{cross} for cross-circular polarization. A positive sign indicates a stronger signal in co-circular polarization, whereas a negative sign corresponds to a stronger signal in cross-circular polarization. The calculation of the degree of circular polarization using Equation (3.1) is repeated for all polarization configurations and carriers, and the results are summarized in Table 3.1.

Table 3.1: The degree of circular polarization, determined with Equation (3.1), for the electron and hole SF lines in anti-Stokes (AS) and Stokes (S) spectral ranges.

exc. pol.	Faraday geometry σ^+		σ^-	
	AS	S	AS	S
e	−0.70	0.03	0.06	−0.60
h	0.40	−0.65	−0.50	0.40

The behavior of the measured polarization degrees can be summarized as follows: For both carriers, the sign of the polarization degree reverses when switching from Stokes to anti-Stokes side or when changing between σ^+ and σ^- excitation. Furthermore, the difference in magnitude of the polarization degree in Stokes and anti-Stokes side is inverted depending on the excitation polarization. This effect is more pronounced for the electron SF, where only a few percent polarization degree is observed on Stokes side for σ^+ excitation and on anti-Stokes side for σ^- excitation. Finally, the entire sign behavior of the polarization degrees is inverted between electrons and holes. This observation might be an indication that the sign of the g-factor is essential for understanding the behavior of the polarization degrees. To gain insight into the described polarization dependence of the $MAPbI_3$ SFRS spectra, a simplified model is presented in the following.

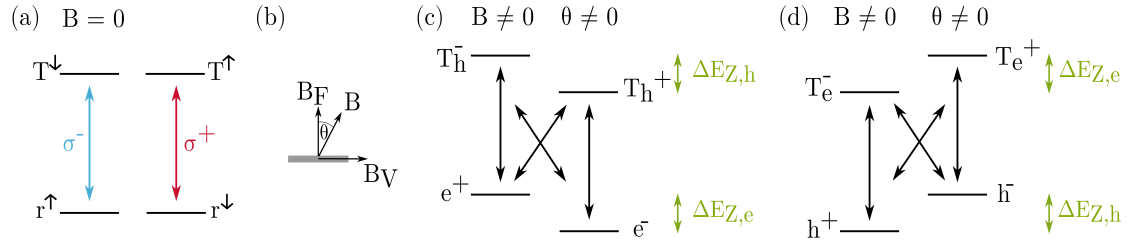

Figure 3.3: Optical selection rules for the SFRS process involving a resident carrier. (a) Degenerate ground and excited states of the resident carriers $r^{\uparrow\downarrow}$ and the intermediate scattering state $T^{\uparrow\downarrow}$, respectively. (b) Experimental geometry, where the magnetic field is tilted by an angle θ from pure Faraday geometry B_{F}. (c) and (d) Splitting of the resident carrier and trion states by the Zeeman energy $\Delta E_{\mathrm{Z,(e,h)}}$ for $g_{\mathrm{e}} > 0$, $g_{\mathrm{h}} < 0$. Arrows indicate the optical transitions for the exciation and emission: (c) for the resident electron and (d) for the resident hole.

As characterized by the carrier lifetimes in Section 3.1, the observed SFs originate from resident carriers that interact with a photogenerated exciton, which is further explained in Section 1.6.3.

Therefore, the system under study can be described by a four-level scheme as shown in Figure 3.3(a) with two spin configurations of the resident carrier states $|r^{\uparrow\downarrow}\rangle$ (where r is either electron or hole) and two spin configurations of the excited three-particle state $|T^{\uparrow\downarrow}\rangle$, which can be excited by circular polarizations $\sigma^{\pm}$. As these optical transitions are decoupled from each other, the emitted light retains the same polarization as the excitation. When an external longitudinal magnetic field is applied in pure Faraday geometry, the energy levels of both the resident carrier and the three-particle state split according to the Zeeman energy ΔE_{Z}, while the purely circularly polarized optical transitions remain unaffected. The Hamiltonian, in this case, reads as

$$\hat{H} = -\frac{g_{\mathrm{r}}\mu_B B}{2}|r^{\downarrow}\rangle\langle r^{\downarrow}| + \frac{g_{\mathrm{r}}\mu_B B}{2}|r^{\uparrow}\rangle\langle r^{\uparrow}|. \tag{3.2}$$

As discussed in Section 1.6.3, in pure Faraday geometry, no SF signal can be observed. However, the experimental geometry slightly deviates from pure Faraday geometry, enabling the observation of a SF signal. This results in a small tilt of the magnetic field by an angle θ, as schematically illustrated in Figure 3.3(b). The optical selection rules for the SFRS process in a slightly tilted magnetic field for the resident electron with $g_{\mathrm{e}} > 0$ and for the resident hole with $g_{\mathrm{h}} < 0$, are presented in Figure 3.3(c) and (d), respectively. The magnetic field splits the degenerate resident carrier levels by the Zeeman energy $\Delta E_{\mathrm{Z,r}}$, where r represents either an electron or a hole. Similarly, the three-particle states are split by the Zeeman energy $\Delta E_{\mathrm{Z,T}}$, which is determined by either the hole or electron. Furthermore, the pure spin states are mixed, which is described by the Hamiltonian, including the nonzero tilt angle of the magnetic field

$$\begin{aligned}\hat{H} = &-\frac{g_{\mathrm{r}}\mu_B B}{2}\cos(\theta)|r^{\downarrow}\rangle\langle r^{\downarrow}| + \frac{g_{\mathrm{r}}\mu_B B}{2}\cos(\theta)|r^{\uparrow}\rangle\langle r^{\uparrow}| + \frac{g_{\mathrm{r}}\mu_B B}{2}\sin(\theta)|r^{\uparrow}\rangle\langle r^{\downarrow}| + c.c.\\ &-\frac{g_{\mathrm{T}}\mu_B B}{2}\cos(\theta)|T^{\downarrow}\rangle\langle T^{\downarrow}| + \frac{g_{\mathrm{T}}\mu_B B}{2}\cos(\theta)|T^{\uparrow}\rangle\langle T^{\uparrow}| + \frac{g_{\mathrm{T}}\mu_B B}{2}\sin(\theta)|T^{\uparrow}\rangle\langle T^{\downarrow}| + c.c..\end{aligned} \tag{3.3}$$

For simplicity, an anisotropy of the g-factors is not considered. The system becomes diagonal in the base given by mixtures of the pure ground and excited states

$$\begin{aligned}|r^{+}\rangle &= |r^{\uparrow}\rangle - \frac{\sin\theta}{\cos\theta+1}|r^{\downarrow}\rangle\\ |r^{-}\rangle &= \frac{\sin\theta}{\cos\theta+1}|r^{\uparrow}\rangle + |r^{\downarrow}\rangle\\ |T^{+}\rangle &= |T^{\uparrow}\rangle - \frac{\sin\theta}{\cos\theta+1}|T^{\downarrow}\rangle\\ |T^{-}\rangle &= \frac{\sin\theta}{\cos\theta+1}|T^{\uparrow}\rangle + |T^{\downarrow}\rangle.\end{aligned} \tag{3.4}$$

To analyze the effect of polarization selection rules in this mixed base, the dipole operator is transformed accordingly. In unperturbed base, the σ^{+} and σ^{-} components of the dipole operator are given by

$$\begin{aligned}\hat{\mu}^{+} &= \mu(|r^{\downarrow}\rangle\langle T^{\uparrow}| + c.c.)\\ \hat{\mu}^{-} &= \mu(|r^{\uparrow}\rangle\langle T^{\downarrow}| + c.c.),\end{aligned} \tag{3.5}$$

where the magnitude μ of both transitions is assumed to be equal. The dipole operator components in the mixed base read as

$$\begin{aligned}\hat{\mu}_D^{+} &= \mu\left(-\frac{\sin\theta}{2}|r^{+}\rangle\langle T^{+}| - \frac{\sin^2\theta}{2(\cos\theta+1)}|r^{-}\rangle\langle T^{+}| + \frac{\cos\theta+1}{2}|r^{+}\rangle\langle T^{-}| + \frac{\sin\theta}{2}|r^{-}\rangle\langle T^{-}| + c.c.\right)\\ \hat{\mu}_D^{-} &= \mu\left(-\frac{\sin\theta}{2}|r^{+}\rangle\langle T^{+}| + \frac{\cos\theta+1}{2}|r^{-}\rangle\langle T^{+}| - \frac{\sin^2(\theta)}{2(\cos(\theta)+1)}|r^{+}\rangle\langle T^{-}| + \frac{\sin(\theta)}{2}|r^{-}\rangle\langle T^{-}| + c.c.\right).\end{aligned} \tag{3.6}$$

Here, it can be seen that in the mixed base, both σ^+ and σ^- mediate between all mixed ground and excited states, as indicated by the arrows in Figures 3.3(c) and (d). Furthermore, for a given angle θ, where $0 < \theta < \pi/2$, the magnitude of the transition dipole elements can strongly differ. For example, the dipole moments of the transitions $|r^+\rangle \rightarrow |T^-\rangle$ and $|r^-\rangle \rightarrow |T^+\rangle$ have, in general, a different magnitude. This result represents a first hint that can explain the sign inversion of the polarization degree for electron and hole in the Stokes/anti-Stokes SFRS processes. As the electron and hole g-factors have opposite signs, the lowest and highest ground states are reversed, as shown in Figures 3.3(c) and (d). Consequently, different transition cascades are involved in the SFRS process. For example, for the Stokes process of the electron, the cascade $|e^-\rangle \rightarrow |T^+\rangle \rightarrow |e^+\rangle$ is relevant while for the hole the cascade $|h^+\rangle \rightarrow |T^-\rangle \rightarrow |h^-\rangle$ contributes. Since the dipole moments of the transitions differ, as can be seen in Equation (3.5), the SF magnitudes in co- and cross-polarized polarization configuration can be inverted for electron and hole.

To quantify this qualitative discussion, the Kramers-Heisenberg equation (Equation (1.18)) is applied in the following to calculate the magnitudes of the SF peaks

$$A \propto \sum_{|n\rangle} \left| \langle f|\hat{\mu}|n\rangle\langle n|\hat{\mu}|i\rangle \right|^2 . \tag{3.7}$$

In the considered special case, the intermediate states $|n\rangle$ are given by the three-particle states in mixed base $|T^\pm\rangle$, whereas the initial and final states are given by the mixed resident states $|r^\pm\rangle$. As mentioned above, whether $|r^+\rangle$ or $|r^-\rangle$ represents the initial or final state for the SFRS process on Stokes or anti-Stokes side depends on the sign of the g-factor. For the electron, the Stokes signal is calculated as

$$S_{\mathrm{e,\,S}} \propto \left\| e^+\rangle\langle T^+|\hat{\mu}^\pm|T^+\rangle\langle e^-\right\|^2 + \left\| e^+\rangle\langle T^-|\hat{\mu}^\pm|T^-\rangle\langle e^-\right\|^2 . \tag{3.8}$$

Here, depending on the considered polarization configuration, the terms for μ^+ and μ^- from Equation (3.6) are inserted. In the same way, the anti-Stokes signal is calculated using

$$S_{\mathrm{e,\,AS}} \propto \left\| e^-\rangle\langle T^-|\hat{\mu}^\pm|T^-\rangle\langle e^+\right\|^2 + \left\| e^-\rangle\langle T^+|\hat{\mu}^\pm|T^+\rangle\langle e^+\right\|^2 . \tag{3.9}$$

For the hole, the amplitudes correspondingly read as

$$\begin{aligned} S_{\mathrm{h,\,S}} &\propto \left\| h^-\rangle\langle T^-|\hat{\mu}^\pm|T^-\rangle\langle h^+\right\|^2 + \left\| h^-\rangle\langle T^+|\hat{\mu}^\pm|T^+\rangle\langle h^+\right\|^2 , \\ S_{\mathrm{h,\,AS}} &\propto \left\| h^+\rangle\langle T^+|\hat{\mu}^\pm|T^+\rangle\langle h^+\right\|^2 + \left\| h^+\rangle\langle T^-|\hat{\mu}^\pm|T^-\rangle\langle h^+\right\|^2 . \end{aligned} \tag{3.10}$$

As a final step, the calculated signals are used to evaluate the polarization degrees as defined in Equation (3.1). Since the resulting expressions for the polarization degrees are quite complex, a graphical representation of the results is presented in Figure 3.4. Here, the polarization degrees for the electron on Stokes and anti-Stokes side as a function of the tilt angle θ are presented in Figures 3.4(a) and (b), with σ^+ excitation in (a) and σ^- excitation in (b). For the polarization degree of the hole, σ^+ excitation is shown in (c) and σ^- excitation in (d). Note that the curves are undefined for $\theta = 0$ (pure Faraday geometry, where all SF signals are zero), which is excluded here.

The resulting qualitative behavior of the polarization degree successfully explains all key features of the experimental results: For a given angle θ, a sign inversion of the polarization degree occurs when switching from Stokes to anti-Stokes side, from σ^+ to σ^- excitation, and from electron to hole due to the opposite sign of their g-factors. Furthermore, the model captures the asymmetry in the polarization degree, where the positive values are smaller than the negative ones. However,

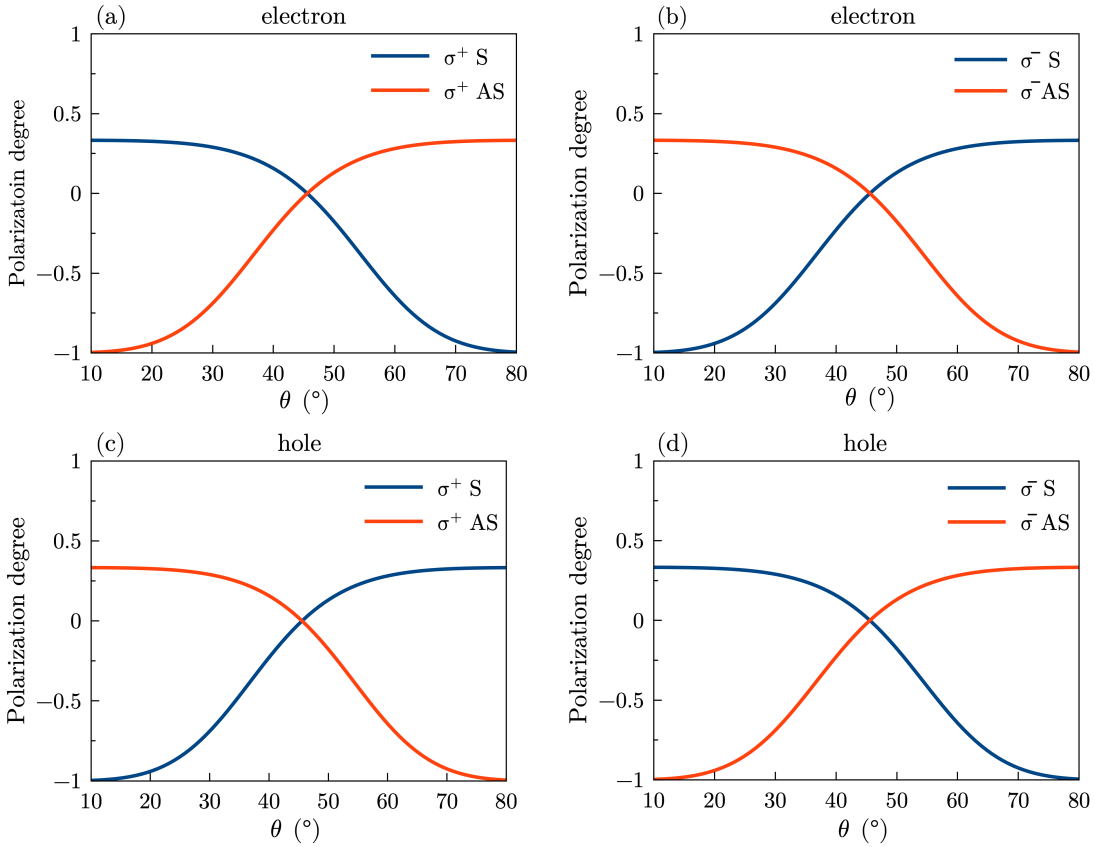

Figure 3.4: Calculated polarization degrees for Stokes (S) side (blue lines) and anti-Stokes (AS) side (red lines) according to Equation (3.1). (a) and (b) show the polarization degrees for the resident electron, while (c) and (d) correspond to the resident hole. σ^+ excitation for (a) und (c), and σ^- excitation in (b) und (d).

the simplified model cannot fully reproduce the measured polarization degree for small angles, as summarized in Table 3.1, nor does it account for the fact that the values for electrons and holes are not identical, highlighting the limitations of the model.

Nevertheless, the successful reproduction of the key experimental results with the presented model confirms that the observed polarization dependence of the SFRS spectra arises directly from the combination of a non-perfect Faraday geometry and the four-level excitation scheme involving resident carriers in the ground states and excited three-particle states. This result is remarkable, as it provides additional evidence that the observed SFRS signals indeed originate from resident carriers in the lead halide perovskite crystal. Furthermore, the inverted polarization behavior of electrons and holes further supports the conclusion that the sign of the hole g-factor is negative, as already measured in Reference [143] using DNP. As the identification of the g-factor sign is generally a non-trivial task, the systematic polarization analysis presented here offers a powerful approach for measuring the sign of g-factors in so far unexplored materials.

Higher order spin-flip processes in Faraday geometry

As the magnetic field increases, additional SF lines with slightly different g-factors, which were not resolved at lower magnetic fields, appear in the SFRS spectrum at $B_\mathrm{F} = 6\,\mathrm{T}$, as shown in

Figure 3.5(a). According to Figure 3.2(a), the cross-circularly polarized configuration $\sigma^+\sigma^-$ is chosen to observe strong electron and hole SFs. Both the anti-Stokes and part of the Stokes spectral range are presented to display the various SF lines, indicated by vertical arrows, which are preferentially observed on either the Stokes or anti-Stokes side. On anti-Stokes side, six SF lines are observed, labeled as h, e+h, e′, e, e-h, and 2e, while on Stokes side, two additional lines can be identified, labeled as h′ and 2h. The labels of the SFs are assigned based on the SFRS processes involving the corresponding carriers, including single, combined, or double carrier SFs. Note that part of the anti-Stokes spectrum for the e-h and 2e SFs is multiplied by a factor of 30 to enhance their visibility. The Raman shift for the various SFs lines at different magnetic fields is depicted in Figure 3.5(b), along with the corresponding g-factors.

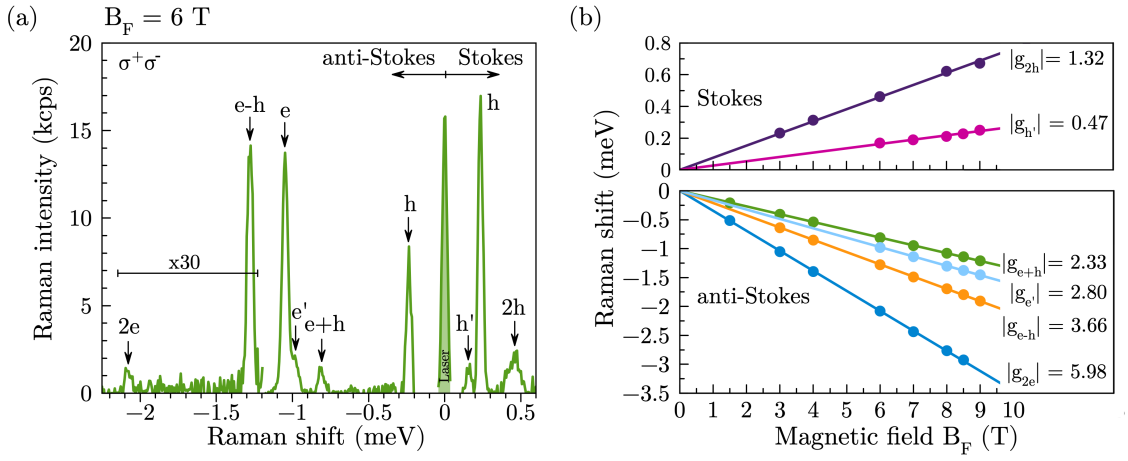

Figure 3.5: SFRS spectra of $MAPbI_3$ in Faraday geometry at $B_F = 6$ T in cross-circular polarization $\sigma^+\sigma^-$ with an excitation power density of $P = 0.6$ W/cm^2. Multiple SFs are indicated by vertical arrows, which shift linearly with the magnetic field in (b). To enhance the visibility of the e-h and 2e SFs lines, this part of the spectrum is multiplied by a factor of 30.

On anti-Stokes side, the strongest SF line is the electron SF with a Raman shift of $E_e = -1.05$ meV. The electron SF line is accompanied by two equidistant lines on the left and right-hand sides: one at -1.27 meV (labeled as $E_{e\text{-}h}$) with a g-factor of $|g_{e\text{-}h}| = 3.66$ and the other on the opposite side of the electron SF line at a Raman shift of $E_{e+h} = -0.81$ meV with a g-factor of $|g_{e+h}| = 2.33$. The difference in Raman shift matches that of the hole with $E_h = -0.24$ meV, leading us to conclude that these lines arise from a combined SF processes, where both an electron and a hole SF occur simultaneously. In addition, the SF line at $E_{2e} = -2.09$ meV, with a corresponding g-factor of $|g_{2e}| = 5.98$, is twice that of the electron, and is consistently attributed to an SFRS process involving the SFs of two electrons. The observation of both combined and double SF processes is extremely rare, as their SF intensity is significantly reduced due to the lower efficiency of the higher-order process involving an additional carrier [31]. To the best of our knowledge, a combined SF of a resident electron and hole has been found in 2D perovskite $(PEA)_2PbI_4$ [15] but no double SF processes involving two electrons and two holes have been reported in lead halide perovskites so far. Interestingly, on the Stokes side, we can not only identify the hole SF line, but also observe the SF of two holes ($E_{2h} = 0.47$ meV with $|g_{2h}| = 1.32$), which we were unable to detect on the anti-Stokes side. Additionally, the SFRS spectrum reveals shoulders on the lower-energy side for the hole on Stokes side at $E_{h'} = 0.17$ meV and for the electron on anti-Stokes side at -0.98 meV, which we denote as h′ and e′, respectively. We attribute these two lines, with $|g_{h'}| = 0.47$ and $|g_{e'}| = 2.80$, to a structural domain, where the orthorhombic axis is tilted relative to the sample's out-of-plane axis, as these g-factor values do not not match any

combination of g_e and g_h. The ratio of the SF intensities for e and e′ is roughly 6:1, while it is 10:1 for h and h′. This indicates that the sample is not composed of a single domain, rather, most domains are oriented in a specific direction, with only a small fraction oriented differently. A more detailed investigation of the domain orientation is presented in Section 3.2.3.

3.2.2 Voigt geometry

To determine the in-plane components of the electron and hole g-factors, SFRS measurements are performed in Voigt geometry ($\theta = 90°$). In Faraday geometry, a strong polarization dependence of the SF intensities for both electron and hole is observed in Figures 3.2(a) and (b). Accordingly, we begin our study of SFRS in Voigt geometry by analyzing the effects of linear polarizations on the SF intensities at a magnetic field of $B_V = 8$ T, as shown in Figures 3.6(a) and (b). The polarization configuration is represented by two letters, where the first one indicates the excitation polarization, and the second letter denotes the detection polarization. Linear polarizations, either horizontal (H) or vertical (V), are used to define the polarization configurations.

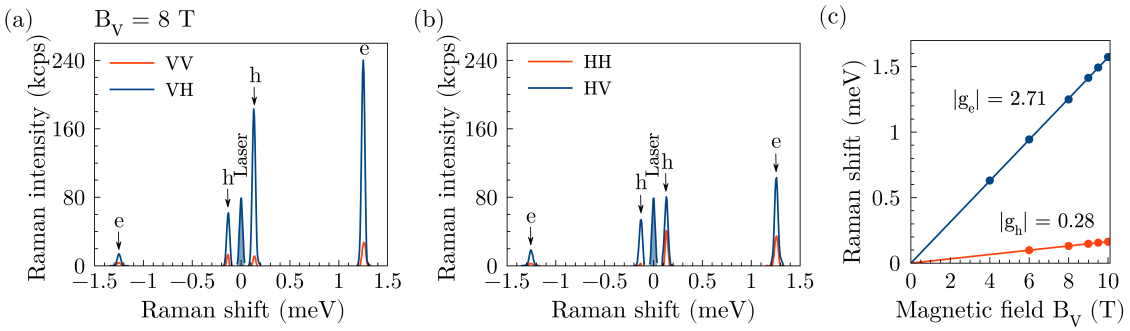

Figure 3.6: Polarization dependence of the electron and hole SFs in Voigt geometry at $B_V = 8$ T, excited at the exciton resonance with $E_{exc} = 1.633$ eV and a power density of $P = 0.6$ W/cm^2. (a) corresponds to vertical (V) excitation, while (b) corresponds to horizontal (H) excitation. Red represents co-linear polarization, and blue represents cross-linear polarization. (c) Magnetic field dependence of the electron and hole Raman shifts, along with the determined g-factors.

Two distinct SFs in the SFRS spectra, shown in Figures 3.6(a) and (b), are identified at Raman shifts of $|E_h| = 0.13$ meV and $|E_e| = 1.25$ meV, both shifting linearly with the magnetic field (see Figure 3.6(c)). Thus, the g-factors are calculated to be $|g_h| = 0.28$ and $|g_e| = 2.71$. The sign of both g-factors are discussed in Section 3.2.1, leading to $g_h < 0$ and $g_e > 0$. A comparison of the g-factor values with those reported in Reference [143] reveals that the g-factor of the hole, $g_h = -0.33$, is in good agreement, while the g-factor for the electron $g_e = 2.56$, shows a slight deviation from our experimental results. Additionally, the results of the transversal g-factor values for the electron and hole are consistent with those reported for polycrystalline $MAPbI_3$ [166].

Polarization dependence

In Voigt geometry, the polarization dependence observed in Figures 3.6(a) and (b) demonstrates that for both vertical (V) and horizontal (H) excitation, cross-polarization is more favorable, as indicated by higher SF intensities for both electrons and holes. Notably, the opposite behavior between electron and hole SFs, as identified in Figures 3.2(a) and (b) for circular polarization in Faraday geometry, is not evident for linear polarizations in Voigt geometry. The degree of linear polarization is calculated by Equation (3.1) and summarized in Table 3.2.

Table 3.2: The degree of polarization, determined with Equation (3.1), for the electron and hole SF lines in the anti-Stokes (AS) and Stokes (S) spectral ranges.

	Voigt geometry			
exc. pol.	H		V	
	AS	S	AS	S
e	−0.75	−0.50	−0.60	−0.80
h	−0.90	−0.35	−0.65	−0.90

The degree of linear polarization ranges from −0.35 to −0.90, indicating a stronger SF signal for cross-polarization. This preferential observation of the SF signal for cross-polarization is consistent with theoretical predictions for the SFRS process involving resident carriers in perovskite semiconductors [37] and can be explained by the simple model introduced in Section 3.2.1. Consequently, in Voigt geometry, we set the tilt angle $\theta = 90°$. In the experiment, vertical and horizontal linear polarization configurations are used for both excitation and detection, requiring the determination of the dipole operator components in the mixed state basis for horizontal (H) and vertical (V) polarization given by

$$\begin{aligned} \hat{\mu}_H &\propto \hat{\mu}_D^+ + \hat{\mu}_D^- \propto -|r^+\rangle\langle T^+| + |r^-\rangle\langle T^-|, \\ \hat{\mu}_V &\propto \hat{\mu}_D^- - \hat{\mu}_D^+ \propto |r^-\rangle\langle T^+| - |r^+\rangle\langle T^-|, \end{aligned} \tag{3.11}$$

mediating the optical transitions shown in Figure 3.7.

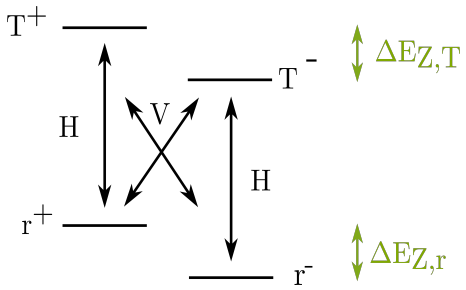

Figure 3.7: Optical selection rules for the SFRS process involving a resident carrier in the Zeeman split ground state $|r^{\pm}\rangle$ and three-particle state $|T^{\pm}\rangle$ in Voigt geometry. Arrows indicate the optical transitions for horizontally (H) and vertically (V) polarized excitation and emission.

As shown in Figure 3.7, the optical transitions of the SFRS process involving a resident carrier are mediated by horizontal and vertical linear polarizations. According to Equation (3.11), horizontally polarized light induces the transitions $r^+ \rightarrow T^+$ and $r^- \rightarrow T^-$, while vertically polarized light induces the transitions $r^+ \rightarrow T^-$ and $r^- \rightarrow T^+$. Therefore, horizontal and vertical polarization cannot mediate between all mixed ground and excited states, as indicated by the arrows in Figure 3.7. As a result, in ideal Voigt geometry, linear co-polarization does not generate any signal in the SFRS process. Consequently, only the linear cross-polarized configurations can be observed. This argumentation is consistent with the experimental observation in Figure 3.6 where in all polarization configurations on both Stokes and anti-Stokes side, a significantly stronger signal is observed in cross-polarization. The non-zero signal observed in co-polarization might be an indication of a non-perfect Voigt geometry.

The Voigt geometry is favorable for measuring SFRS, as the perpendicular magnetic field mixes the spin states, thereby enhancing the efficiency of the SF process. Comparing the SFRS spectra

in Faraday (see Figure 3.5(a)) and Voigt geometry (Figure 3.8(b)), for instance, the hole on Stokes side reveals that the SF intensity in Voigt geometry is approximately three times higher than in Faraday geometry.

Higher order spin flip processes in Voigt geometry

As the SF intensities are the highest for cross-linear polarization (VH), this polarization configuration is chosen for the SFRS spectra shown in Figures 3.8(a) and (b). Figures 3.8(a) and (b) present the complete SFRS spectrum for cross-linear polarization (VH) at magnetic fields of $B_V = 6$ T (a) and $B_V = 9$ T (b), respectively.

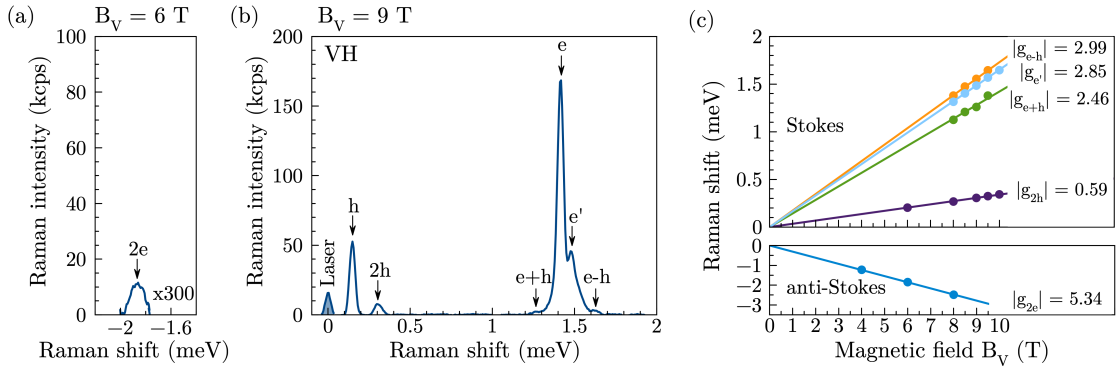

Figure 3.8: SFRS spectra of $MAPbI_3$ in Voigt geometry at $B_V = 6$ T (a) and $B_V = 9$ T (b) in cross-linear polarization VH with $P = 0.6$ W/cm^2. Multiple SFs are indicated by vertical arrows, which shift linearly with the magnetic field in (c). To enhance the visibility of the SF lines, the double electron SF in (a) is multiplied with a factor of 300.

Along with the electron and hole SFs identified in Figure 3.6, several additional SF lines with lower intensities can be observed in Figure 3.8(b). Close to the electron SF, the combined SF of an electron and hole can be observed at $E_{e+h} = 1.26$ meV ($g_{e+h} = 2.46$) and $E_{e-h} = 1.57$ meV ($g_{e-h} = 2.99$). The SF line at $E_{2h} = 0.31$ meV can be assigned to the double hole SF with a g-factor of $g_{2h} = -0.59$. On Stokes side, the SF of two electrons is not observable and is therefore evaluated from anti-Stokes side, as shown for $B_V = 6$ T in Figure 3.8(a), yielding $g_{2e} = 5.34$. Additionally, at this high magnetic field of $B_V = 9$ T, the electron SF from the other structural domain becomes visible at $E_{e'} = 1.64$ meV, which is also observed in Faraday geometry (see Figure 3.5(a)). In contrast to Faraday geometry, where the e′ SF has a smaller Raman shift compared to the electron, in Voigt geometry, the Raman shift is larger, indicating an anisotropy of the g-factor.

3.2.3 g-factor anisotropy

Table 3.3 summarizes the g-factors in Faraday and Voigt geometries, determined by SFRS, along with the g-factors measured with TRKR in Reference [143]. Note that $MAPbI_3$ exhibits a complex g-factor anisotropy, which is not aligned with the main axes of the sample. As a result, the g-factor values provided by TRKR, measured with a vector magnet, correspond to the minimal and maximal g-factor values, g_{min} and g_{max}.

The g-factor values presented in Table 3.3 clearly demonstrate that the g-factors for both the electron and the hole differ between Faraday and Voigt geometry, leading to a distinct g-factor

Table 3.3: Overview of the g-factors in Faraday and Voigt geometry for bulk $MAPbI_3$ single crystals measured by SFRS and TRKR. [143].

	SFRS		TRKR [143]	
g-factor	Faraday $\theta = 0^\circ$	Voigt $\theta = 90^\circ$	g_{max}	g_{min}
e	3.00	2.71	2.98	2.46
h	−0.66	−0.28	−0.71	−0.28
2e	5.98	5.34		
2h	−1.32	−0.59		
e+h	2.33	2.46		
e-h	3.66	2.99		

anisotropy for both carriers. This anisotropy arises from the structural anisotropy of the material as a consequence of the orthorhombic crystal phase that $MAPbI_3$ exhibits at temperatures below 160 K [167]. From the g-factor anisotropy, we aim to determine the orientation of the g-factor tensor for both structural domains. Therefore, the g-factor anisotropy, presented in Figure 3.9, is complemented by SFRS measurements conducted in $\theta = 15^\circ$ steps relative to the magnetic field direction, where θ denotes the tilt angle as defined in Figure 3.3(b).

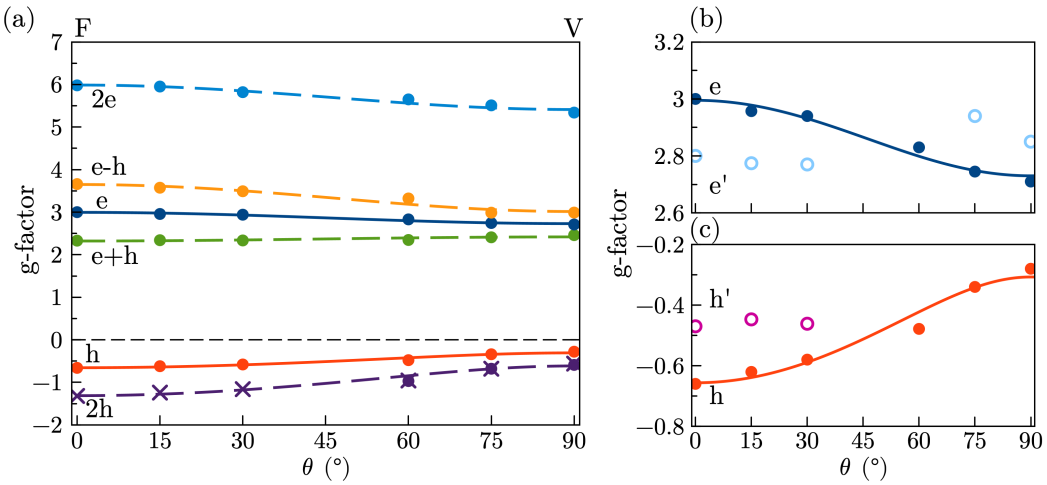

Figure 3.9: (a)-(c) g-factor anisotropy for different carriers in $MAPbI_3$ between Faraday ($\theta = 0^\circ$) and Voigt ($\theta = 90^\circ$) geometry. Crosses represent calculated g-factor values and lines are fits with Equation (3.12). Solid lines for single carriers and dashed lines for combined/double carriers in (a). (b) and (c) g-factor anisotropies of the electron and hole with fits based on Equation (3.12).

Both electron and hole g-factors exhibit an anisotropy: g_e varies from +3.00 ($\theta = 0^\circ$) to +2.71 ($\theta = 90^\circ$), while g_h ranges between −0.66 ($\theta = 0^\circ$) and −0.28 ($\theta = 90^\circ$). The angular dependence of the g-factor in Figure 3.9(a) is modeled by fitting the experimental data to [62]

$$g(\theta) = \sqrt{(g_c \cos\theta)^2 + (g_{(a,b)} \sin\theta)^2}, \tag{3.12}$$

where g_c denotes the g-factor in Faraday, $g_{(a,b)}$ corresponds to the g-factor in Voigt geometry, and θ is the tilt angle. The relative g-factor anisotropy Δg is quantified by [62]

$$\Delta g = \frac{g_F - g_V}{g_F + g_V}, \tag{3.13}$$

where g_F and g_V denote the g-factors measured in Faraday and Voigt geometries, respectively. Applying Equation (3.13), the hole g-factor anisotropy reaches 40%, while the electron g-factor anisotropy is significantly smaller with 5%, consistent with TRKR measurements reported in Reference [143]. The anisotropies for the double electron and hole SFs are similar in relative numbers to those of the single electron and hole SFs, with values of 40% for holes and 6% for electrons. Reference [125] reports that the anisotropies g_e and g_h in lead halide perovskite crystals nearly compensate each other, resulting in a nearly constant g-factor for the bright exciton. The bright exciton g-factor in lead halide perovskites is defined by the sum of the electron and hole g-factors $g_X = g_e + g_h$, yielding $g_{e,F} + g_{h,F} = 2.34$ and $g_{e,V} + g_{h,V} = 2.43$. The measured value of $g_X = +2.30$ from magneto-transmission (Figure 3.1(c)) demonstrates a good agreement, confirming the expected isotropy for g_X.

In Figures 3.9(b) and (c), the g-factor anisotropies of e′ and h′ (open dots) are compared to those of the electron and hole (closed dots). While the anisotropy of the electron and hole g-factors follows a distinct trend, e′ and h′ exhibit a smoother but opposite behavior. This behavior can also be observed by comparing the SFRS spectra in Faraday (Figure 3.5(a)) and Voigt geometry (Figure 3.8(b)): in Faraday geometry, the Raman shift $|E_{e'}|$ is smaller than $|E_e|$, while in Voigt geometry, it is larger. The different g-factor anisotropies, along with the fact that their g-factor do not match any combination of the electron and hole g-factors provides further evidence that e′ and h′ originate from structural domains with tilted orientations. As the g-factor anisotropy for e′ and h′ is small, we propose that the crystallographic out-of-plane c-axes lies nearly in the plane, with the magnetic field being rotated between the a- and b-axes. However, as our experiments are limited to measurements of the g-factor anisotropy to the horizontal plane, we cannot determine any possible tilting in the vertical direction. Further investigations using a vector magnet would be required to determine the precise orientation of the structural domain. Nevertheless, the intensities between e to e′ and h to h′ are nearly an order of magnitude larger, indicating that the sample primarily consists of a single domain in which the crystallographic axes align with the laboratory frame. This alignment enables to model the g-factor anisotropies for electron and hole with Equation (3.12), as shown by the solid lines in Figures 3.9(b) and (c).

3.3 Conclusions

This chapter presented the application of SFRS to resident carriers in a bulk $MAPbI_3$ single crystal. For this sample, strongly polarization-dependent SFRS spectra were observed in Faraday and Voigt geometry. To gain insight into the polarization dependence, a simplified model was introduced that describes the system as a four-level scheme with ground resident carrier states and excited three-particle states. The simplified model successfully explains the key features of the experimental results, providing additional proof that the observed SFRS signal originates from resident carriers. Furthermore, this model offers a valuable approach for determining the sign of the g-factor through systematic polarization analysis.

In $MAPbI_3$, we discovered not only single carrier SFs but also rare double SFs involving two resident electrons or holes. The observation of SF lines with different anisotropies indicates that the sample consists of two structural domain orientations. The integral intensities of the electron and hole SF lines from one domain are approximately an order of magnitude stronger than those from the other domain, allowing us to conclude that the studied $MAPbI_3$ single crystal can be considered nearly single-domain. To gain full insight into the domain orientation, detailed studies of the g-factor anisotropy using a vector magnet that can differentiate between the two in-plane axes of the sample are required. In conclusion, the results presented in this chapter demonstrate that SFRS is a powerful tool for probing the domain structure and their orientations in lead halide perovskites.

Spin-flip Raman spectroscopy of 2D lead halide perovskites

4

The experiments presented in this chapter investigate the optical and spin properties of resident carriers in Ruddlesdon-Popper (RP)-type two-dimensional lead halide perovskites $(PEA)_2(MA, FA)_{n-1}Pb_nX_{3n+1}$, with varying inorganic layer thickness n and halides X = Br, I. First, for $(PEA)_2PbI_4$ with $n = 1$, a characterization of the optical properties (Section 4.1.1) and the results of spin-flip Raman scattering (SFRS) (Section 4.1.2) are presented in detail. Section 4.1.3 reveals the exchange interaction between resident electrons and nuclei. By applying the technique of SFRS to 2D perovskites with different inorganic layer thicknesses, the electron and hole g-factors are determined separately for the bromide (Section 4.2.1) and iodine series (Section 4.2.2). These results are then combined in Section 4.2.3 to provide insights into the g-factor dispersion across a wide energy range. For 2D perovskites, the dependence of the electron and hole g-factors on the band gap energy is found to deviate from the universal dependence observed in bulk perovskites [62], indicating that the quantum confinement in one direction modifies the g-factor, as the mixing of electronic bands in 2D perovskites differs significantly from that in bulk.

The results presented in this chapter are previously published in:

> C. Harkort, D. Kudlacik, N. E. Kopteva, D. R. Yakovlev, M. Karzel, E. Kirstein, O. Hordichuk, M. V. Kovalenko, and M. Bayer, "Spin-flip Raman Scattering on Electrons and Holes in Two-Dimensional $(PEA)_2PbI_4$ Perovskites", Small **19**, 2300988 (2023)
> DOI: 10.1002/smll.202300988,

4.1 Optical and spin properties of $(PEA)_2PbI_4$

4.1.1 Optical properties

As a first step of our study, we characterize the optical properties of $(PEA)_2PbI_4$ with $n = 1$ at a temperature of $T = 1.6\,K$. The reflectivity spectrum presented in Figure 4.1(a) exhibits a pronounced exciton resonance with a minimum at 2.341 eV, which aligns with the maximum observed at 2.343 eV in the photoluminescence (PL) spectrum. In a longitudinal magnetic field (Faraday geometry) of $B_F = 7\,T$, the reflectivity spectra measured for both circular detection polarizations ($\sigma^{\pm}$) exhibit a Zeeman splitting of the exciton resonance, corresponding to a splitting energy of $E_{Z,X} = 0.63\,meV$ (see Figure 4.1(b)). The magnetic field dependent Zeeman splitting of the exciton resonance is shown in Figure 4.1(c). From a linear fit, as shown by the red dashed line, we extract the exciton g-factor $g_{X,C} = +1.6$. Note that in this experiment, the sign of the g-factor can be determined. A positive g-factor value indicates that the reflectivity minimum shifts to higher energies when detected with σ^+ polarized light, relative to detection with σ^- polarized light.

To identify the different contributions to the radiate recombination channels in the PL spectra based on their characteristic lifetimes, the time-resolved PL dynamics at the PL maximum are analyzed. In Reference [72], PL dynamics were measured for $(PEA)_2PbI_4$ with $n = 1$ from the

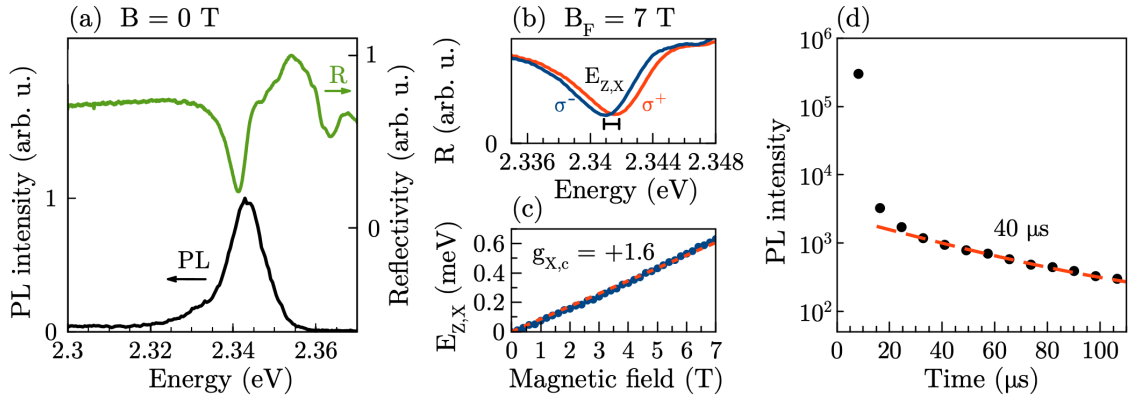

Figure 4.1: (a) Normalized PL (black) and reflectivity (green) spectrum of $(PEA)_2PbI_4$ with $n = 1$ in zero magnetic field. (b) Splitting of the exciton resonance in reflectivity by the Zeeman energy $E_{Z,X}$ between σ^+ and σ^- polarized detection in a magnetic field of $B_F = 7$ T. (c) Magnetic field dependence of the Zeeman splitting (blue dots) and fit to a linear function (red dashed line). (d) Decay of the PL (black dots) measured at the PL maximum of 2.343 eV with a pulsed excitation of $E_{exc} = 3.493$ eV and power density of $P = 3$ W/cm^2. The fit to a single exponential (red line) allows to extract the decay time of the long-lived component.

same sample batch, revealing a fast component of 20 ps, which is attributed to the lifetime of the bright exciton with a large oscillator strength in 2D perovskites. The long PL dynamics, extending up to 110 µs, are shown in Figure 4.1(d). Interestingly, we observe a long decay time of 40 µs, which exceeds the exciton recombination times for this material as reported in Reference [72]. This indicates the presence of long-lived, spatially separated carriers within the sample. The existence of resident carriers in lead halide perovskites has been reported for various materials, such as $CsPbBr_3$ [142], $FA_{0.9}Cs_{0.1}PbI_{2.8}Br_{0.2}$ [18], and $MAPbI_3$ [168] crystals. These resident carriers can be photogenerated electrons and holes that are localized at spatially different regions of the perovskite crystal before recombination, resulting in their extended lifetime. In the SFRS spectra presented in Section 4.1.2, the spin-flips (SFs) originate from the interaction between resident carriers and the photogenerated exciton. This interaction enables us to observe the Zeeman splitting through changes in the exciton emission energy.

4.1.2 Carrier g-factors measured by spin-flip Raman spectroscopy

Next, we aim to determine the optimal conditions for measuring the SFRS spectrum of $(PEA)_2PbI_4$ with $n = 1$, considering parameters such as excitation energy, magnetic field geometry, temperature, and polarization. As an initial step, we set the excitation energy to match the exciton resonance and subsequently adjust the experimental parameters to maximize the intensity of the SFs.

As discussed in Section 1.6.3, measuring SFRS in Voigt geometry is favorable, as the carrier out-of-plane spin components are mixed, thereby enhancing the probability of SF transitions. The experimental definition of Voigt geometry is illustrated in Figure 4.2(a), where the magnetic field **B** is aligned along the in-plane (a, b) axes of the sample, and the light's wave vector **k** is oriented along the out-of-plan c-axis of the sample. The SFRS spectrum measured in Voigt geometry is presented in Figure 4.2(b), recorded at a magnetic field of $B_V = 10\,T$ and a temperature of $T = 1.6\,K$. Two peaks, corresponding to SFs lines, are visible in the SFRS spectrum and marked by vertical arrows. The intensity of the SF line at $-1.45\,meV$ at different excitation energies is shown in the resonance profile in Figure 4.2(d). By varying the excitation energy across the exciton resonance (see Figure 4.2(c) for comparison), the maximum amplitudes of the SF signal are evaluated in a magnetic field of $B_V = 7\,T$ at a fixed power density of $P = 5.7\ W/cm^2$.

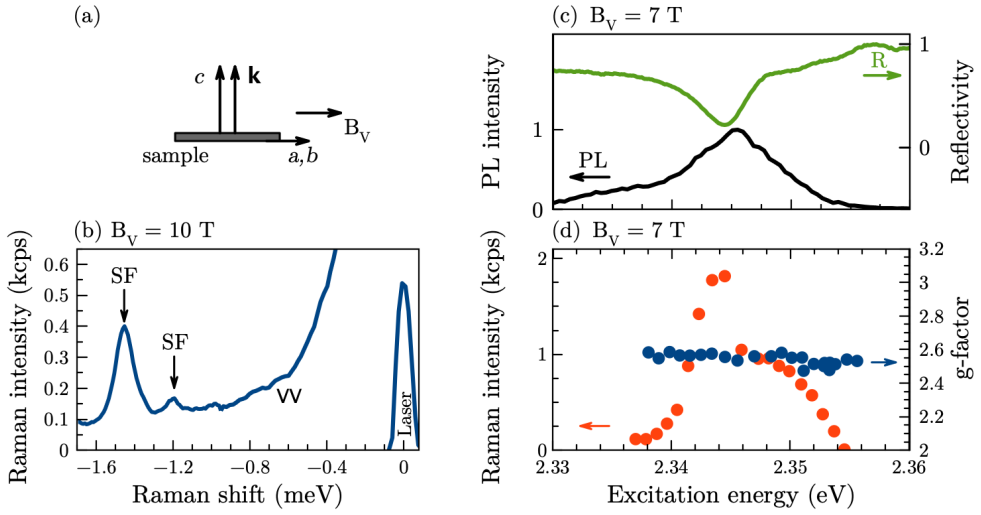

Figure 4.2: (a) Schematic of the experimental geometry. In Voigt geometry, the magnetic field $B_V \parallel (a, b)$ with the laser light vector $\mathbf{k} \parallel c$. (b) SFRS spectrum at $B_V = 10\,T$, excited at $E = 2.345\,eV$ with a power density of $P = 5.7\ W/cm^2$ for vertically co-linear polarization. SFs are marked by vertical arrows. (c) Normalized PL and reflectivity spectra are given for comparison. (d) Resonance profile of the strong SF line with larger Raman shift at $B_V = 7\,T$ (red dots) and its g-factor dependence on the excitation energy at $T = 1.6\,K$ (blue dots).

As shown by the resonance profile, the SF intensity exhibits a strong spectral dependence on the laser energy, with the highest SF intensity observed at the exciton resonance, where $E_X = 2.345\,eV$. This observation highlights the key role of the exciton in the SFRS process. Throughout the rest of this section, the laser photon energy is fixed at $E_{exc} = 2.345\,eV$. Note that the value of the g-factor remains unaffected by variations in the excitation energy (see blue dots in Figure 4.2(d)). This observation indicates that the exciton resonance is mainly homogeneously broadened, suggesting that the layer thickness of the sample remains relatively constant across the excited sample spot.

As a next step, the influence of temperature on the SF intensity will be discussed. The magnetic field is set to $B_V = 7\,T$ in Voigt geometry. In Figure 4.3(a), the SFRS anti-Stokes spectra at temperatures of 5 K and 12 K are compared. At $T = 5\,K$, both SFs are pronounced, whereas at $T = 12\,K$ only one SF with significantly reduced intensity remains visible. The intensity of the stronger SF decreases as the temperature rises and becomes nearly undetectable above 16 K (see the green dots in Figure 4.3(b)). The temperature dependence of the SF intensity for resident carriers follows the Arrhenius-like equation [15]

$$I(T) = \left(A \exp\left(-\frac{E_A}{k_B T}\right) + C\right)^{-1}, \tag{4.1}$$

where E_A denotes the activation energy, and k_B the Boltzmann constant. The fitted parameters are: activation energy $E_A = (2.14 \pm 0.43)\,meV$, amplitude $A = 0.22$, and constant $1/C = 133\,cps$. At a temperature of $T = 5\,K$, the SF intensity is reduced to half its value. We propose that this decrease in intensity is due to the thermal delocalization of resident carriers, which reduces the efficiency of the SFRS process. Therefore, to maximize the SF intensity, the SFRS spectra are measured at the lowest temperature of $T = 1.6\,K$. In contrast to the SF intensity, the full width at half maximum (FWHM) of the SF (black points in Figure 4.3(b)) remains nearly constant at around 0.1 meV. Additionally, the g-factor remains stable around $g = 2.5 \pm 0.1$ across the temperature range of 1.6 K to 16 K, as depicted in Figure 4.3 (c), indicating negligible changes in the band structure within this temperature range.

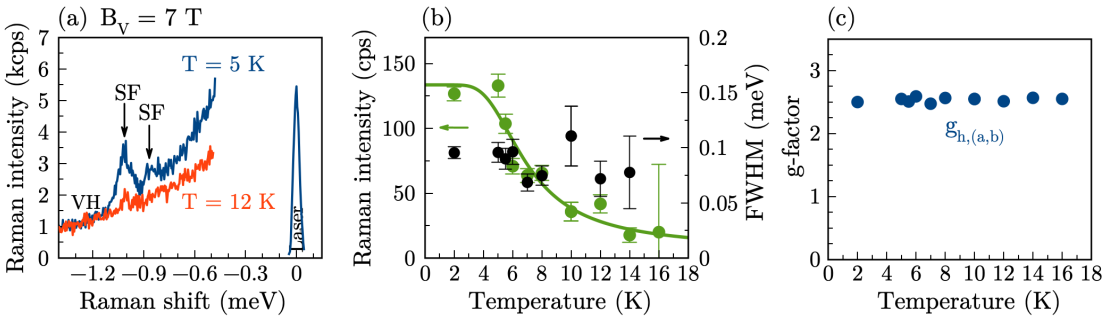

Figure 4.3: Temperature dependence of SFRS measured in Voigt geometry at $B = 7\,T$ with a power density of $P = 5.7\,W/cm^2$. (a) Anti-Stokes spectra for 5 K (blue) and 12 K (red). Both spectra are multiplied by a factor of 10 to enhance the visibility of the SFs. (b) Decrease in the amplitude of the more pronounced SF line (green dots) fitted with an Arrhenius-like equation (green line). Temperature dependence of the FWHM of the SF (black dots) (b) and g-factor (c).

In various studies of SFRS on conventional semiconductors, polarization-resolved measurements were performed to explore the optical selection rules and to identify both the type of charge carrier involved in the scattering and the underlying scattering mechanism [24, 169]. Figure 4.4 presents the polarization dependence of the strong SF line in both Voigt and close-to-Faraday ($\theta = 22°$) geometry measured at $B = 6T$. To improve the comparability of the SF peaks for different polarization configurations, the background signals are subtracted following the analysis method described in Section 2.3. The SF intensities are measured for both co- and cross-polarization configurations. As discussed in Section 1.3, polarization-dependent measurements in Voigt geometry are performed using linear polarization configurations, while circular polarization configurations are used for close-to-Faraday geometry. The polarization configuration is denoted by two letters: the first letter indicates the excitation polarization, and the second letter refers to the detection polarization. The SF signals on anti-Stokes in both close-to-Faraday and Voigt geometry are multiplied by a factor of seven to improve the visibility of the SF.

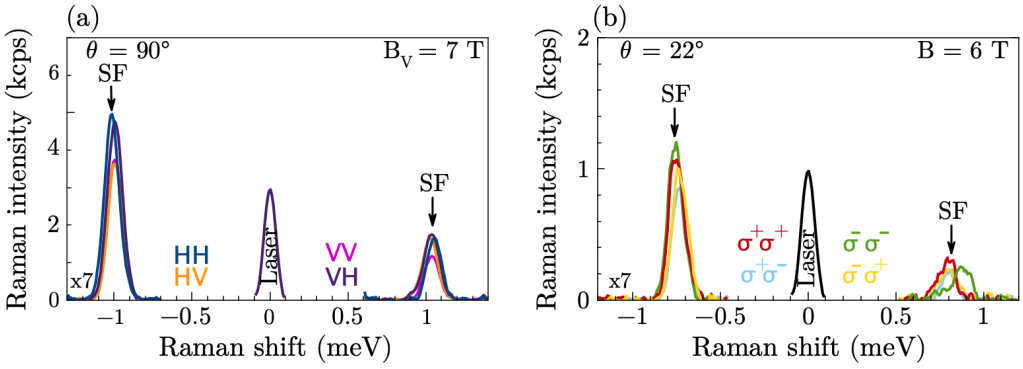

Figure 4.4: Polarization dependence of the SFRS spectra in Voigt (a) and in tilted field $\theta = 22^\circ$ (b) geometry for $P = 5.7$ W/cm^2. The polarizations are given in the order of excitation/detection. Linear polarization configurations in (a) and circular polarization configurations in (b). The anti-Stokes spectra are multiplied by a factor of seven to increase the visibility of the SF.

By comparing Figures 4.4(a) and (b), it can be seen that the SF intensity in Voigt geometry is approximately five times higher than in close-to-Faraday geometry, indicating enhanced SF efficiency as the sample is tilted towards Voigt geometry. However, for 2D $(PEA)_2PbI_4$, polarization effects are not as pronounced as in bulk $MAPbI_3$ (see Section 3), which might be attributed to the reduced symmetry of the structure along the *c*-axis. Therefore, the polarization dependence is not discussed in detail. The weak polarization dependence observed in both geometries indicates the absence of clear selection rules, preventing a determination of the *g*-factor sign. Therefore, in Section 4.1.3, we investigate the *g*-factor sign through dynamic nuclear polarization.

With the optimal experimental conditions for enhancing the SF intensity, we proceed to analyze the Raman shift of the SFs to determine the *g*-factors and attribute them to the respective charge carriers. The SFRS spectrum in close-to-Faraday geometry, measured at a magnetic field of $B = 9.4$ T, is shown in Figure 4.5(b). The SFRS spectrum is presented for the anti-Stokes spectral range, where the absence of resonant PL leads to a more pronounced SFs compared to the Stokes spectral range. To minimize the influence of scattered laser light on the SFRS spectrum, measurements are performed in cross-circular polarization ($\sigma^+\sigma^-$).

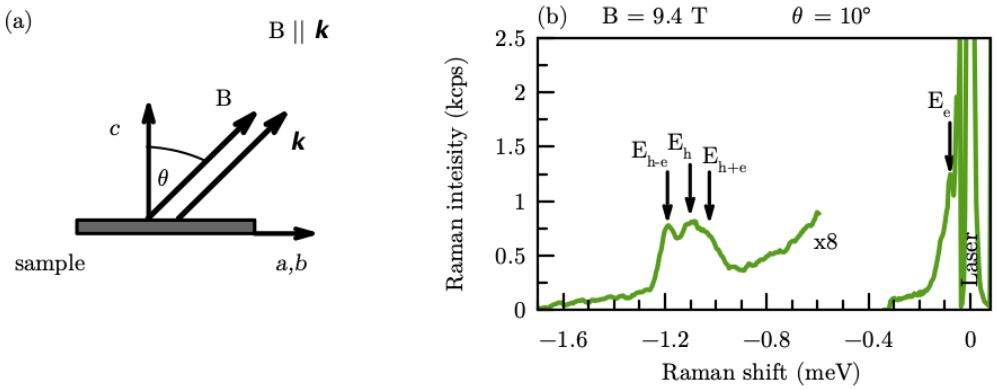

Figure 4.5: (a) Schematic of the experimental geometry for tilted configuration, where the tilt angle θ is between the magnetic field and *c* axis, with $\mathbf{B} \parallel \mathbf{k}$. (b) SFRS spectrum measured at $\theta = 10^\circ$ with excitation energy $E_{exc} = 2.345$ eV and power density $P = 5.7$ W/cm^2.

In the SFRS spectrum measured in close-to-Faraday geometry ($\theta = 10^{\circ}$), shown in Figure 4.5(b), four SF lines, marked by vertical arrows, can be identified. The magnetic field dependences of their Raman shifts are presented in Figure 4.6. As the magnetic field increases, the SFs shift linearly from the laser (referred to as zero). The SF line with a Raman shift of −1.14 meV, corresponding to a g-factor value of $|g| = 2.11$, is attributed to the resident hole based on the general trend observed in Figure 4.19. Next to the SF of the resident hole, two peaks appear symmetrically with the same energetic distance to the left and right of it. In high magnetic fields of $B_{\mathrm{F}} = 9.4\,\mathrm{T}$ and above, a SF near the laser line emerges, exhibiting a small Raman shift of only −0.08 meV, as shown in Figure 4.5(b). The corresponding small g-factor of $|g_{\mathrm{c,e}}| = 0.13$ is attributed to the resident electron. At this point, it is important to emphasize that the sign of the g-factors cannot be determined. Interestingly, the distance between the hole SF and the side peaks matches the Raman shift of the electron, supporting the assignment of the side peaks to the combined SFs of resident electrons and holes, with g-factors of $|g_{\mathrm{c,h+e}}| = 1.94$ and $|g_{\mathrm{c,h\text{-}e}}| = 2.25$. This combined SF processes, which involves both electron and hole SFs, is a rather unusual SFRS process. However, double SF processes have been reported in the literature experimentally for CdS [170] and ZnSe [171] and theoretically in References [37, 146]. The SF lines corresponding to $E_{\mathrm{h\pm e}}$ can be distinguished from the hole SF in magnetic fields exceeding $B = 3\,\mathrm{T}$. Consequently, the Raman shift of the electron can be determined for magnetic fields smaller than $B = 9.4\,\mathrm{T}$ by calculating the difference in Raman shifts between the combined carrier and hole, as indicated by the crosses in Figure 4.6(c).

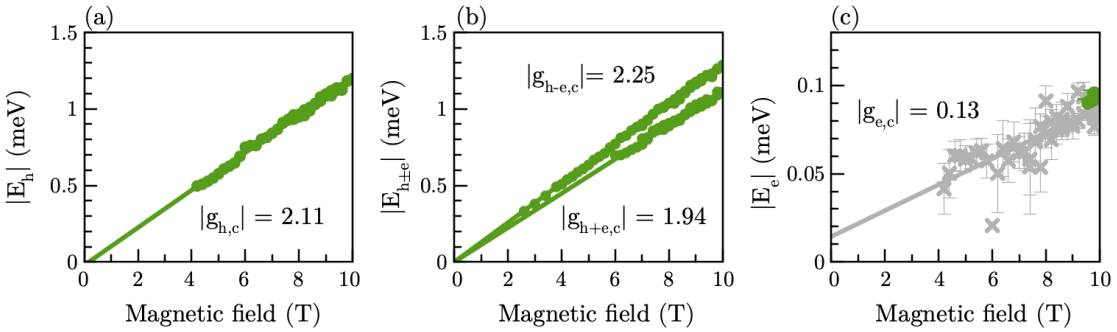

Figure 4.6: Raman shifts of the SF lines in magnetic field and evaluated g-factors in close-to-Faraday geometry for (a) hole, (b) combined carriers, and (c) electron. Direct measurements of the Raman shifts represented by green dots and calculated electron Raman shifts by gray crosses. The fit to linear functions (solid lines) allows to extract the g-factors. Errors are reflected in the thickness of the data points.

In Voigt geometry the SFRS spectrum is measured in linearly co-polarization (V/V) shown for $B = 10\,\mathrm{T}$ in Figure 4.2(b). The SFs of hole and combined carrier are labeled as E_{h} and $E_{\mathrm{e+h}}$. Their g-factors are $|g_{\mathrm{h,(a,b)}}| = 2.50$ and $|g_{\mathrm{h+e,(a,b)}}| = 1.98$. As discussed above, the SF intensity is five times higher in Voigt geometry compared to close-to-Faraday geometry. However, the electron SF cannot be resolved in this experimental configuration. To determine the electron g-factor in Voigt geometry, we calculate the electron Raman shift from the difference between the Raman shift of the hole and the combined carrier (see Figure 4.7(c)), yielding a g-factor of $|g_{\mathrm{e,(a,b)}}| = 0.51$. Based on this g-factor value, we would expect to observe the electron SF at a Raman shift approximately −0.30 meV in the SFRS spectrum shown in Figure 4.2(b). Note that the second line from the combined carrier (h-e) is not well detectable and can only be observed in a magnetic field of $B_{\mathrm{V}} = 7\,\mathrm{T}$.

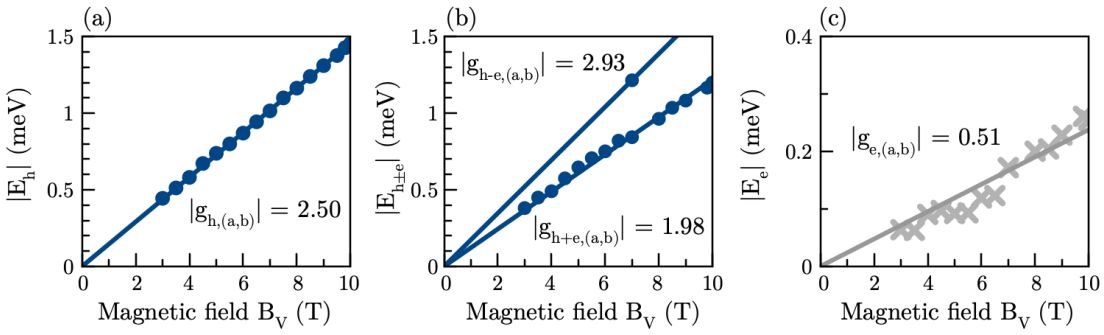

Figure 4.7: Raman shifts of the SF lines in magnetic field and evaluated g-factors in Voigt for (a) hole, (b) combined carriers, and (c) electron. Direct measurements of the Raman shifts represented by blue dots and calculated electron Raman shifts by gray crosses. The fit to linear functions (solid lines) allows to extract the g-factors.

A comparison of the g-factors for the electron, hole, and their combinations reveals an anisotropy in the g-factors between close-to-Faraday and Voigt geometry. Such an anisotropy in 2D materials is expected as the symmetry of the structure is reduced along the c-axis. The angular dependence of the g-factor on the magnetic field is further investigated by rotating the sample holder, enabling measurements at intermediate angles between Faraday and Voigt geometry, as presented in Figure 4.8.

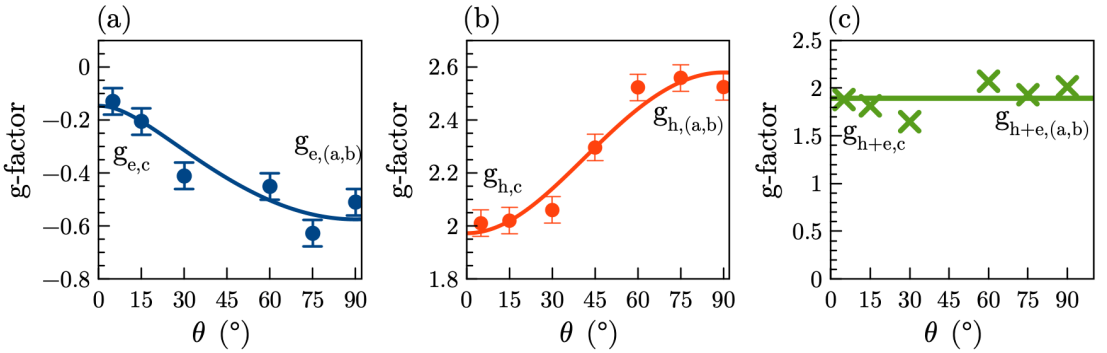

Figure 4.8: Angular dependence of the measured electron (a) and hole (b) g-factors, as well as the calculated combined carrier g-factors (c), shown as crosses. The g-factor anisotropies are denoted in Faraday geometry by a tilt angle $\theta = 0°$ with subscript c, and in Voigt geometry by $\theta = 90°$ with subscripts (a, b). Lines are fits to Equation (3.12).

The g-factor anisotropies of electron and hole, which can be described by Equation (3.12), nearly compensate each other. As a result, the g-factors of the combined carriers ($g_{e,c} + g_{h,c} = 1.98$ and $g_{e,(a,b)} + g_{h,(a,b)} = 1.99$), remain nearly isotropic, as shown in Figure 3.12(c). In comparison to the exciton g-factor of $g_{X,c} = +1.6$, measured by magneto-reflectivity in Section 4.1.1, the combined carrier g-factor calculated from the individual electron and hole g-factors is approximately 0.4 larger. We attribute this difference to the large binding energies of excitons in 2D perovskites. However, further model calculations would be necessary to identify the underlying mechanisms.

4.1.3 Dynamic nuclear polarization

To determine the sign of the g-factors, we analyze the hyperfine interaction of carriers with the lattice nuclei that can be addressed by the effect of dynamic nuclear polarization (DNP). Experimentally, we can observe DNP by exciting the 2D perovskites with circularly polarized light, measure two SFRS spectra for σ^+ and σ^- polarizations while keeping the circular polarization fixed in detection in a longitudinal magnetic field. Depending on the g-factor sign, the effective nuclear field (Overhauser field B_N) can increase or reduce the Zeeman splitting and, consequently, the Raman shift induced by the external magnetic field. Therefore, if the comparison of the Raman shift between the different excitation polarizations shows any difference, an interaction between the carrier and nuclear spin systems is involved. The SFRS spectra are measured at a magnetic field of $B = 10$ T. According to Equation (1.12), the orientation of the magnetic field has a strong influence on the strength of the DNP, with the maximum occurring in pure Faraday geometry. As discussed in Section 1.6.3, the SFRS signal in pure Faraday geometry is absent. Thus, we slightly rotate the sample from Faraday to close-to-Faraday geometry ($\theta = 10°$). In Figure 4.9, the SFRS spectra are separated into two spectral regions to highlight small differences in the Zeeman splitting of the electron, hole, and their combination arising from DNP.

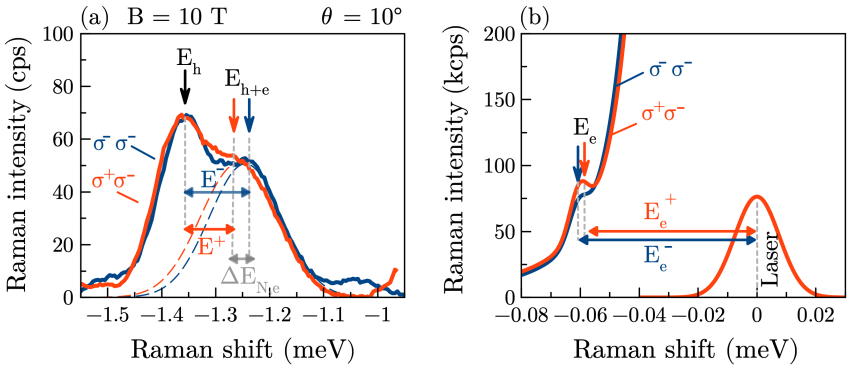

Figure 4.9: SFRS spectra excited with different circular polarization, σ^+ (red) and σ^- (blue), at $B = 10$ T in close-to-Faraday geometry ($\theta = 10°$), with σ^- in detection. The gray dashed lines mark the peak maxima. (a) Raman shift of the hole E_h and combined carrier E_{h+e} for $P = 13.5$ W/cm^2. Horizontal arrows indicate the energy differences $E^\pm$ between the combined carrier SF and the hole SF for $\sigma^\pm$ excitation. Energy splitting $\Delta E_{N,e} = E^+ - E^-$ scales with twice the Overhauser field. Blue and red dashed line represent the fits to Gaussian functions to make the energy shift more visible. (b) Raman shift of the electron E_e for $P = 5.7$ W/cm^2.

As shown in Figure 4.9, a difference in Raman shift is observed between σ^+ and σ^- polarization excitations for both electron and combined SFs, while no difference is observed for the hole SF. In general, for lead halide perovskites, both electrons and holes can interact with the nuclei [18, 73]. However, the effect on the electron is typically smaller due to its p-type wave function, in contrast to the hole's s-type wave function, as discussed in Section 1.5. Several parameters contribute to DNP, including the g-factor, external magnetic field, and laser power. For an effective hyperfine interaction between the nuclear spin system and the carrier spin system, their Zeeman splittings must be comparable. The Hamiltonian describing the interaction of the nuclei in an external magnetic field is analogous to the Hamiltonian for carriers (Equation (1.3)), but it incorporates the nuclear g-factor, g_N, and the nuclear magneton, μ_N, instead. As the nuclear magneton is three orders of magnitude smaller than the Bohr magneton, the Zeeman splitting of nuclear spin sublevels is correspondingly three orders of magnitude smaller than that of the carrier spin sublevels. When a large magnetic field is applied, such as 10 T in Figure 4.9, the difference becomes

significant. Due to a smaller g-factor for the electron, the carrier Zeeman splitting is closer to the Zeeman splitting of the nuclei. Although the hyperfine interaction is typically stronger for the s-type wave function of the hole compared to the p-type wave function of the electron it is not strong enough to overcome the large Zeeman splitting. Consequently, to observe DNP for the hole, measurements in small magnetic fields may be successful. Furthermore, the strength of DNP strongly depends on the laser power (see Figure 4.11). If the power is too low, the nuclear spin polarization is small, leading to a weak DNP. Conversely, if the laser power is too high, heating of the nuclear spin system can occur, which weakens the effect of DNP. Therefore, finding the optimal laser power is crucial for achieving a strong effect of DNP. Successfully observing DNP in a sample demands precise alignment of all contributing factors, presenting a significant challenge. Under the experimental conditions shown in Figure 4.9, the strong influence of DNP on the Zeeman splitting of the electron leads us to focus on its interaction with the nuclei, as electrons dominate in polarizing the nuclei. With DNP, we can thus determine the sign of the electron. Therefore, we calculate the difference of the electron Raman shift $\Delta E_{\mathrm{N,e}} = E_{\mathrm{e}}^{+} - E_{\mathrm{e}}^{-} = -1.6\,\mu\mathrm{eV}$ for a power density of $P = 5.7\ \mathrm{W/cm^2}$, which scales with twice the Overhauser field

$$\Delta E_{\mathrm{N,e}} = |E_{\mathrm{e}}^{+}| - |E_{\mathrm{e}}^{-}| = 2|g_{\mathrm{e}}|\mu_B B_{\mathrm{N,e}}. \tag{4.2}$$

The impact of DNP on the Raman shift is more clearly observed in the combined SF $E_{\mathrm{h+e}}$ (see Figure 4.9(a)) due to the reduced background from scattered light near the laser. The energy splitting amounts to $\Delta E_{\mathrm{N,e}} = -5.5\,\mu\mathrm{eV}$ for $P = 13.5\ \mathrm{W/cm^2}$. In Section 4.1.2, the electron g-factor was determined in close-to-Faraday geometry, yielding $|g_{\mathrm{e,c}}| = 0.13$. Inserting the values in Equation (4.2) results in an Overhauser field of $B_{\mathrm{N,e}} = -0.11\,\mathrm{T}$ for $P = 5.7\ \mathrm{W/cm^2}$ and $B_{\mathrm{N,e}} = -0.36\,\mathrm{T}$ for $P = 13.5\ \mathrm{W/cm^2}$. Consequently, the negative sign of $B_{\mathrm{N,e}}$ means that $g_{\mathrm{e,c}} < 0$. For this situation, the schematic of the hyperfine interaction of electrons and nuclei is shown in Figure 4.10.

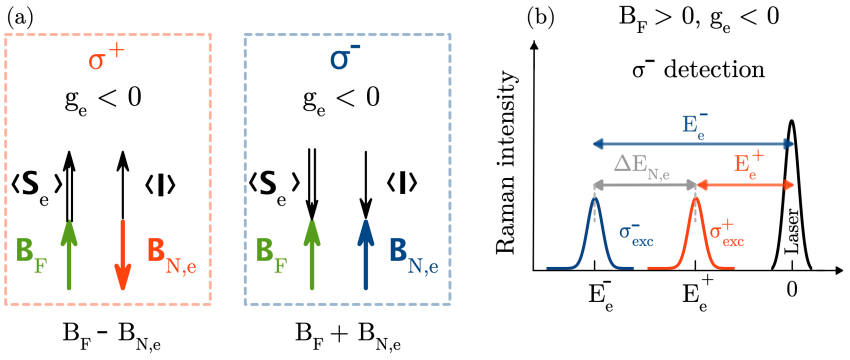

Figure 4.10: (a) Schematic illustration of the electron Overhauser field $B_{\mathrm{N,e}}$ orientations for $g_{\mathrm{e}} < 0$ under σ^+ (red) and σ^- (blue) excitation, with an external magnetic field applied in Faraday geometry B_{F}. The Overhauser field either reduces ($B_{\mathrm{F}} - B_{\mathrm{N,e}}$, left panel) or increases ($B_{\mathrm{F}} + B_{\mathrm{N,e}}$, right panel) the Zeeman splitting. (b) Schematic SFRS spectrum in the anti-Stokes spectral range, illustrating the effect of DNP ($\Delta E_{\mathrm{N,e}}$) on the Raman shift, as depicted in (a).

To spin-polarize the electrons ($\langle \mathbf{S}_{\mathrm{e}} \rangle$) we use circularly polarized light. Depending on the light's helicity, the orientation of $\langle \mathbf{S}_{\mathrm{e}} \rangle$ can be adjusted. The effective Knight field $\mathbf{B}_{\mathrm{K}}$ transfers the orientation of the electrons to the nuclei, aligning the average nuclear spin polarization $\langle \mathbf{I} \rangle$ in the same direction as the spin-polarized electrons. The sign of the Overhauser field is determined

by the sign of the electron g-factor. In Figure 4.10(a), the effect of the electron Overhauser field for different circular polarization excitations, $\sigma^{\pm}$, on the external magnetic field is shown for a negative g-factor. For a negative g-factor under σ^+ excitation, $B_{N,e}$ points in the opposite direction compared to the external magnetic field B_F, thereby reducing the Zeeman splitting ($B_F - B_{N,e}$). In σ^- excitation, the situation is reversed: $B_{N,e}$ and B_F now point in the same direction, resulting in an increased Zeeman splitting ($B_F + B_{N,e}$) (see Figure 4.10(a)). The impact of this situation on the SFRS spectrum is schematically depicted in Figure 4.10(b). Under σ^+ excitation, the SF exhibits a smaller Raman shift, positioning it closer to the laser line, as the Zeeman splitting is reduced by the effective nuclear field. Conversely, under σ^- excitation, the SF shows a larger Raman shift. This matches the experimental observations shown in Figure 4.9, which results in a negative electron g-factor. As we induce the electron spin polarization optically and observe variations in the strength of the Overhauser field, determined from the electron ($B_{N,e} = -0.11\,\mathrm{T}$ for $P = 5.7\ \mathrm{W/cm^2}$) or combined carrier ($B_{N,e} = -0.36\,\mathrm{T}$ for $P = 13.5\ \mathrm{W/cm^2}$), we aim to experimentally find the maximum achievable Overhauser field in this sample by investigating its dependence on excitation density in Figure 4.11.

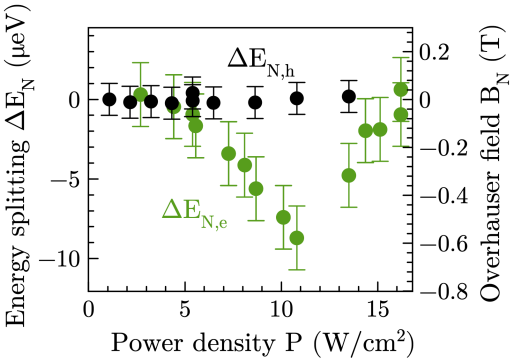

Figure 4.11: Power dependences of the energy splitting $\Delta E_N = E^+ - E^-$ for hole (black) and electron (green) exemplarily shown in Figure 4.9(a) for one power density, along with the calculated Overhauser field B_N. While hole DNP is absent, electron DNP exhibits a strong dependence on excitation density.

Experimentally, we can indeed observe a strong influence of excitation density on the electron energy splitting $\Delta E_{N,e}$ (see green dots in Figure 4.11) and consequently on the Overhauser field, as a higher power density results in more oriented electron spins. The more electron spins are oriented, the greater the nuclear spin polarization, which in turn contributes linearly to the strength of the Overhauser field. The Overhauser field increases linearly with power density up to $P = 10.6\ \mathrm{W/cm^2}$, reaching $B_{N,e} = -0.6\,\mathrm{T}$ ($\Delta E_{N,e} = -8.7\,\mu\mathrm{eV}$). At higher excitation densities, $\Delta E_{N,e}$ decreases, which we attribute to the heating of the nuclear spin system. Note that the excitation density has no effect on the Raman shift of the holes.

To gain a comprehensive understanding of the impact of reduced dimensionality on the g-factor in 2D RP perovskites, detailed studies of samples with variation of the inorganic layer thickness (lead halide octahedra) n and halide compositions are needed, which are presented in the following.

4.2 Influence of the 2D inorganic layer thickness on the optical and spin properties in $(PEA)_2(MA, FA)_{n-1}Pb_n(I, Br)_{3n+1}$

We commence our study of $(PEA)_2(MA, FA)_{n-1}Pb_nX_{3n+1}$ with X = I, Br following the same procedure as presented for $(PEA)_2PbI_4$ with $n = 1$. In $(PEA)_2PbI_4$ with $n = 1$, the exciton resonance was observed in the green spectral range. By varying the inorganic layer thickness (number of lead halide octahedra layers) n and the halide X, the exciton resonance is adjusted across a broad energy range, requiring a precisely tunable laser system for excitation.

As a first step, we analyze the PL and absorption/reflectivity spectra of $(PEA)_2MA_{n-1}Pb_nI_{3n+1}$ and $(PEA)_2FA_{n-1}Pb_nBr_{3n+1}$, shown in Figure 4.12. For $(PEA)_2MA_{n-1}Pb_nI_{3n+1}$ (see Figure 4.12(a)), seven exciton resonances are observed in the reflectivity spectrum, each corresponding to a different number of inorganic layers n. By varying n, the exciton resonances for $(PEA)_2MA_{n-1}Pb_nI_{3n+1}$ shift across an energy range from 1.75 eV for $n = 7$ to 2.342 eV for $n = 1$. The strong exciton resonance characteristics for lower n values become less pronounced as n increases. For $(PEA)_2FA_{n-1}Pb_nBr_{3n+1}$, presented in Figure 4.12(b), five distinct peaks are visible in the PL spectrum, each with a corresponding exciton resonance nearby. The substitution of the halide from iodine to bromide shifts the exciton resonances to a higher energy range, reaching up to 3.054 eV. As n increases, the excitonic absorption shifts to lower energies, ranging from 3.054 eV for $n = 1$ to 2.435 eV for $n = 5$. The assignment of these resonances to specific numbers of inorganic layers is based on literature: Reference [172] for low-n iodine perovskites, Reference [173] for higher-n iodine perovskites, and Reference [174] for bromide perovskites. In Figure 4.12(c) the evaluated exciton resonance energies, derived from reflectivity or absorption spectra for the iodine and bromide series, are presented as a function of the number of inorganic layers n. The systematic monotonic decrease in exciton resonance energy with increasing n suggests that these exciton resonances correspond to the different n phases. The samples of $(PEA)_2MA_{n-1}Pb_nI_{3n+1}$ and $(PEA)_2FA_{n-1}Pb_nBr_{3n+1}$ with different n covering the blue, green and red spectral range enable us to measure the g-factor dependence for 2D RP perovskites over a broad energy range. The g-factor dependence for 2D RP perovskites is compared to the universal dependence of the electron and hole g-factors as a function of the band gap energy in bulk lead halide perovskites. This comparison enables us to investigate how a shift in the effective band gap through quantum confinement modifies the g-factor, in contrast to a shift of the band gap induced by compositional substitution.

To observe SFs and determine their g-factors for varying n in Faraday and Voigt geometry, we set the excitation energy of the laser in the exciton resonance of each n. The measurement procedure is the same as described for $(PEA)_2PbI_4$ with $n = 1$, which is discussed in detail in Section 4.1.2. However, here we will only present exemplary results for two samples: $(PEA)_2Pb_nBr_4$ with $n = 1$ and $(PEA)_2MA_3Pb_4I_{13}$ with $n = 4$. These samples are selected to demonstrate SFRS measurements across the full energy range, from $E_{exc} = 3.057$ eV to $E_{exc} = 1.839$ eV, respectively. Note that, for simplicity, we refer to the slightly tilted Faraday and Voigt geometries just as Faraday and Voigt geometries, as the experimental setup prevents perfect alignment of the light's wave vector to parallel or perpendicular to the magnetic field, as discussed in Section 2.1.3.

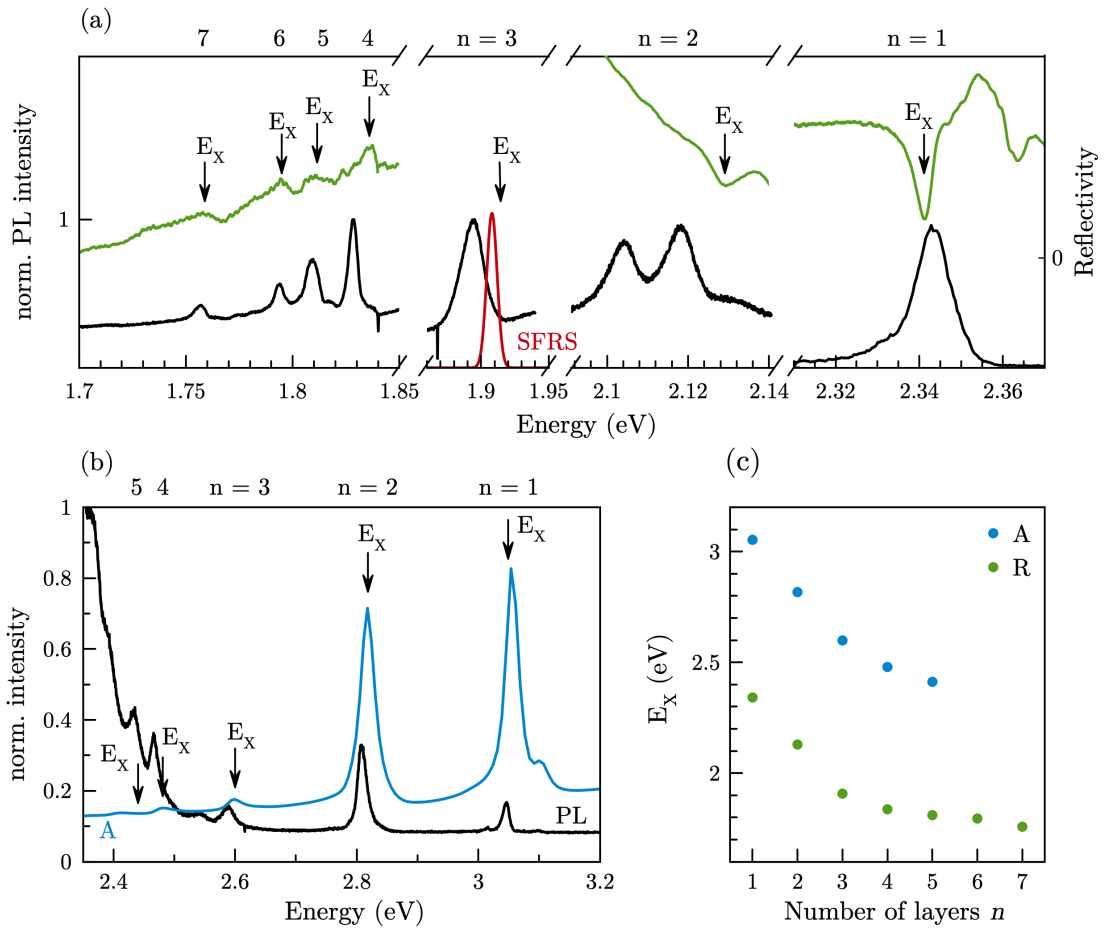

Figure 4.12: Optical properties of 2D RP type perovskites $(PEA)_2MA_{n-1}Pb_nI_{3n+1}$ and $(PEA)_2FA_{n-1}Pb_nBr_{3n+1}$. (a) Normalized PL (black) and reflectivity (green) spectra for $(PEA)_2MA_{n-1}Pb_nI_{3n+1}$. Maximum of the resonance profile measured by SFRS (red). (b) Normalized PL and absorption (blue) spectra for $(PEA)_2FA_{n-1}Pb_nBr_{3n+1}$. The PL is excited at $E_{exc} = 3.493$ eV at a temperature of $T = 1.6$ K. The absorption is measured at $T = 4$ K. Exciton resonances E_X for varied inorganic layer thickness n are marked by vertical arrows. (c) Positions of the exciton resonances, extracted from reflectivity spectra for $(PEA)_2MA_{n-1}Pb_nI_{3n+1}$ and from absorption spectra for $(PEA)_2FA_{n-1}Pb_nBr_{3n+1}$, as a function of the number of inorganic layers n.

4.2.1 Spin properties of $(PEA)_2FA_{n-1}Pb_nBr_{3n+1}$

In Figure 4.13(a), the SFRS spectra for $(PEA)_2PbBr_4$ with $n = 1$ are compared in Faraday and Voigt geometry at a magnetic field of $B = 10$ T. Both spectra exhibit a pronounced SF at a Raman shift of approximately 1.2 meV, which can be attributed to the hole. Additionally, a second, less pronounced SF corresponding to the exciton can be observed in the magnetic field. The assignment of the carriers is based on the g-factor layer dependence shown in Figure 4.15, which is further supported by additional measurements on the same sample batch using time-resolved Kerr rotation (TRKR), performed by Evgeny Zhukov.

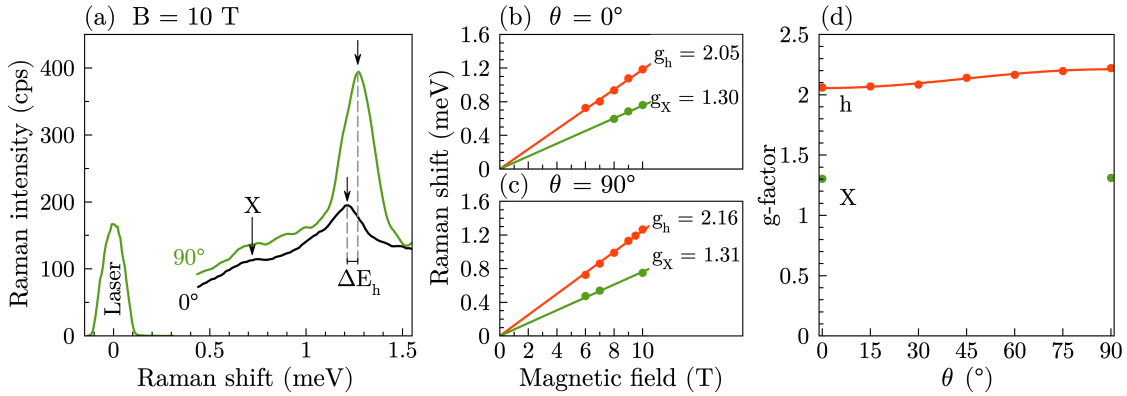

Figure 4.13: (a) SFRS spectra for $(PEA)_2PbBr_4$ ($n = 1$) in Faraday ($\theta = 0°$, black) and Voigt geometry ($\theta = 90°$, green) excited with excitation energy $E_{exc} = 3.057$ eV and power density $P = 0.3$ W/cm^2. SFs of hole and exciton are indicated by vertical arrows, the differences in hole Raman shifts resulting from the magnetic field geometry are denoted as ΔE_h. (b, c) Raman shifts of the SF lines in magnetic field for the hole and exciton in Faraday (b) and Voigt geometry (c). The fit to linear functions (solid lines) allow to determine the carrier g-factors. (d) hole g-factor anisotropy described by Equation (3.12).

The Raman shift of the hole in Faraday and Voigt geometry differs by ΔE_h, as highlighted by the dashed gray lines in Figure 4.13(a). The SF intensity in Voigt geometry is higher than in Faraday geometry due to the enhanced SF probability. In the magnetic field, the Raman shifts of the SFs are traced and plotted in Figure 4.13(b) for Faraday and in Figure 4.13(c) for Voigt geometry. The g-factors determined from the slope of the linear fits based on the Zeeman equation (Equation (2.2)) are $g_h = 2.05$ and $g_h = 2.16$ for the hole in Faraday and Voigt geometries, respectively, while the exciton g-factors are $g_X = 1.30$ and $g_X = 1.31$ in the corresponding geometries. Using Equation (3.13), the g-factor anisotropy of the hole is determined to be 5%, whereas the g-factor of the exciton is nearly isotropic. The angular dependences of the hole and exciton g-factors are presented in Figure 4.13(d), including measurements at additional intermediate angles in steps of $\theta = 15°$. The hole SF is pronounced in both Faraday and Voigt geometries (see Figure 4.13(a)), therefore the hole SF remains clearly observable in tilted magnetic field geometries. In contrast, the exciton SF, which exhibits lower intensity, is only observed in Faraday and Voigt geometries. The bright exciton g-factor defined as $g_X = g_h + g_e$ is found to be nearly isotropic, as the anisotropies of the electron and hole g-factor tend to compensate each other [125]. Note that in SFRS spectra, the g-factor value and anisotropy for excitons and combined SF processes are similar. However, they can be distinguished by their polarization properties. Exciton SFs typically exhibit a polarization dependence [24], whereas combined carrier SF processes do not. As we do not observe pronounced polarization properties in 2D perovskites, as shown exemplarily in Figure 4.4, this suggests that the SF process is most likely associated with a combined carrier SF than an exciton. However, if the electron SF is not observed in the SFRS spectrum, it is unlikely to detect a combined SF process involving an electron, as combined SF processes are less probable than single SF processes [37]. Therefore, we attribute the signal to the exciton, although this distinction is of minor importance since our focus is on the electron and hole g-factors.

By measuring a sample from the same synthesis batch using two different magento-optical techniques, such as SFRS and TRKR, we can combine the data provided by each method, taking advantage of their individual strengths. SFRS is sensitive to signals from individual carriers, their combinations, and excitons, while TRKR primarily detects resident carriers with nanosecond spin relaxation times. Although TRKR can also probe excitons, their spin lifetime is limited by

their short recombination time. To further explore the coherent spin dynamics of charge carriers, we investigate $(PEA)_2FA_{n-1}Pb_nBr_{3n+1}$ by TRKR.

In general, the principle of TRKR involves the generation of spin-polarized electrons and holes by circularly polarized pump pulses, with the spin polarization S_c oriented along the wave vector of the pump light and perpendicular to the sample surface. When a transverse magnetic field is applied in Voigt geometry, it induces a Larmor precession of the carrier spins around this magnetic field, leading to a loss of spin polarization over time. The dynamics of the spin polarization are detected by linearly polarized probe pulses, which are delayed with respect to the pump pulses. The changes in the Kerr rotation are observed as the spin polarization decays due to spin dephasing. The signal is described by a decaying oscillatory function

$$A_{KR} = S_c \cos(\omega_{L,c} t) \exp(-t/T^*_{2,c}). \tag{4.3}$$

with the signal amplitude S_c, Larmor precession frequency $\omega_{L,c}$, and carrier spin dephasing time $T^*_{2,c}$. For example, when both the electron and hole contribute to the signal, it is described by the superposition of two decaying oscillatory functions. Modifying the Zeeman equation (Equation (2.2)) by

$$\Delta E = \hbar\omega_{L,c} = g_c \mu_B B, \tag{4.4}$$

enables to determine the carrier g-factor from the Larmor precession frequency $\omega_{L,c}$. [58, 175]

The results of the TRKR measurements obtained for 2D $(PEA)_2PbBr_4$ with $n = 1$ by Evgeny Zhukov are presented in Figure 4.14. The excitation energy of $E_{exc} = 3.068$ eV is close to that used for SFRS measurements.

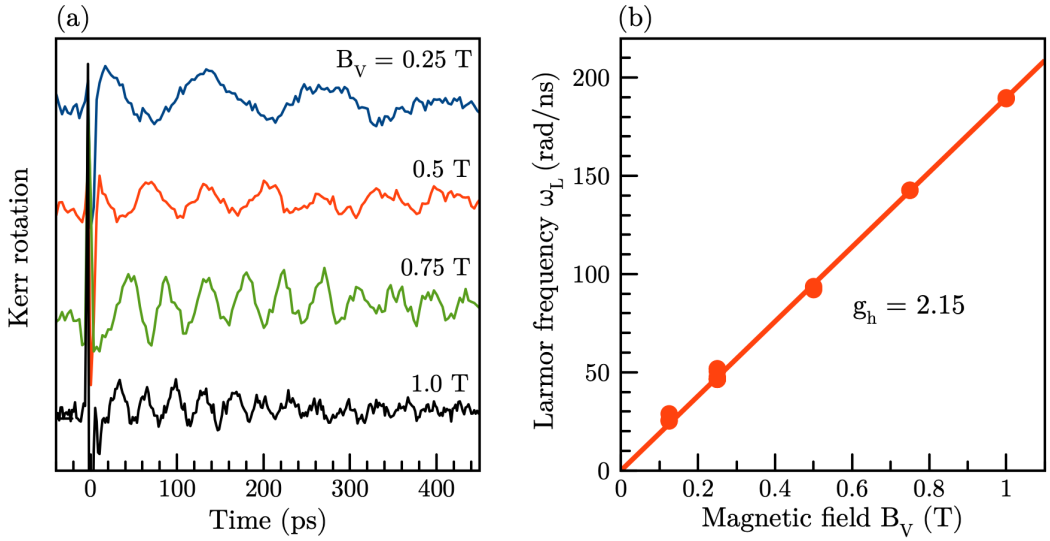

Figure 4.14: Spin dynamics of a resident carrier in $(PEA)_2PbBr_4$ ($n = 1$) in Voigt geometry B_V at $T = 1.6$ K, excited with $E_{exc} = 3.068$ eV. (a) TRKR signals for different magnetic field strengths in 0.25 T steps. Signals are vertically shifted for better visibility. (b) Dependence of the Larmor frequency ω_L on the magnetic field, along with the linear fit based on Equation (4.4) (solid line).

In Figure 4.14(a), the TRKR signals of $(PEA)_2PbBr_4$ with $n = 1$ are shown for different magnetic field strengths applied in Voigt geometry B_V. With increasing magnetic field, the Larmor frequency increases, while the spin dephasing time decreases, indicating faster spin relaxation dynamics. The TRKR signals reveal a single oscillating component, which can be fitted using Equation (4.3). The calculated Larmor frequencies, ω_L, as a function of the magnetic field are presented in Figure 4.14(b). These frequencies exhibit a linear dependence on the magnetic field and demonstrate no offset at zero magnetic field, indicating a vanishing Larmor precession frequency in the absence of a magnetic field. By applying Equation (4.4), the g-factor is calculated to be $g_h = 2.15$.

With the technique of SFRS, we determined two g-factors with values of 2.16 and 1.34 in Voigt geometry. The first g-factor matches the value observed with TRKR, indicating that the same carrier was detected with both techniques. As the coherent spin dynamics of charge carriers can be investigated with TRKR, we assign the g-factor of $g_h = 2.15$ to the hole, based on the trend observed of the hole g-factor with varying inorganic layer thickness, as shown in Figure 4.15. However, the second g-factor of 1.34 cannot be identified in the TRKR signal, as the spin lifetime of the exciton is limited by its short recombination time. Based on the isotropic g-factor for different magnetic field geometries (see Figure 4.13(d)), we conclude that this g-factor corresponds to the exciton, where the g-factor anisotropies of the electron and hole compensate each other [125].

As a next step, the g-factors of the hole and exciton in $(PEA)_2FA_{n-1}Pb_nBr_{3n+1}$, with n ranging from 2 to 5, are measured on the same sample with the technique of SFRS by tuning the laser energy to the corresponding exciton resonance. For a more detailed analysis of the SFRS spectra, including the magnetic field dependences and g-factor anisotropies for each number of the inorganic layer thickness, refer to Appendix A1 (Figures A1 - A3). The g-factors obtained with the techniques of SFRS and TRKR are summarized in Table 4.1.

Table 4.1: Summary of the g-factors for SFRS and TRKR in $(PEA)_2FA_{n-1}Pb_nBr_{3n+1}$.

		SFRS				TRKR
		Faraday		Voigt		Voigt
n	E_{exc}	$g_{h,F}$	$g_{X,F}$	$g_{h,V}$	$g_{X,V}$	$g_{h,V}$
1	3.057 eV	2.05	1.30	2.16	1.34	2.15
2	2.812 eV	2.17	1.21	2.05	1.17	2.10
3	2.600 eV			1.82	1.04	
4	2.467 eV	1.81	0.89	1.59	0.84	1.50
5	2.409 eV	1.67	0.83	1.46	0.83	1.42

Figure 4.15(a) shows the evaluated g-factors as a function of the excitation energy for the bromide series in Faraday geometry, while Figure 4.15(b) presents the corresponding g-factors for Voigt geometry. As described in Section 1.4, we compare the g-factors observed in RP type 2D perovskites with those reported for bulk lead halide perovskites. The solid lines represent fits based on the universal dependences of the electron and hole g-factors on the band gap energy in bulk lead halide perovskites, as presented in Reference [62]. Additionally, we compare the results for the 2D perovskites to $CsPbI_3$ nanocrystals (NCs) as a systematic analysis of the g-factor dependence on quantum confinement in all three dimensions has been performed for this material system. The dashed lines correspond to the dependences derived for lead halide perovskite $CsPbI_3$ NCs [58]. For bulk and NCs, blue indicates the electron g-factor dependence, while red corresponds to that of the hole g-factor.

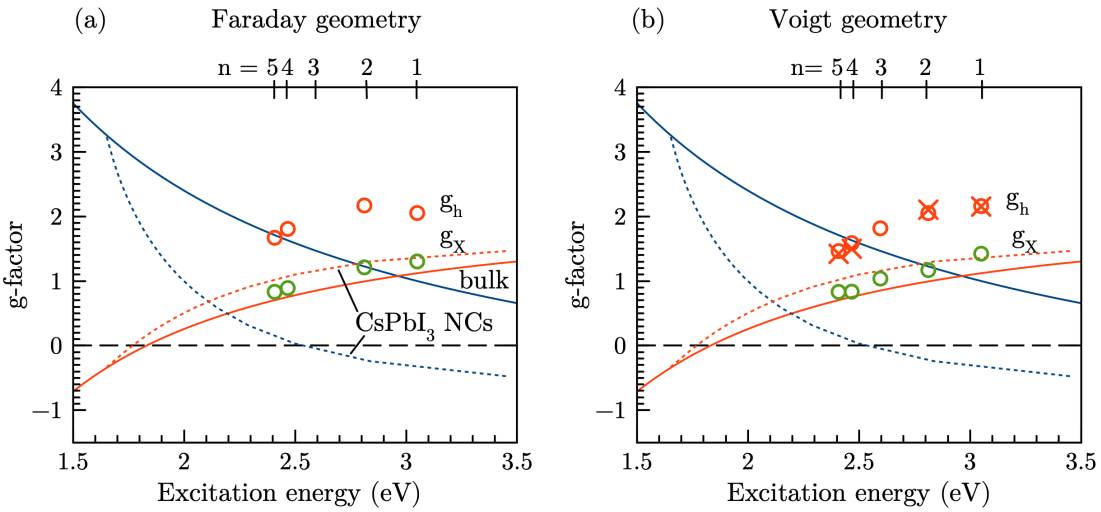

Figure 4.15: Hole and exciton g-factors as a function of the excitation energy in 2D $(PEA)_2FA_{n-1}Pb_nBr_{3n+1}$. Experimental data are represented by open dots for SFRS and crosses for TRKR. Solid lines indicate the universal dependence of the electron and hole g-factors on the band gap energy in bulk lead halide perovskites, as described in Reference [62], while dashed lines correspond to the same dependence derived for lead halide perovskite NCs [58]. (a) Faraday geometry and (b) Voigt geometry.

Experimentally, we can clearly observe a strong influence of the quantum confinement in RP lead halide perovskites on the hole g-factor. A similar trend for the hole g-factor, g_h, as observed in bulk lead halide perovskites, can be seen here: as the excitation energy increases and n decreases, the value of g_h increases. In Faraday geometry, g_h rises from 1.67 at $E_{exc} = 2.409$ eV ($n = 5$) to 2.05 at $E_{exc} = 3.057$ eV ($n = 1$) as n decreases. In Voigt geometry, g_h ranges from 1.46 to 2.16. The g-factor values for the hole, obtained by TRKR (indicated by crosses), are in good agreement with those measured by SFRS. An initial assignment might suggest that within the small energy range for $n = 4$ and $n = 5$, the observed g-factor corresponds to the electron rather than the hole when compared to the bulk electron g-factor dependence. However, for $CsPb(Cl, Br)_3$ NCs, a similar trend for g_h has been observed, where the hole g-factor is close to the bulk value and exhibits a strong dependence on the quantum confinement strength [51]. Additionally, Reference [51] reports a strong hyperfine interaction for this carrier with the nuclei, as expected for holes in lead halide perovskites.

To examine the trend of the g-factors in 2D lead halide perovskites over a broad energy range, we extend this dependence by including the electron and hole g-factors from the iodine series from $(PEA)_2MA_{n-1}Pb_nI_{3n+1}$.

4.2.2 Spin properties of $(PEA)_2MA_{n-1}Pb_nI_{3n+1}$

Figure 4.16 presents the results of the SFRS measurements for $(PEA)_2MA_3Pb_4I_{13}$ with $n = 4$ excited with a photon energy of $E_{exc} = 1.839$ eV and power density of $P = 0.6$ W/cm^2. The SFRS spectra are displayed in the Stokes spectral range, measured at $B = 7$ T in Faraday and in Voigt geometry. In Voigt geometry, a pronounced SF appears at a Raman shift of approximately 0.62 meV, accompanied by a shoulder at 0.52 meV. The magnetic field dependence, shown in Figure 4.16(c), reveals g-factors of $g_h = 1.51$ and $g_e = 1.29$, corresponding to the hole and electron,

respectively. In Faraday geometry at $B_F = 7\,T$, only a single SF at 0.71 meV is observed. From the magnetic field dependence presented in Figure 4.16(b), the electron g-factor is calculated to be $g_e = 1.67$. At higher magnetic fields, an additional SF is identified with a small g-factor of $g_h = 0.25$, attributed to the hole. The g-factor anisotropy shown in Figure 4.16(d) indicates an electron g-factor anisotropy of 13% and 70% for the hole.

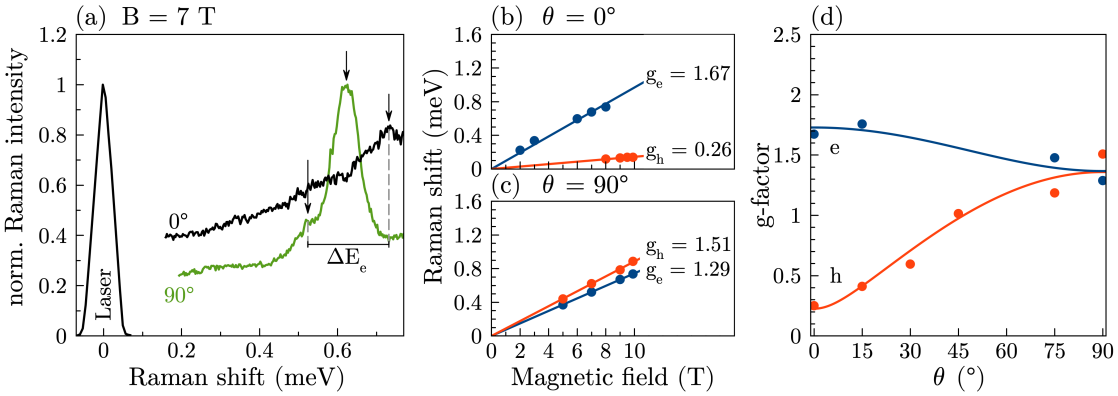

Figure 4.16: (a) SFRS spectra for $(PEA)_2MA_3Pb_4I_{13}$ ($n = 4$) in Faraday ($\theta = 0°$, black) and Voigt geometry ($\theta = 90°$, green) excited with $E_{exc} = 1.839$ eV and $P = 0.6\,W/cm^2$. (b, c) Raman shifts of the SF lines in magnetic field for electron and hole in Faraday (b) and Voigt geometry (c). The fit to linear functions (solid lines) allow to determine the carrier g-factors. (d) Electron and hole g-factor anisotropies with fits using Equation (3.12) (solid lines).

A sample from the same synthesis batch for $n = 4$ is also investigated by Evgeny Zhukov using TRKR. The TRKR signal, excited with $E_{exc} = 1.839$ eV and measured at a temperature of $T = 1.6\,K$, is presented in Figure 4.17. In Figure 4.17(a), the TRKR signal is shown for magnetic field steps of $B_V = 0.25\,T$, up to $B_V = 1\,T$. By extending Equation (4.3) to incorporate the sum of contributions from two carriers, the TRKR signal for $B_V = 0.5\,T$ (see Figure 4.17(b)) can be fitted, revealing two oscillating components (blue and violet curves). The Larmor frequencies of the electron and hole, $\omega_{L,(e,h)}$, along with their spin dephasing times, $T^*_{2,(e,h)}$, can be determined. From the Larmor frequencies, the g-factors of the two resident carriers can be extracted as shown in Figure 4.17(c). Their g-factors yield $g_{e,TRKR} = 1.26$ and $g_{h,TRKR} = 1.50$, which are assigned to the electron and hole, respectively, based on the results obtained from SFRS. In SFRS, the g-factors of the electron and hole are determined to be $g_{e,SFRS} = 1.29$ and $g_{h,SFRS} = 1.51$, respectively, almost identical with TRKR results.

Next, the SFRS spectra for $(PEA)_2MA_{n-1}Pb_nI_{3n+1}$ up to $n = 7$ are measured, the g-factors are determined and assigned to the respective charge carriers. For a detailed analysis of the SFRS spectra for each sample, we refer to the Appendix A2. As illustrated in Figure 4.16 and supported by the data for the other numbers of the inorganic layer thickness in the Appendix (Figure A4 - A8), a consistent trend in the g-factor anisotropy is observed and attributed to the same charge carrier: as the g-factor increases from Faraday to Voigt geometry, it is assumed to correspond to the hole, where a decrease is assigned to the electron. The assignment of electron and hole was determined based on the overall trend of the g-factor values on the excitation energy. The g-factors obtained with the techniques of SFRS and TRKR are summarized in Table 4.2.

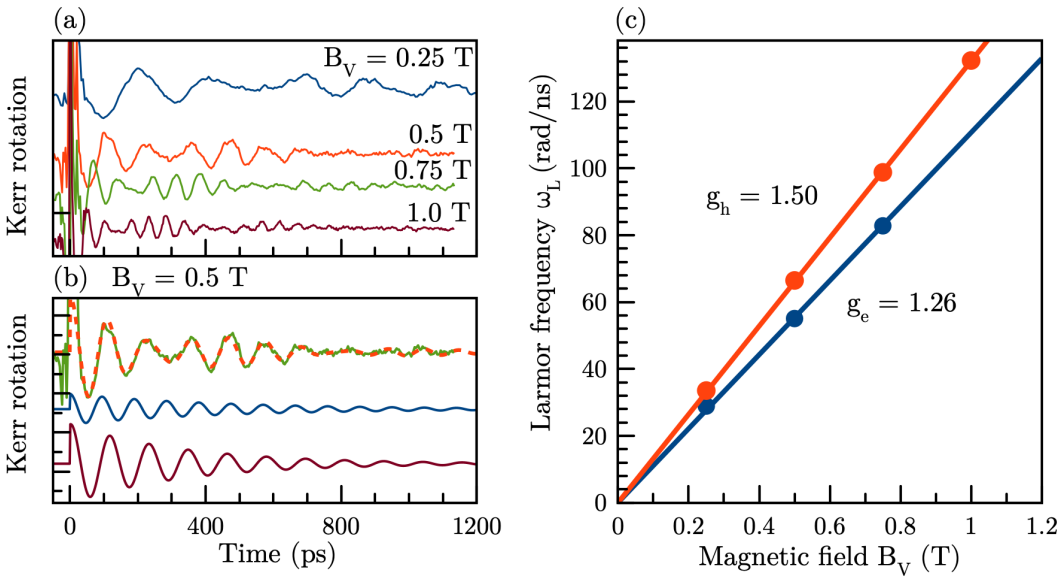

Figure 4.17: Spin dynamics of resident carriers in $(PEA)_2MA_3Pb_4I_{13}$ ($n = 4$) in Voigt geometry B_V at $T = 1.6\,K$, excited with $E_{exc} = 1.839\,eV$. (a) TRKR signals for different magnetic field strengths. Signals are vertically shifted for better visibility. (b) Fit of the TRKR signals at $B_V = 0.5\,T$ with two components (blue and violet) to extract the Larmor frequencies $\omega_{L,(e,h)}$. (c) Dependence of the Larmor frequencies $\omega_{L,(e,h)}$ on the magnetic field, along with the linear fits using Equation (4.4) (solid lines).

Table 4.2: Summary of the g-factors for SFRS and TRKR in $(PEA)_2MA_{n-1}Pb_nI_{3n+1}$.

		SFRS				TRKR	
		Faraday		Voigt		Voigt	
n	E_{exc}	$g_{e,F}$	$g_{h,F}$	$g_{e,V}$	$g_{h,V}$	$g_{e,V}$	$g_{h,V}$
1	2.341 eV	−0.13	2.11	−0.51	2.50		2.45
2	2.132 eV		1.24	0.38	1.91	0.18	1.65
3	1.912 eV	1.21	0.76	0.59	1.62	0.73	1.56
4	1.839 eV	1.67	0.25	1.29	1.51	1.26	1.50
5	1.814 eV			1.15	1.46		1.22
6	1.798 eV			1.19	1.54	1.26	1.41
7	1.789 eV	2.11		1.23			

Figure 4.18 provides a summary of the g-factor values for electrons and holes in the iodine series, determined with SFRS and verified by TRKR (indicated by crosses), displayed in (a) for Faraday and (b) for Voigt geometry. The theory curves represent the universal dependence of the electron and hole g-factors on the band gap energy in bulk lead halide perovskites [62], with additional theoretical curves for perovskites NCs [58] shown for comparison.

For the iodine series, the g-factors of both electron and hole were identified. The electron g-factor, g_e, follows a similar trend to that theoretically observed for $CsPbI_3$ NCs [58]: as the number of inorganic layers decreases (and the excitation energy increases), g_e becomes smaller. In the experiment, we also observe this behavior in Section 5.1 for $CsPbBr_3$ NCs. The good agreement between 2D perovskites and perovskites NCs suggests that the degree of quantum confinement,

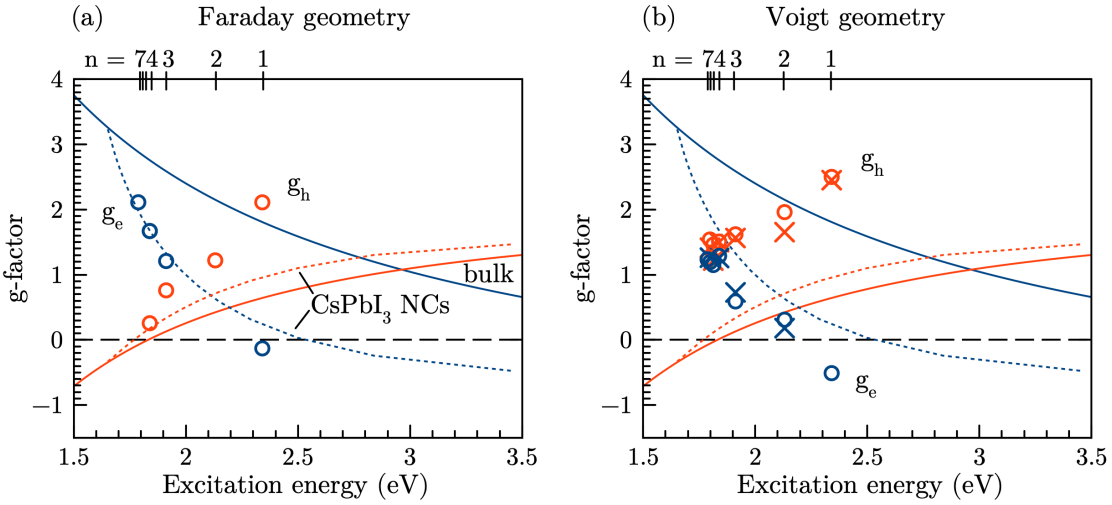

Figure 4.18: Electron and hole g-factors as a function of the excitation energy in 2D $(PEA)_2MA_{n-1}Pb_nI_{3n+1}$. Experimental data are represented by open dots for SFRS and crosses for TRKR. Solid lines indicate the universal dependence of the electron and hole g-factors on the band gap energy in bulk lead halide perovskites, as described in Reference [62], while dashed lines correspond to the same dependence derived for lead halide perovskite NCs [58]. (a) Faraday geometry and (b) Voigt geometry.

rather than the composition of the perovskite material is the dominant factor for modifying the g-factor within the observed energy range. In Faraday geometry (see Figure 4.18(a)), for n ranging between 3 to 7, g_e aligns well with the g-factor dependence observed in $CsPbI_3$ NCs. For smaller n, g_e slightly deviates from this trend. In Voigt geometry (see Figure 4.18(b)), the electron and hole g-factors exhibit the same reversed trends as observed in Faraday geometry. While the trend of the electron g-factor closely follows the theoretical curves for $CsPbI_3$ NCs, the experimental data in Section 5.1 show that the hole g-factors, both in 2D and for NCs, deviate significantly from the expected trend. The general trend of the hole g-factor is similar to that observed for the iodine series: as the number of inorganic layers decreases (and the excitation energy increases), g_h becomes larger. In Faraday geometry, the values of g_h range widely from -1.06 to 2.11, while in Voigt geometry, for $n \geq 3$, the hole g-factor stays nearly constant at 1.47. This observation is supported by TRKR measurements. A constant trend of the g-factor is also observed for the electron in Voigt geometry, where it remains at a value of $g_e = 1.29$ and does not vary with excitation energy.

Next, the electron and hole g-factors determined in the iodine and bromide series are combined into a unified band gap dependence of the g-factors in 2D lead halide perovskites.

4.2.3 Band gap dependence of carrier g-factors in 2D perovskites

As a final step, we provide an overview of the dependence of carrier g-factors on the effective band gap energy in 2D perovskites, including the bromide series $(PEA)_2FA_{n-1}Pb_nBr_{3n+1}$ and the iodine series $(PEA)_2MA_{n-1}Pb_nI_{3n+1}$. The analysis focuses on the experimentally determined g-factors of resident carriers obtained by SFRS, supported by TRKR, and compares their trends with the theoretical models outlined in Section 1.4, highlighting both consistencies and discrepancies. Figure 4.19(a) and (b) show the electron (blue) and hole (red and orange) g-factors measured in Faraday and in Voigt geometry, respectively, as a function of the effective band gap energy. The exciton g-factors measured in the bromide series are not included in these dependences.

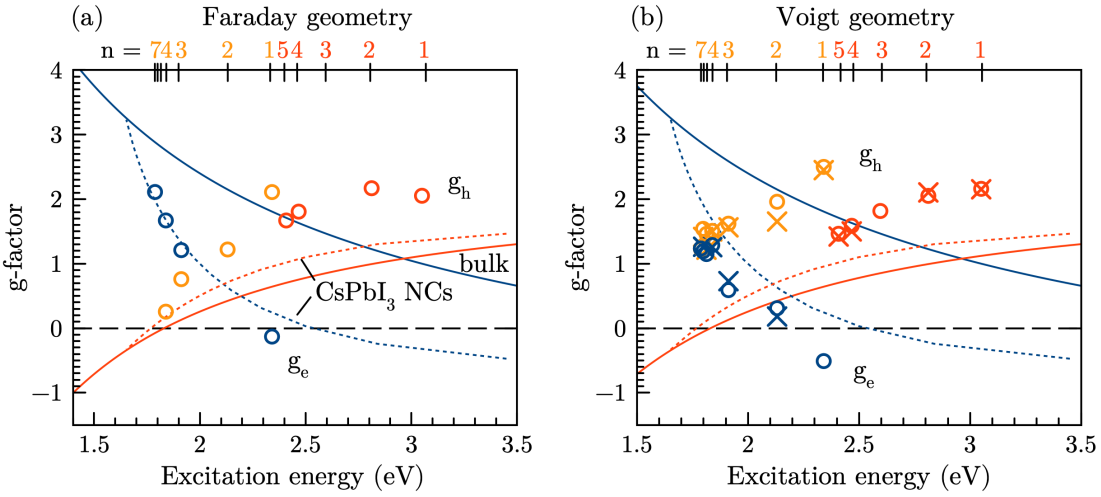

Figure 4.19: Electron and hole g-factors as a function of the excitation energy, combined from Figures 4.15 and 4.18, for 2D RP perovskites. Blue and orange open dots represent electron and hole g-factors from the iodine series, respectively, while red open dots indicate hole g-factors from the bromide series. Experimental data are represented by dots for SFRS and crosses for TRKR. Solid lines indicate the universal dependence of the electron and hole g-factors on the band gap energy in bulk lead halide perovskites, as described in Reference [62], while dashed lines correspond to the same dependence derived for lead halide perovskite NCs [58]. (a) Faraday geometry and (b) Voigt geometry.

In Faraday geometry (see Figure 4.19(a)), the dependence of the electron and hole g-factor on the effective band gap energy indicates a specific trend: the electron g-factor decreases with increasing effective band gap energy, while the hole exhibits an increasing trend. The g-factor values for the electron vary from $g_e = 2.11$ for $n = 7$ ($E_{exc} = 1.788\,eV$) to $g_e = -0.13$ for $n = 1$ ($E_{exc} = 2.341\,eV$), while for the hole the g-factors range between $g_h = -1.06$ to $g_h = 2.11$ across the same energy range. For the bromide series, the hole g-factor increases from $g_h = 1.67$ for $n = 5$ ($E_{exc} = 2.409\,eV$) to $g_h = 2.05$ for $n = 1$ ($E_{exc} = 3.05\,eV$). The transition from the iodine to the bromide series at an energy of approximately $E_{exc} = 2.34\,eV$ is relatively smooth.

In Voigt geometry (see Figure 4.19(b)), a similar trend is observed, where the electron and hole g-factors exhibit opposing trends on the effective band gap energy. In this geometry, the electron g-factors decreases from 1.23 to −0.51, while the hole g-factor increases from 1.54 to 2.5 as the effective band gap energy increases. For the bromide series, the hole g-factor increases from $g_h = 1.47$ for $n = 5$ ($E_{exc} = 2.409\,eV$) to $g_h = 2.15$ for $n = 1$ ($E_{exc} = 3.05\,eV$). In contrast to Faraday geometry, the difference in the hole g-factor when changing from the iodine to the bromide series at $E_{exc} = 2.34\,eV$ is discontinuous in Voigt geometry, with a jump of the g-factor

of 1.04. This observation suggests that the halide content especially impacts the in-plane g-factor in 2D perovskites. The observed trends underline the anisotropic nature of carrier g-factors in 2D perovskites, which strongly depend on both the band gap energy and the experimental geometry.

The measured dependences of the electron and hole g-factors are compared with theoretically calculated g-factors for bulk lead halide perovskites (solid lines) [62] and perovskite NCs (dashed lines) [58] as detailed in Section 1.4. Note that these theoretical dependences are plotted against the effective band gap energy, i.e., the energy between the first quantum confined levels of the electron and hole, while the experimental data is shown for the exciton resonance energy, corresponding to the laser photon energy. While the general trends qualitatively align, notable differences in the g-factor values are observed. In particular, the increase in quantum confinement strength has a more pronounced effect on the hole g-factor than theoretically predicted, resulting in experimental hole g-factors that exceed the predicted values by almost a factor of two. Similar behavior has been recently observed in $CsPbI_3$ NCs [161], as well as in $CsPbBr_3$ and $CsPb(Cl, Br)_3$ NCs [51], suggesting that this effect may be a general characteristic of lower-dimensional lead halide perovskites. In Reference [161], the strong renormalization of the hole g-factor is attributed to the mixing of the upper valence band (VB) with lower halide bands. As tight-binding calculations are limited to describe the upper valence band and three lower conduction bands (CBs), the influence of mixing with lower VBs is not taken into account. This results in an underestimation of this contribution, potentially explaining the discrepancy in the hole g-factors.

For the electron g-factor in Faraday geometry, the experimental data are limited, as the electron g-factor is observed only in the iodine series, not in the bromide series. Nevertheless, the electron g-factors cover an energy range of roughly 0.6 meV, and the expected trend aligns well with theoretical predictions for $CsPbI_3$ NCs with only small deviations observed for stronger quantum confinement. In Voigt geometry, a similar trend is observed, as seen in $CsPbI_3$ NCs. The good agreement between 2D perovskites and perovskites NCs suggests that the degree of quantum confinement, rather than the composition of the perovskite material, is the dominant factor for modifying the g-factor within the observed energy range. The smaller deviations may be attributed to surface effects, as the surface-to-volume ratio increases with decreasing layers of lead halide octahedra. In particular, surfaces containing organic spacers such as PEA may have a significant impact on the spin properties of the carriers and excitons, as electrons could become localized at the surface.

The results highlight the complex dependence of carrier g-factors on the effective band gap energy in 2D perovskites, revealing distinct trends for electrons and holes that also vary with the experimental geometry. These findings emphasize the need to refine theoretical models to better describe the unique properties of 2D perovskite systems and account for the strong renormalization of the hole g-factor. A deeper understanding of the carrier g-factor dependences in 2D perovskites is essential for optimizing their performance in spintronic and optoelectronic applications.

4.3 Conclusion

This chapter presented the investigations of SFRS on 2D RP type perovskites $(PEA)_2(FA, MA)_{n-1}Pb_n(Br, I)_{3n+1}$. In $(PEA)_2PbI_4$ with $n = 1$, we observed SFs of resident electrons, holes, and their combinations in different magnetic field geometries. The g-factor anisotropies of both the electron and the hole highlight the reduced symmetry of the band structure in 2D perovskites. However, their sum corresponding to the bright exciton remains isotropic. The observation of the hyperfine interaction through DNP revealed the negative sign of the electron g-factor, while the sign of the hole g-factor was determined to be positive based on the universal dependence of the electron and hole g-factors in bulk lead halide perovskites.

To gain a comprehensive understanding of the impact of reduced dimensionality on the g-factor in 2D RP perovskite $(PEA)_2(FA, MA)_{n-1}Pb_n(Br, I)_{3n+1}$, the g-factors of resident electrons and holes were systematically determined for the iodine and bromide series. By combining the g-factors from both series, the electron and hole g-factors were traced across a large energy range of approximately 1.3 eV, supported by TRKR measurements. While the general trend of the g-factors with respect to the effective band gap energy aligns qualitatively with models for bulk lead halide perovskites, the hole g-factor exceeds predictions for bulk by nearly a factor of two. These findings highlight the need to refine theoretical models to better describe the unique properties of 2D perovskites and understand the strong renormalization of the hole g-factor. This also opens up the possibility of tuning the spin properties of lead halide perovskites through quantum confinement, as the band gap energy significantly shifts from approximately 1.63 eV for bulk $MAPbI_3$ to 2.34 eV for two-dimensional $(PEA)_2PbI_4$ with $n = 1$.

It should be noted that, compared with our publication [15], the assignment of the electron and hole g-factors has been revised, taking into account the full dependence of g-factors on the effective band gap energy and the recent finding that the hole g-factor in low dimensional systems can drastically change with stronger quantum confinement.

Resonant Raman spectroscopy of $CsPbBr_3$ and $CsPbI_3$ perovskite nanocrystals

5

In Section 4, the impact of dimensionality through quantum confinement on the g-factor was explored for 2D lead halide perovskites. In this section, the focus shifts to 0D $CsPbBr_3$ and $CsPbI_3$ perovskite nanocrystal (NC) of varying sizes. Larger $CsPbBr_3$ NCs, dispersed in solution and drop-cast onto a glass substrate, exhibit sizes of 8–11 nm, whereas smaller $CsPbI_3$ NCs, embedded in a glass matrix, range between 4–13 nm. The larger $CsPbBr_3$ are investigated with the technique of spin-flip Raman scattering (SFRS) to evaluate the impact of quantum confinement on the carrier g-factor in comparison to bulk lead halide perovskites. Therefore, the g-factors of resident electrons and holes are determined as a function of the NC size. Resonant Raman spectra reveal scattering from both acoustic and optical phonons in $CsPbBr_3$ and $CsPbI_3$ NCs. This technique offers a direct measurement of the acoustic and optical phonon energies. Furthermore, we observe that the Raman shift of these confined acoustic phonons depends on the NC size. Finally, we analyze the size dependence of the confined acoustic phonons resonances for small $CsPbI_3$ and large $CsPbBr_3$ NCs through their interaction with photogenerated excitons. With density functional theory (DFT) calculations, the resonant Raman spectra can be simulated, offering an additional approach for characterizing NCs in terms of their shape, structural phase, and size.

The results of the DFT calculations presented in Section 5.2 are obtained by Mikhail O. Nestoklon within our research group at TU Dortmund University.

5.1 Spin-flip Raman spectroscopy of $CsPbBr_3$ nanocrystals

In this section, we first analyze the optical properties of $CsPbBr_3$ NCs. Next, the technique of SFRS is applied to determine the carrier g-factors and their anisotropy. Finally, we investigate the dependence of the electron and hole g-factors on the NC size.

5.1.1 Optical properties of $CsPbBr_3$ nanocrystals

First, we begin with the optical characterization of a set of $CsPbBr_3$ NCs samples, consisting of three samples with NCs sizes ranging from 8 to 11 nm. The samples are labeled as #1 for a NC size of 11 nm, #2 for 10 nm, and #3 for 8 nm. The NC sizes were determined through absorption measurements performed by the synthesis group at ETH Zürich. In Section 5.2, a complementary experimental approach for determining the size, shape, and structural phase of a NC, based on optically-active confined acoustic phonon modes, will be introduced.

Figure 5.1 shows the photoluminescence (PL) and absorption spectra at a temperature of $T = 1.6\,\mathrm{K}$ for samples #1–#3. In Table 5.1, the parameters of the PL and absorption spectra for all three samples, obtained from Figure 5.1, are summarized.

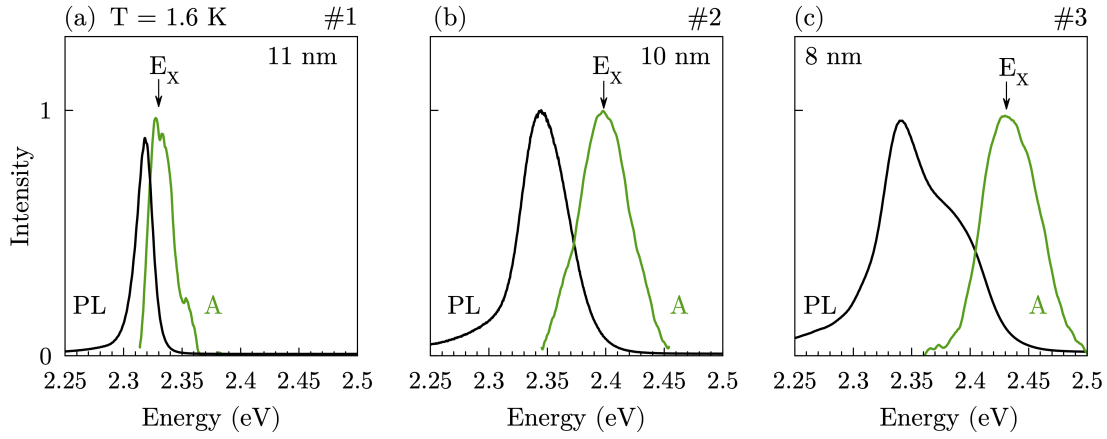

Figure 5.1: PL (black) and absorption A (green) spectra for $CsPbBr_3$ NCs of varying sizes at $T = 1.6\,\mathrm{K}$. The sample numbers (#) correspond to decreasing NC size, presented in the order from largest to smallest: #1 for 11 nm, #2 for 10 nm, and #3 for 8 nm. Power densities used for PL measurements are 1 $\mathrm{W/cm^2}$ for sample #1, 4 $\mathrm{W/cm^2}$ for sample #2, and 2 $\mathrm{W/cm^2}$ for sample #3. Exciton resonances E_X are indicated by vertical arrows.

The PL emission maxima occur at energies of $E_{\#1} = 2.318\,\mathrm{eV}$ for sample #1, $E_{\#2} = 2.344\,\mathrm{eV}$ for sample #2, $E = 2.342\,\mathrm{eV}$, and $E_{\#3} = 2.388\,\mathrm{eV}$ for sample #3. In Figure 5.1(c) for sample #3, the PL exhibits an asymmetric lineshape, with the lower energy peak corresponding to larger NCs, which have a PL maximum nearly identical to that observed in Figure 5.1(b). However, our focus is on the higher energy side of the PL, near the absorption maximum. The variation in the spectral positions of the PL peaks for the $CsPbBr_3$ NCs arises from differences in the quantum confinement energy of the carriers [51]. The significant size dispersion of NCs within each sample results in pronounced inhomogeneous broadening in their optical properties. Single $CsPbBr_3$ NCs at a temperature of $T = 6\,\mathrm{K}$ typically exhibit a narrow PL spectral width of 1 meV due to the absence of inhomogeneous broadening [176]. In contrast, the PL lines in the NC ensemble show a full width at half maximum (FWHM) ranging from 20 to 60 meV, while the absorption maxima exhibit a FWHM of 20 to 55 meV. Based on the FWHM of the PL and absorption spectra, sample #1, with the largest NC sizes, appears to be the most homogeneous of the three investigated samples. The NC ensemble provides insights into the average spin properties and their dependence on different NC sizes due to the inhomogeneities within the sample [66]. By using a narrow single-mode laser as an excitation source in the SFRS experiments, we are able to selectively excite NCs with different mean sizes by scanning the central energy of the laser through the inhomogeneously broadened resonance of the ensemble.

Table 5.1: Summary of the parameters of the PL and absorption spectra of samples #1–#3.

sample	NC size	E_{PL}	$FWHM_{PL}$	E_A	$FWHM_A$
#1	11 nm	2.318 eV	20 meV	2.332 eV	20 meV
#2	10 nm	2.344 eV	50 meV	2.398 eV	50 meV
#3	8 nm	2.388 eV	60 meV	2.435 eV	55 meV

5.1.2 Carrier g-factors of $CsPbBr_3$ nanocrystals

To investigate the role of quantum confinement on the carrier g-factors in lead halide perovskite NCs, we begin with SFRS measurements on sample #1, tuning the laser photon energy to the exciton resonance at $E_{exc} = 2.323\,eV$. Figure 5.2(a) presents the SFRS spectrum for Faraday geometry in a magnetic field of $B_F = 7\,T$, measured on Stokes side for cross-circular polarization $\sigma^+\sigma^-$.

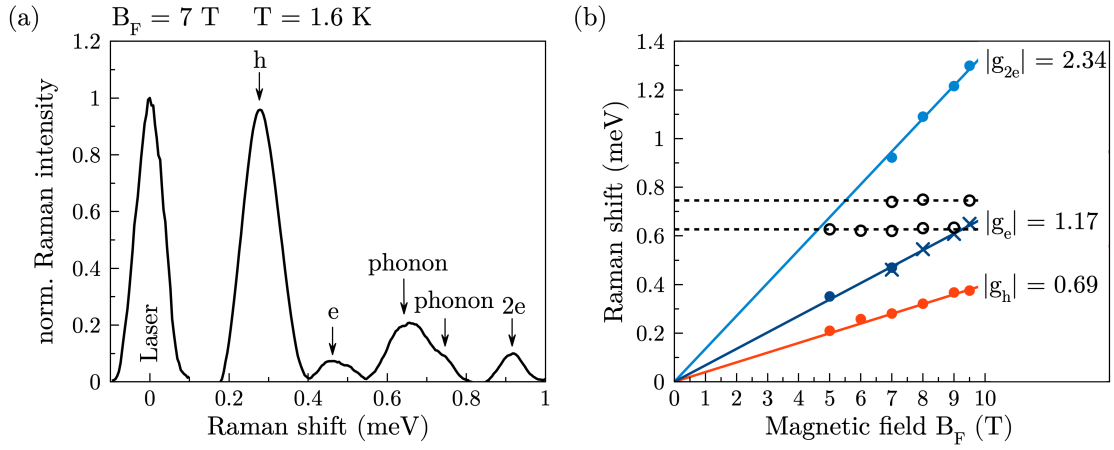

Figure 5.2: (a) Normalized SFRS spectra of $CsPbBr_3$ NCs sample #1 (11 nm) in Faraday geometry at $B_F = 7\,T$, measured with an excitation energy of $E_{exc} = 2.323\,eV$ in cross-circular polarization $\sigma^+\sigma^-$ and a power density of $5\,W/cm^2$. Peaks are indicated by vertical arrows. (b) Magnetic field dependence of the Raman shifts. Closed dots represent spin-flips with their linear fits (solid lines) based on the Zeeman equation, while crosses indicate calculated Raman shifts. Open dots and dashed lines correspond to phonons.

In the SFRS spectrum in Figure 5.2(a), five peaks marked by vertical arrows can be observed. From the magnetic field dependence presented in Figure 5.2(b), we can deduce the origin of the different peaks. The peaks at $E_h = 0.28\,meV$, $E_e = 0.46\,meV$ and $E_{2e} = 0.92\,meV$ exhibit a linear dependence on the magnetic field, confirming their origin as spin-flip (SF) transitions and aligning with observations for 3D and 2D lead halide perovskites discussed in Chapters 3 and 4. Their corresponding g-factors, calculated from the Zeeman equation (Equation 2.2), are $|g_h| = 0.69$, $|g_e| = 1.17$, and $|g_{2e}| = 2.34$, respectively. The signs of g_e and g_h cannot be directly determined from a single SFRS spectrum but they are positive in bulk $CsPbBr_3$ [62] and are theoretically expected to remain positive for sufficiently large NCs [51, 58]. In contrast, the peak at $E_{phonon} = 0.62\,meV$ and its shoulder at $E_{phonon} = 0.74\,meV$ remain unaffected by the magnetic field, indicating that they originate from a different inelastic scattering process. Since $CsPbBr_3$ crystalizes in the orthorhombic structural phase even at room temperature [93], one possibility is that these peaks arise from the bright exciton fine structure splitting, as introduced in Section 1.1.2. In $CsPbBr_3$ NCs, the exciton fine structure splitting caused by the anisotropic exchange interaction within the exciton has been observed to be in the order of 1 meV [177]. If the peaks originate from the exciton fine structure, the slope of the linear fits would change from zero to following the Zeeman equation at a magnetic field of approximately 6 T. However, as shown in Figure 5.2(b), measurements up to 10 T reveal that the peaks remain independent of the magnetic field across the entire range. Therefore, we attribute these peaks to phonons instead. A detailed discussion on the acoustic phonons and their properties can be found in Section 5.2.

At this point, we will focus on the peaks in the SFRS spectrum originating from SFs and determine the corresponding g-factors. In Reference [48], magnetic field measurements are extended to lower fields up to 1 T, demonstrating that the absence of an offset at zero magnetic field indicates the presence of resident carriers in $CsPbBr_3$ NCs, rather than carriers bound within an exciton. In contrast, for excitons, an offset in the Raman shift can arise due to the exchange interaction between the electron and hole. Resident carriers in NCs can originate from long-lived photocharging, when some NCs in the ensemble become charged with electrons, others with holes, while the rest remain neutral [57]. In Reference [58], the g-factors of both electrons and holes in lead halide perovskite NCs have been investigated. By comparing the measured g-factors of $g_h = 0.69$ and $g_e = 1.17$ with the values provided in Reference [58] ($g_h = 0.63$ and $g_e = 1.80$) for the same excitation energy, we can attribute the observed g-factors to the hole and electron, respectively. While the hole g-factor is in good agreement, the electron g-factor exhibits a discrepancy. Additionally, a third SF at $E_{2e} = 0.922$ meV with $g_{2e} = 2.34$, exactly twice the g-factor of the electron, can be identified. By tuning the excitation energy of the laser, the dependence of the spin properties as a function of the NC size can be studied. The result of this measurement is shown in Figure 5.3, where the electron and hole g-factors, represented by blue and red dots, respectively, vary with the excitation energy in a range of 30 meV.

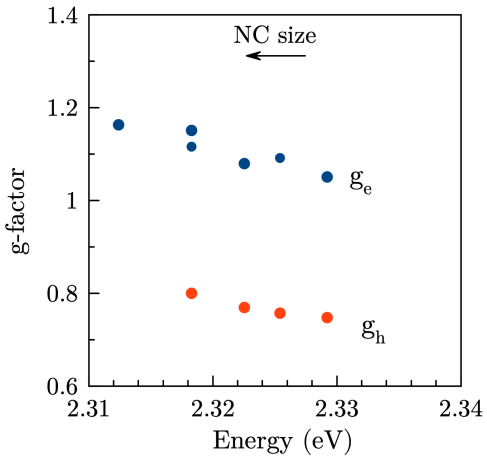

Figure 5.3: Electron and hole g-factors as a function of the NC size for sample #1. Blue and red points represent g-factors of electron and hole, respectively.

Interestingly, in sample #1, the hole g-factor decreases from 0.8 to 0.74, while the electron g-factor changes from 1.16 to 1.05 as the excitation energy increases, corresponding to a decrease in NC size. This observation directly demonstrates that quantum confinement has a significant impact on the g-factors of carriers in $CsPbBr_3$ NCs. To extend this analysis over a broader energy range and NC sizes, the g-factors of electrons and holes are further investigated in samples #2 and #3 in the Section 5.1.4.

5.1.3 g-factor anisotropy of carriers in $CsPbBr_3$ nanocrystals

The orientation of the magnetic field is not expected to significantly affect the g-factors of the NCs, as the c-axes are randomly oriented, resulting in the measurement of an effective averaged g-factor value. However, we verify this assumption by measuring SFRS in both Faraday and Voigt geometry. Figure 5.4(a) shows the SFRS spectrum in Voigt geometry at a magnetic field of $B_V = 7\,T$.

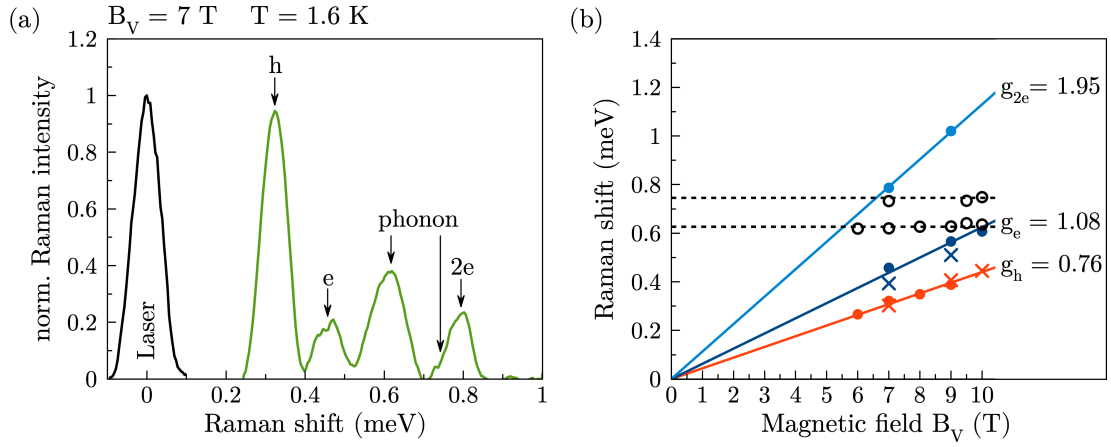

Figure 5.4: (a) Normalized SFRS spectra of $CsPbBr_3$ NCs sample #1 (11 nm) measured in Voigt geometry at $B_V = 7\,T$ using cross-linear polarization HV and excitation power density of $P = 6\,W/cm^2$. Peaks are marked by vertical arrows. (b) Magnetic field dependences of the peaks: filled dots denote SFs, with their linear fits (solid lines) based on the Zeeman equation, while crosses represent calculated Raman shifts. Open dots and dashed lines correspond to phonons.

Four distinct peaks in the SFRS spectra in Figure 5.4(a) are identified at Raman shifts of $E_h = 0.32\,meV$, $E_e = 0.46\,meV$, $E_{phonon} = 0.62\,meV$ and $E_{2e} = 0.79\,meV$, with a small shoulder at $E_{phonon} = 0.73\,meV$. Since the phonon Raman shifts are independent of the magnetic field, their Raman shifts remain unaffected by the field direction and are consistent with those observed in Faraday geometry. In contrast, the other three peaks exhibit a linear shift with the magnetic field (see Figure 5.4(b)), yielding calculated g-factors of $g_h = 0.76$, $g_e = 1.08$ and $g_{2e} = 1.95$ for the hole, electron, and double electron, respectively. Table 5.2 summarizes the g-factors for sample #1, along with the g-factor values determined in Section 5.1.4 for samples #2 and #3, in both Faraday and Voigt geometry.

To simplify the comparison of the SFRS spectra between Faraday and Voigt geometry, both spectra are shown in the same figure, Figure 5.5(a), with Raman shift differences for the hole, electron, and double electron labeled as ΔE. Additional measurements at intermediate angles between Faraday and Voigt geometry, taken in $\theta = 15°$ steps, are presented in Figure 5.5(b) to provide a more precise analysis of the g-factor anisotropy.

In Figure 5.5(b), only a minor g-factor anisotropy for the electron and hole is observed, which can be attributed to the random orientation of the NC c-axes, as already mentioned above. Consequently, no pronounced g-factor anisotropy is expected, as the determined g-factors represent an average over the various c-axis orientations. However, a small anisotropy may arise if the ensemble is not completely disoriented, for instance, when more NCs align along a specific direction, which might result from non-isotropic conditions during sample synthesis. According to Equation 3.13, the g-factor anisotropy is 5% for holes and 4% for electrons.

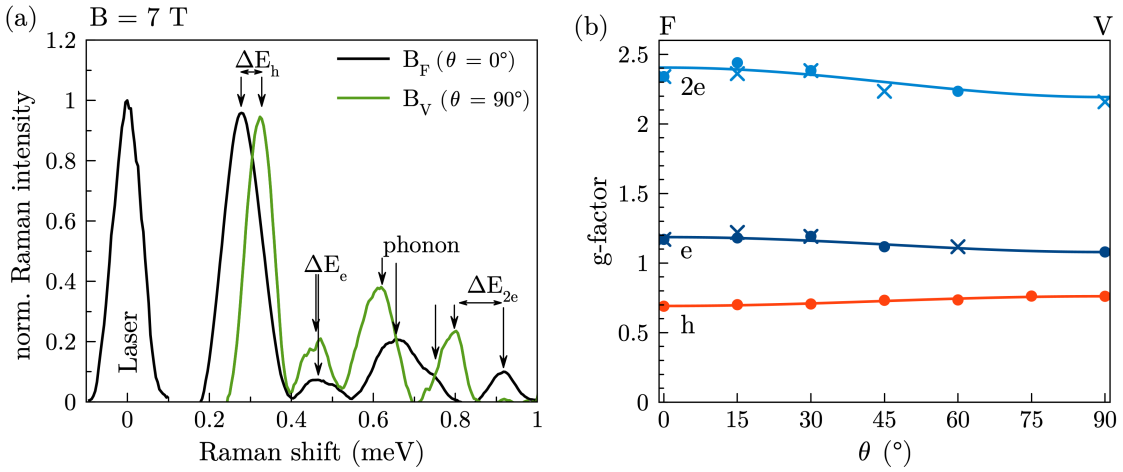

Figure 5.5: (a) Normalized SFRS spectra for $CsPbBr_3$ NCs sample #1 measured in Faraday geometry (B_F, $\theta = 0°$, black) and Voigt geometry (B_V, $\theta = 90°$, green) at $B = 7$ T. The excitation energy is $E_{exc} = 2.323$ eV, with power densities of $P = 5\,W/cm^2$ and $P = 6\,W/cm^2$, respectively. (b) g-factor anisotropy for the electron, hole, and double electron, where crosses represent the calculated g-factor values, and lines correspond to fits with Equation 3.12.

5.1.4 Carrier g-factor dependence on the nanocrystal size

The analysis of the SFRS spectra and the determination of g-factors for samples #2 and #3 follow the same procedure as for sample #1. The results for sample #2 are displayed in Figure 5.6, while those for sample #3 are presented in Figure 5.7. In panels (a) and (c), the SFRS spectra in Faraday and Voigt geometries are shown, respectively, whereas panels (b) and (d) depict the magnetic field dependences for each geometry. Panel (e) presents the g-factor anisotropies.

Sample #2 is resonantly excited with a laser photon energy of $E_{exc} = 2.365$ eV, enabling the determination of the g-factors for the medium-sized NCs in this sample batch. In contrast to sample #1, six distinct peaks are observed in Faraday geometry at $B_F = 10$ T (see Figure 5.6(a)). The SF transitions of the hole, electron, and their combination are identified at Raman shifts of $E_h = 0.44$ meV, $E_e = 0.63$ meV, and $E_{e+h} = 1.08$ meV, corresponding to g-factors of $g_h = 0.75$, $g_e = 1.08$, and $g_{e+h} = 1.87$, respectively. Additionally, the SF of two electrons is observed at $E_{2e} = 1.24$ meV, yielding $g_{2e} = 2.13$. Two phonon lines are also visible at Raman shifts of $E_{phonon} = 0.310$ meV and $E_{phonon} = 0.82$ meV. In Voigt geometry at $B_V = 10$ T (see Figure 5.6(c)), the SFRS spectrum similarly reveals the SFs of hole, electron, and their combination, along with the phonon lines at nearly the same Raman shifts. However, the SF of two electrons cannot be observed. The determined g-factors in Voigt geometry are $g_h = 0.92$, $g_e = 1.20$, and $g_{e+h} = 2.06$. The g-factor anisotropy, as shown in Figure 5.6(e), exhibits only a small dependence of the g-factor on the angle to the magnetic field, with a 10% variation for holes and a 5% variation for electrons. This small anisotropy aligns with our expectations for the subensemble of NCs.

Finally, we examine sample #3 with the smallest NCs. This sample is excited near its exciton resonance at $E_{exc} = 2.430$ eV, and the results are presented in Figure 5.7. In Figure 5.7(a) and (c), the SFRS spectra for Faraday and Voigt geometries at $B = 8$ T are presented. In Faraday geometry (see Figure 5.7(a)), Raman shifts corresponding to the electron and its combination with the hole are identified at $E_e = 0.24$ meV and $E_{e+h} = 0.74$ meV, respectively. These shifts correspond to calculated g-factors of $g_e = 0.53$ and $g_{e+h} = 1.60$, as shown in Figure 5.7(b). However, the hole SF is absent in this spectrum, as can be seen in the magnetic field dependence shown in Figure 5.7(b).

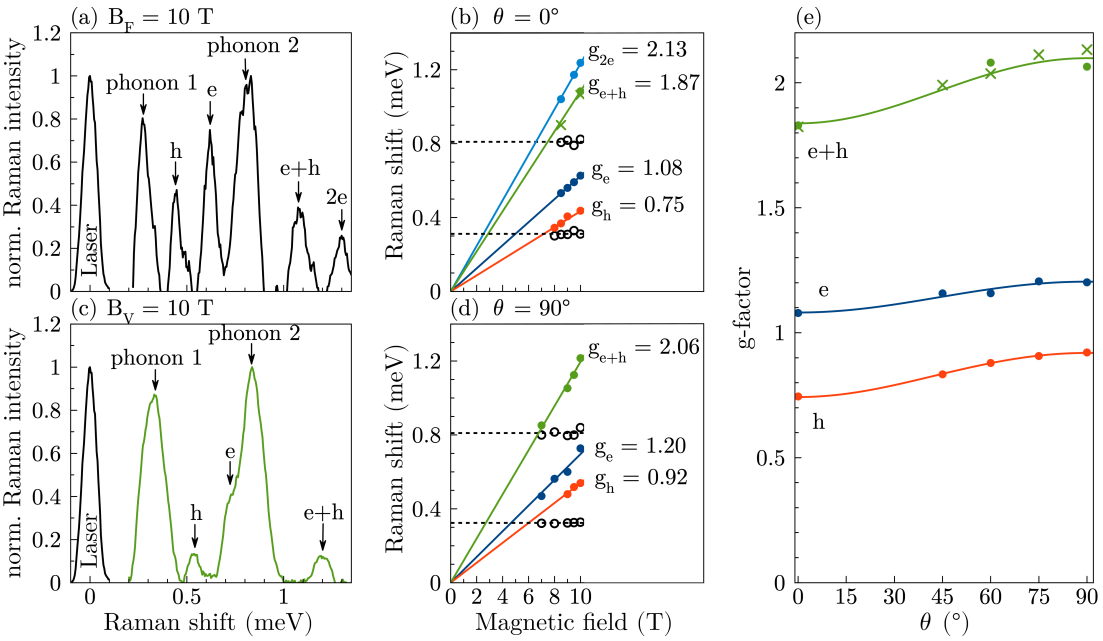

Figure 5.6: Normalized SFRS spectra of $CsPbBr_3$ NCs sample #2 (10 nm), excited at E_{exc} = 2.365 eV for B = 10 T: (a) Faraday geometry with cross-circular polarization ($\sigma^+\sigma^-$) and P = 5 W/cm^2, and (c) Voigt geometry with co-linear polarization (HH) and P = 3 W/cm^2. SFs and phonons are marked with vertical arrows, and their magnetic field dependencies are shown in panels (b) and (d). Open dots and dashed lines represent the phonon Raman shifts. Crosses indicate calculated Raman shifts and g-factors. (e) g-factor anisotropy for the electron, hole, and their combination from Faraday ($\theta = 0°$) to Voigt geometry ($\theta = 90°$), lines are fits with Equation 3.12.

From the linear fit of the hole's magnetic field dependence, a Raman shift of E_h = 0.53 meV at B_F = 8 T for g_h = 1.26 would be expected. At this energy, however, the hole SF overlaps with the phonon signal and the strong phonon line at E_{phonon} = 0.49 meV hides the hole SF signal. Due to the small g-factor anisotropy, the hole SF appears as a small shoulder near the phonon peak in Voigt geometry, as shown in Figure 5.7(c) for B_V = 8 T at a Raman shift of E_h = 0.53 meV. In Voigt geometry, the g-factors are determined to be g_e = 0.70, g_h = 1.07, and g_{e+h} = 1.77. Similar to the other $CsPbBr_3$ samples with varying NC sizes, a small g-factor anisotropy for sample #3 is observed, as illustrated in Figure 5.7(e). From Equation 3.13, the calculated g-factor anisotropy is 11% for holes and 5% for electrons. For the three NC samples, the electron g-factor anisotropy is approximately the same at 5%. However, for holes, the anisotropy is 5% in sample #1 and increases up to 11% for smaller NCs sizes.

The g-factors of sample #1 to #3 in both Faraday and Voigt geometry are summarized in Table 5.2 and presented in Figure 5.8.

As observed for the individual samples, the direction of the magnetic field has a minimal impact on the measured g-factor value and its anisotropy due to the varying orientations of the c-axes within the NC ensemble. Therefore, the dependence of the g-factor on excitation energy and NC size will be discussed in detail only for Faraday geometry. For all three samples, a consistent trend is observed in Faraday geometry, aligning with the universal dependence reported for bulk lead halide perovskites, as described in Reference [62] and Section 1.4. Specifically, the electron g-factor decreases with increasing excitation energy, which corresponds to smaller NCs sizes, while the hole g-factor increases with excitation energy or decreasing NC size. The hole

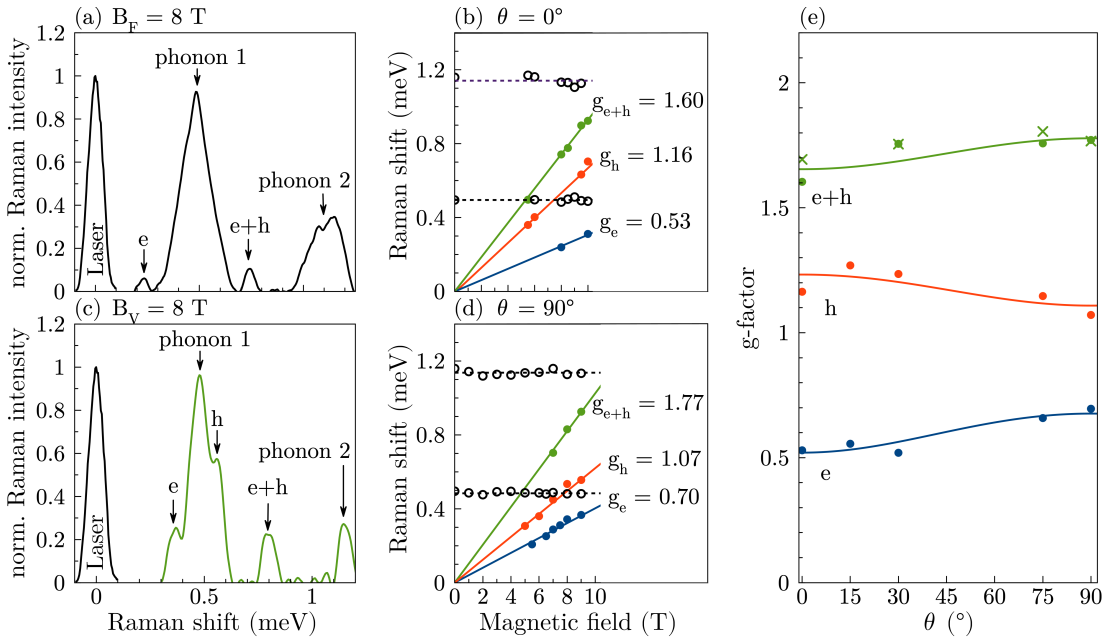

Figure 5.7: Normalized SFRS spectra of $CsPbBr_3$ NCs sample #3 (8 nm), excited at E_{exc} = 2.430 eV for B = 8 T: (a) Faraday geometry with co-circular polarization ($\sigma^-\sigma^-$) and P = 6 W/cm^2, and (c) Voigt geometry with cross-linear polarization (HV) and P = 4 W/cm^2. SFs and phonons are marked with vertical arrows, and their magnetic field dependencies are shown in panels (b) and (d). Open dots and dashed lines represent the phonon Raman shifts. (e) g-factor anisotropy for the electron, hole, and their combination from Faraday ($\theta = 0°$) to Voigt geometry ($\theta = 90°$), lines are fits with Equation 3.12.

g-factor values for $CsPbBr_3$ NCs are relatively close to the bulk values as given in Reference [62]. For sample #1, the hole g-factor is determined to be $g_h = 0.69$, compared to a bulk value of $g_{h,b} = 0.62$. For sample #2, $g_h = 0.74$ is observed, which is only slightly higher than the bulk value of $g_{h,b} = 0.66$. In contrast to sample #1 and #2, the hole g-factor determined in sample #3, which has the smallest NC size among the three investigated $CsPbBr_3$ NC samples, exhibits a significant deviation from the bulk g-factor value. A similar trend for the hole g-factor has been observed in $CsPbBr_3$ NCs embedded in a glass matrix [51]. The dependence of the hole g-factor on the NC size from this publication is shown as crosses in Figure 5.8. By comparing the measured hole g-factor value of $g_h = 1.16$ in sample #3 with the data from Reference [51] at the same energy of $E = 2.43$ eV, we find a good agreement with their hole g-factor of $g_h = 1.12$. Therefore, the dependence of the hole g-factor on the excitation energy roughly follows the trend observed in Reference [51], at least for the small energy range of approximately 100 meV

Table 5.2: Summary of the g-factors for the three $CsPbBr_3$ NCs samples.

	Faraday			Voigt		
g-factor	#1 (11 nm)	#2 (10 nm)	#3 (8 nm)	#1 (11 nm)	#2 (10 nm)	#3 (8 nm)
h	0.69	0.75	1.16	0.76	0.92	1.07
e	1.17	1.08	0.53	1.08	1.20	0.70
e+h		1.87	1.60		2.06	1.77
2e	2.34	2.13		1.95		

covered by samples #1–#3. The calculations presented in Reference [58] are shown as dashed lines in Figure 5.8, with the electron g-factors represented in blue and the hole g-factors in red, as described in detail in Section 1.4. Note that these dependences are plotted as a function of the effective band gap energy, i.e., the energy between the first quantum confined levels of the electron and hole. The measured dependence of the hole g-factors does not align well with the theoretical predictions. However, our experimental data show a good agreement with the data measured by time-resolved Kerr rotation (TRKR) on $CsPbBr_3$ NCs in Reference [51].

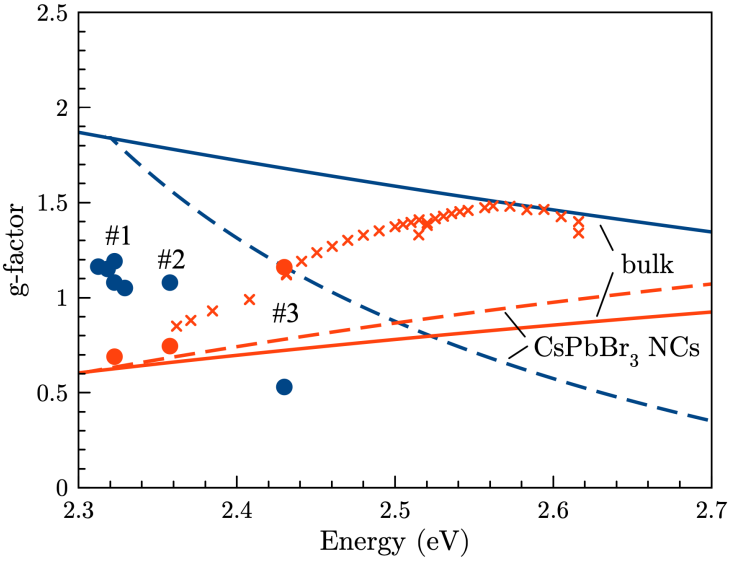

Figure 5.8: Dependence of the electron and hole g-factor on the excitation energy for samples #1–#3 represented by dots. Crosses indicate the data from Reference [51] for $CsPbBr_3$ NCs. Solid lines are fits based on the universal dependence of the electron and hole g-factor on the band gap energy in bulk lead halide perovskites [62], while the dashed lines are derived from the same dependence in lead halide perovskite NCs [58].

In Reference [51], the strong effect of the NC size on the hole g-factor and the discrepancy with the bulk $CsPbBr_3$ value is most likely attributed to the mixing of the upper valence band (VB) with halide bands that lie approximately 1.5 eV below the top of the VB. Model calculations based on the tight-binding approach, which consider nearest-neighbor interactions, can accurately describe the upper VB and the three lowest conduction bands (CBs). However, accurately modeling the dispersion of the lower VBs, which are formed by the p-orbitals of halogen atoms, is challenging with the nearest-neighbor model, as second-neighbor interactions also need to be included [178, 179]. These effects are not included in the theoretical calculations presented in Reference [58]. Incorporating the mixing of the lower VBs could lead to a more accurate description of the renormalization of the hole g-factor. Therefore, extending the theory to include this effect may be important for a more accurate reproduction of the measured hole g-factor dependence in $CsPbBr_3$ NCs. [161]

The trend of g_e for samples #1 to #3 aligns with the universal dependence of the electron g-factor observed in bulk lead halide perovskites. However, the absolute values of g_e, ranging from $g_{e,NC} = 0.53–1.17$, deviate significantly from those reported for bulk lead halide perovskites, which range between $g_{e,b} = 1.84–1.77$. This trend can be qualitatively described by the theory proposed for $CsPbBr_3$ NCs in Reference [58], represented by the blue dashed line in Figure 5.8.

However, our electron g-factors measured with SFRS show significant deviations, which may be attributed to several factors: (1) The $CsPbBr_3$ NCs investigated in this thesis are not embedded in a glass matrix but instead drop-cast onto a glass substrate and stabilized by organic ligands (see Section 2.2.3 for details). If the electron is localized at the surface, this could result in deviations from the electron g-factor values typically observed for carriers confined within a NC. (2) The theoretical calculations are based on NCs with cubic symmetry, while $CsPbBr_3$ adopts an orthorhombic structural phase at low temperatures. This structural difference may influence the spin and electronic properties. (3) The surfaces of the NCs may significantly impact the spin properties of carriers and excitons localized within them. These surface effects are not included in the theoretical model, potentially contributing further to the observed discrepancies. An alternative interpretation might suggest that the observed g-factors correspond to the exciton rather than to the electron. Interestingly, a similar behavior is reported in perovskite NCs in Reference [161], where the exciton g-factor remained approximately constant with respect to the effective band gap energy despite the influence of quantum confinement, surface effects, and the large exciton binding energy in NCs. Therefore, the observed g-factor values of $g_{e,NC} = 0.53-1.17$ must be attributed to the electrons. Although a complete theoretical understanding of the observed size-dependent spin properties of lead halide perovskite NCs has not been achieved yet, the experimental results presented in this chapter demonstrate that the g-factors of carriers are highly sensitive to the effect of quantum confinement.

As mentioned earlier, the SFRS spectra reveal numerous lines with Raman shifts that remain independent of the magnetic field. We attribute these lines to Raman scattering on optically-active acoustic phonons confined within the NCs. The phonon properties will be explored and discussed in detail in Chapter 5.2 for both $CsPbBr_3$ and $CsPbI_3$ NCs.

5.2 Optically-active confined acoustic phonons

This chapter aims to provide insights into the phonon properties and their dependence on the NC size by exploring two compositions of NCs, $CsPbBr_3$ and $CsPbI_3$, through the technique of resonant Raman scattering. Besides the difference between the halides, there are two important distinctions between the two sets of investigated NCs. First, the surrounding material differs: $CsPbBr_3$ NCs are dispersed in solution and drop-cast onto a glass substrate, while $CsPbI_3$ NCs are embedded in a fluorophosphate glass matrix. Second, the NCs in the glass matrix are smaller than those grown in solution. We begin our analysis with $CsPbI_3$ NCs. Detailed information on the carrier g-factors of the investigated $CsPbI_3$ NCs is provided in Reference [161].

5.2.1 $CsPbI_3$ nanocrystals

We begin by analyzing the optical properties of the four $CsPbI_3$ samples with NCs sizes ranging from 4 to 13 nm. The samples are labeled as #1–#4, corresponding to an increasing resonance energy. Consequently, the NC size decreases. Figure 5.9 shows the PL and absorption spectra at a temperature of $T = 1.6$ K for samples #1–#4.

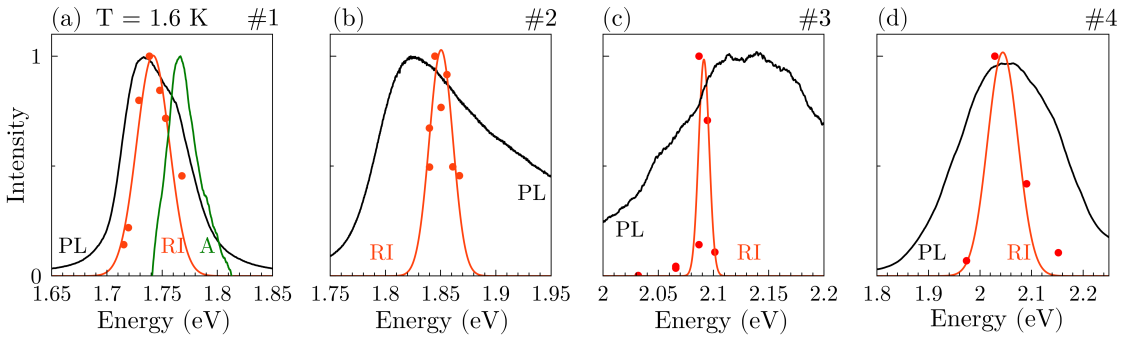

Figure 5.9: PL (black) and absorption A (green) spectra for $CsPbI_3$ NCs of varying sizes. The sample numbers (#) correspond to decreasing NC size, presented in the order from largest to smallest, ranging from 13 nm to 4 nm. Resonance profile of the Raman scattering intensity (RI) of the phonons is represented by red dots, with lines included as guides for the eye. Power densities used for PL and resonant Raman measurements are 4 mW/cm^2 for sample #1, 0.1 W/cm^2 for sample #2, and 0.3 W/cm^2 for samples #3 and #4.

The PL spectra exhibit maxima at energies of 1.734 eV for sample #1, 1.826 eV for sample #2, 2.124 eV for sample #3, and 2.051 eV for sample #4. The PL lines have a FWHM of approximately 100 meV to 200 meV, attributed to the size dispersion of NCs. In samples #2–#4, the large values for the FWHM of the PL lines indicate strong inhomogeneous broadening, preventing the observation of a pronounced exciton resonance in the absorption spectra. By tuning the laser photon energy, a subensemble of NCs with a specific mean size can be selectively addressed. The corresponding amplitudes of the Raman signals are shown in Figures 5.9(a)-(d) for the different samples, with the red dots representing the data points. For sample #1, Figure 5.9(a) reveals that the amplitude of the Raman signal reaches its maximum at an excitation energy of $E_{exc} = 1.741$ eV. Consequently, the resonant Raman spectra shown in Figures 5.10(a) and (b) are measured at this energy.

In Figure 5.10(a), the resonant Raman spectrum is displayed for a large energy range up to 9 meV, revealing numerous spectral lines. Several of these lines, with energies above 2 meV, can be attributed to the Raman scattering on optical phonons [180]. We will briefly return to the optical

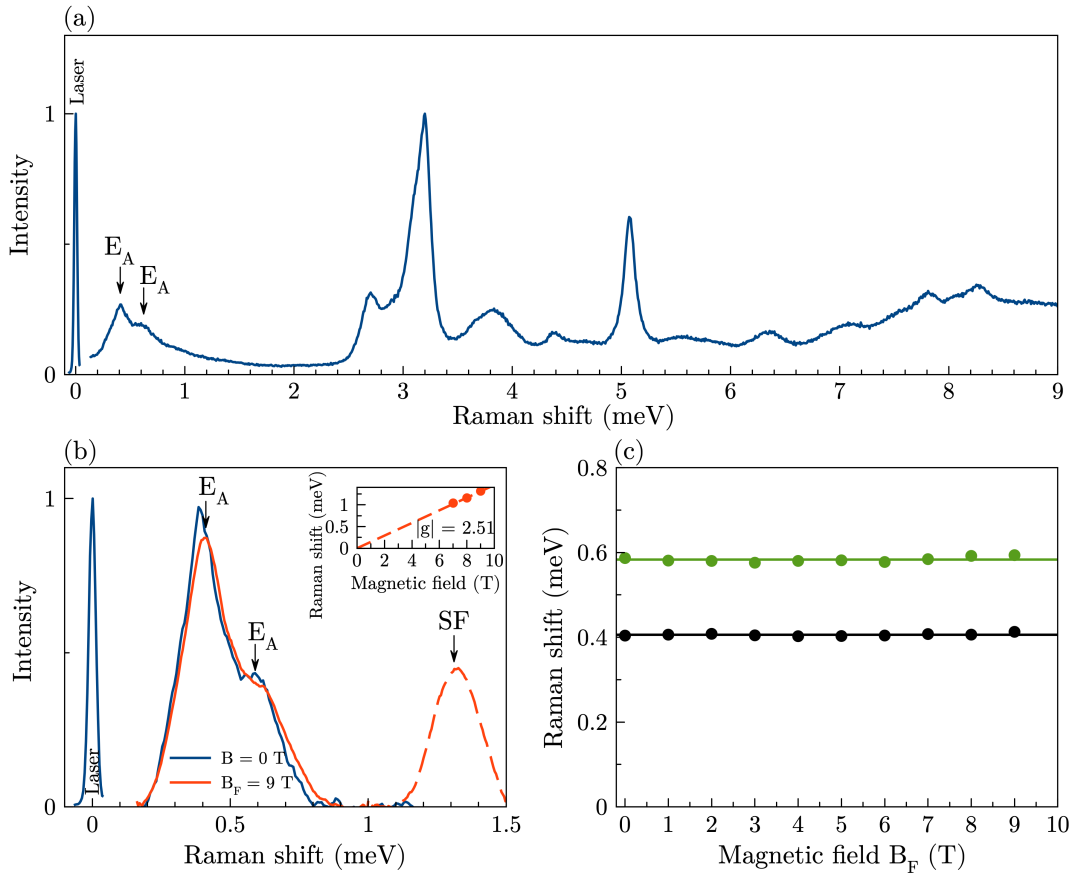

Figure 5.10: (a) Resonant Raman spectrum of sample #1 measured across a wide energy range at $T = 1.6\,\mathrm{K}$ using an excitation energy of $E_{\mathrm{exc}} = 1.741\,\mathrm{eV}$, co-linear polarization, and a power density of $P = 0.1\,\mathrm{W/cm^2}$. Arrows indicate the energies of the acoustic phonons E_{A}. (b) Comparison of the Raman spectra in the energy range of the acoustic phonons for longitudinal magnetic fields of $B = 0\,\mathrm{T}$ (blue) and $B_{\mathrm{F}} = 9\,\mathrm{T}$ (red). At $B_{\mathrm{F}} = 9\,\mathrm{T}$, a spin-flip (SF) line is observed (red dashed line), with its magnetic field dependence and determined g-factor value shown in the inset. (c) Magnetic field dependence of the acoustic phonons E_{A}, fitted with linear functions.

phonons in Figure 5.14. However, our primary focus is on the optically active confined acoustic phonons, which are identified near the laser line with peaks at Raman shifts of 0.41 meV and 0.58 meV for an excitation energy of $E_{\mathrm{exc}} = 1.741\,\mathrm{eV}$, labeled as E_{A}.

Next, we trace these two acoustic phonon peaks in the presence of a longitudinal magnetic field applied in Faraday geometry. Figure 5.10(b) shows the Raman spectra measured at $B = 0\,\mathrm{T}$, as well as in a longitudinal magnetic field of $B_{\mathrm{F}} = 9\,\mathrm{T}$. It can be observed that their Raman shifts remain almost the same in both zero and high magnetic fields. This behavior is analyzed in more detail in Figure 5.10(c), where the magnetic field dependence is presented in steps of $B_{\mathrm{F}} = 1\,\mathrm{T}$. The Raman shifts can be modeled by a constant function, confirming that the Raman shift of the acoustic phonons E_{A} do not exhibit a magnetic field dependence. Additionally, in the Raman spectrum at $B_{\mathrm{F}} = 9\,\mathrm{T}$, a SF at $E = 1.32\,\mathrm{meV}$ is observed. Its magnetic field dependence, shown in the inset of Figure 5.10(b), follows the Zeeman equation (Equation 2.2) and yields a g-factor of $|g| = 2.51$. In Reference [161], the g-factors for the electron and hole in $CsPbI_3$ NCs, measured at approximately the same excitation energy, are reported to be $g_{\mathrm{e}} = 2.2$ and $g_{\mathrm{h}} = 0.2$, respectively.

This results in a calculated bright exciton g-factor of $g_X = 2.4$, suggesting that the observed g-factor might be attributed to the exciton.

In Figures 5.10(a) and (b), the resonant Raman spectra are presented on Stokes side. This representation becomes clear by analyzing the polarization dependence of the exciton interaction with confined acoustic phonons on both Stokes and anti-Stokes sides, as shown in Figure 5.11. The resonant Raman spectra are presented for different linear polarization configurations at $B = 0$ T, with each configuration represented by two letters. The first letter specifies the excitation polarization, while the second indicates the detection polarization. Horizontal polarization is labeled as H, and vertical polarization as V. On Stokes side in Figure 5.11(a), the peaks E_A are clearly observable, particularly in co-linear polarization. In contrast, anti-Stokes side exhibits only a broad, low-intensity peak (see Figure 5.11(b)), where the two acoustic phonon peaks cannot be distinctly identified. Consequently, throughout the rest of this section, we focus on Stokes side when presenting resonant Raman spectra.

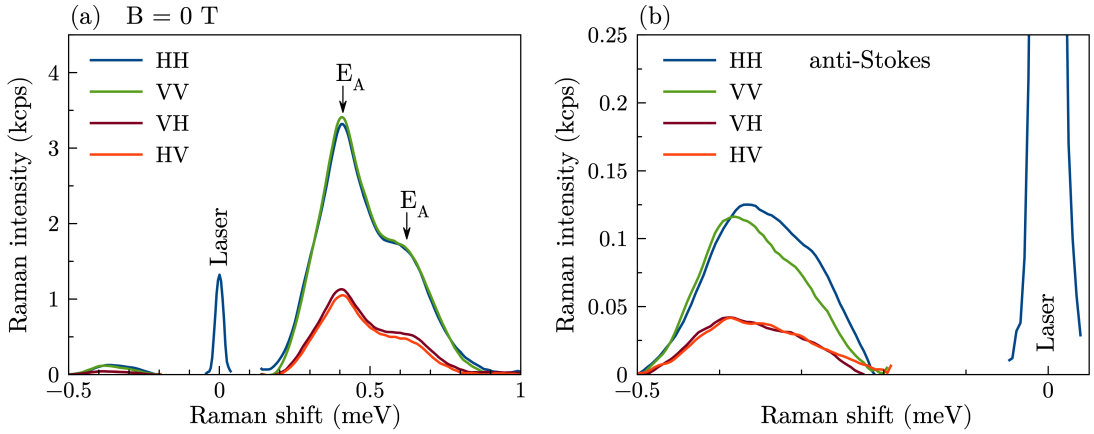

Figure 5.11: Polarization dependence of the exciton-phonon interaction at $B = 0$ T, measured with an excitation power density of 0.1 W/cm^2, where E_A represent the Raman shifts of the confined acoustic phonons. (a) The full spectra display both the anti-Stokes and Stokes spectral ranges. (b) Magnified anti-Stokes spectral range for improved visibility.

As a next step, we analyze the spectral dependence of the amplitudes of the exciton-phonon interaction, referred to as resonance profile. The procedure is identical for each sample: the laser photon energy is initially set near the PL maximum and then systematically tuned across it. For each sample, the amplitudes of the acoustic phonon peaks are evaluated. As shown in the resonance profiles in Figure 5.9 (red dots), the phonon intensity exhibits a pronounced spectral dependence near the PL maximum. Figures 5.12 (a)–(d) present representative resonant Raman spectra for each sample, with the corresponding excitation energies near the exciton resonance indicated at the top of each panel. Collectively, the four samples cover an energy range of approximately 600 meV. The spectra are fitted using multiple Gaussians functions, with the number of Gaussians corresponding to the identified acoustic phonon energies. These energies are indicated in the spectra by vertical arrows labeled E_A. The distance between the Gaussian fits increases from sample #1 to sample #4, promoting a more detailed investigation. To analyze this trend, we summarize all Raman shifts of the acoustic phonons as a function of the excitation energy in Figure 5.12(e). Different symbols represent the four samples: closed dots for sample #1, open diamonds for sample #2, squares for sample #3, and triangles for sample #4.

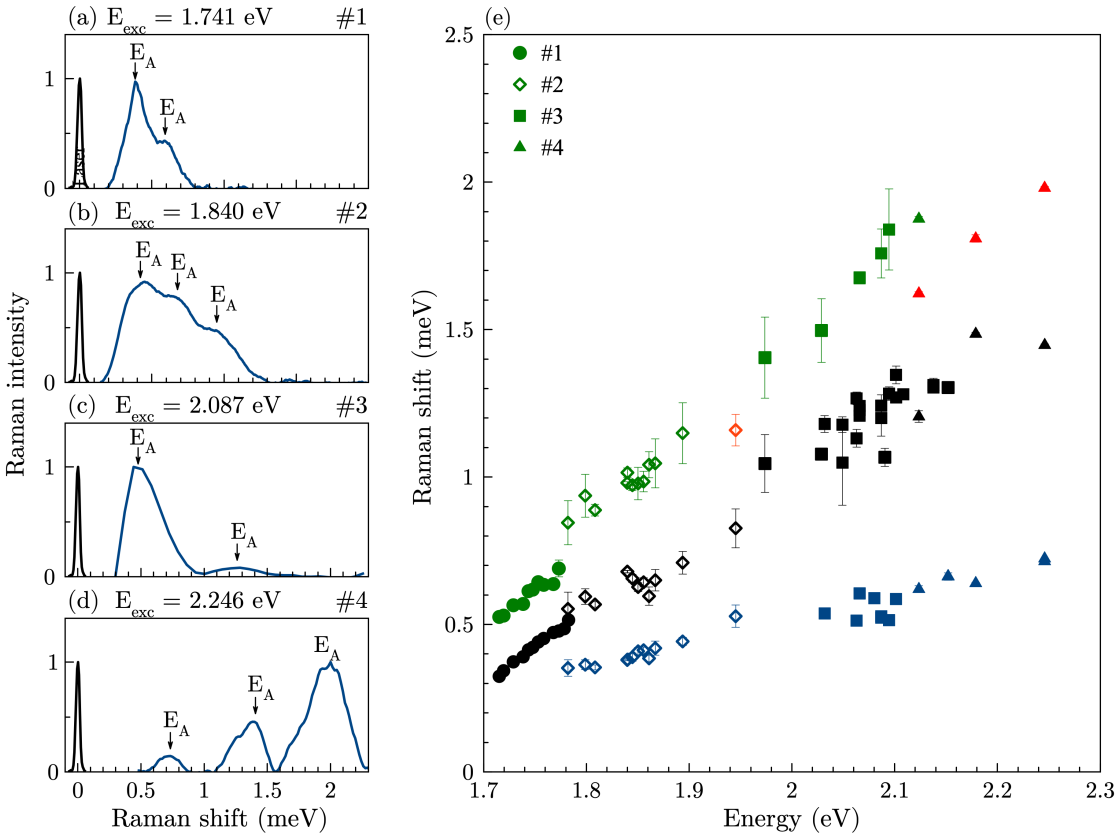

Figure 5.12: (a-d) Resonant Raman spectra of acoustic phonons in samples #1-4, measured with excitation energies near the exciton resonance, as indicated at the top of each panel. The Raman shifts of the acoustic phonons are marked by arrows. Power densities are 0.1 W/cm^2 (sample #1), 0.3 W/cm^2 (sample #2 and #3), and 2 W/cm^2 (sample #4). (e) Size dependence of confined acoustic phonons resonances in $CsPbI_3$ NCs.

Figure 5.12 clearly demonstrates that the Raman shift increases to a higher energy as the NC size decreases. Based on the observation that the Raman shift of the acoustic phonon mode depends strongly on the NC size, insights about the phonon properties can be obtained. In low-dimensional semiconductor materials, acoustic phonons become optically-active as a result of the folding of their dispersion in momentum space. The energies of the optically-active acoustic phonons are determined by the size of the NC. Confinement of acoustic phonons has been reported for different materials such as CdS doped glasses [69] and CuCl NCs [70].

The theoretical estimation of the phonon energies requires knowledge of the elastic constant tensor of the studied material and the size of the NC in order to calculate the Raman spectrum. To achieve this, DFT calculations of the total energy of the $CsPbI_3$ perovskite composition are performed by Mikhail O. Nestoklon. Then, the components of the elastic tensor for bulk $CsPbI_3$ are determined using the IRelast package [181] by applying deformations to the optimized system. For small strains (ϵ) Hooke's law applies and the elastic energy E of a crystal can be approximated as a quadratic function of the strain components

$$E \propto \frac{1}{2} V_0 \sum_{i,j=1}^{6} C_{i,j} e_i e_j, \tag{5.1}$$

where $C_{i,j}$ are the elastic constants, V_0 is the equilibrium volume of the unit cell, and e_j are the components of the strain tensor (ϵ), which are related to the deformation tensor. [182] The elastic constant tensor is a fourth-rank tensor, and in general, it can have up to $3^4 = 81$ independent constants. However, symmetry considerations enable a reduction in the number of independent elastic constants [183]. For example, in cubic materials, the are only three independent elastic constants [182]. The elastic constants can be derived from the second-order derivative of Equation (5.1) to [181]

$$C_{i,j} = \frac{1}{V_0}\left[\frac{\partial^2 E}{\partial \epsilon_i \partial \epsilon_j}\right]. \tag{5.2}$$

With the calculated components of the elastic tensor and the material densities for the different $CsPbI_3$ structural phases, we aim to calculate the Raman spectra for confined modes of acoustic phonons in NCs.

At low temperatures, the intensity of the Raman scattering is proportional to the overlap of the exciton and the confined phonon wave functions, as well as the amplitude of the phonon mode within the NC. The amplitude of the phonon mode depends on the sound velocity, which in turn is determined by the calculated elastic constants [184]. The peak positions in the Raman spectrum correspond to frequencies that are associated with the confined energy levels of acoustic phonons in the NC. The calculations account for the full anisotropy of the material and its shape, considering cubic, spherical, and oblate spherical NCs in the orthorhombic phase, as well as spherical NCs in the tetragonal phase. For ideal spherical $CsPbI_3$ NCs, the elastic parameters of the tetragonal or orthorhombic phases are compared. The calculated results are presented in Figure 5.13, where the amplitude of the Raman signal is shown by the color and the thickness of the lines is proportional to the relative volume variation during oscillation $\Delta V/V$ [185]. Note that the calculations are performed for Raman-active modes that involve volume changes during oscillation [186, 187]. For better comparison, the experimentally observed Raman peaks, shown in Figure 5.12, are represented as open symbols along the calculated spectra.

The comparison of the calculated Raman signal with the experimental data reveals that the measured signal can be unambiguously attributed to Raman scattering from confined modes of acoustic phonons in the NC. From Figure 5.13, it appears that the experimental data are best modeled using NCs with an oblate spherical shape in the orthorhombic phase. While the Raman shifts observed in Figure 5.12 are initially assigned to four phonon modes with a linear dispersion, a comparison with the modeled acoustic phonon modes reveals that these Raman shifts correspond to numerous phonon modes.

Combining optical measurements of Raman spectra of acoustic phonons confined in NCs with DFT calculations provides valuable insights into the NCs, including their shape, structural phase, and size. To evaluate the shape of NCs, usually scanning transmission electron microscopy can be used. For samples embedded in a glass matrix, the technique may fail due to disruptions caused by electron beam-induced charging on the sample surface [58]. After synthesis, the size of NCs is typically measured using absorption spectroscopy. As observed, the Raman shift of the confined acoustic phonons depends on the excitation energy, which is directly related to the NC size. This suggests that Raman scattering could serve as an additional tool for determining the size of the NCs. By calculating the Raman shift for a given NC size and comparing the theoretical spectrum with experimental measurements, the NC size can be determined. Using tight-binding parameters, the best empirical fit from Reference [58] provides the following relationship between

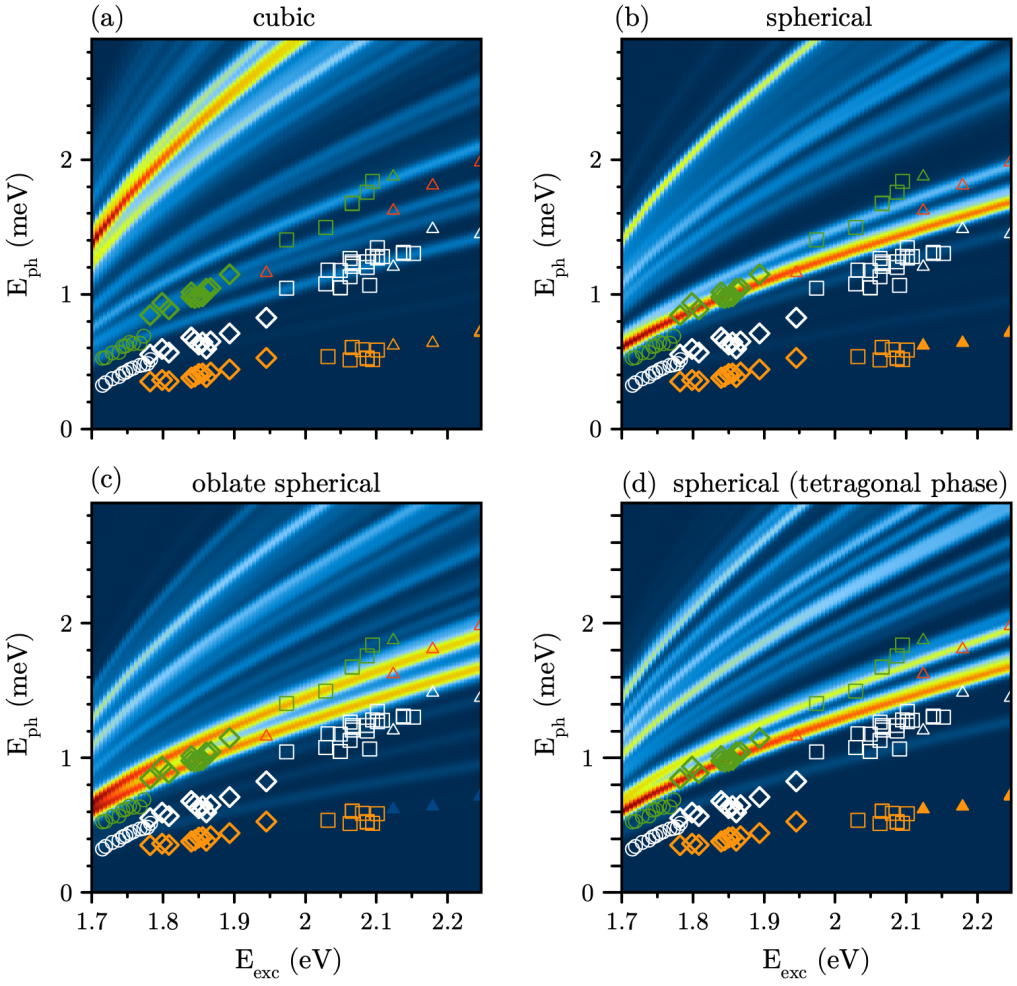

Figure 5.13: Calculated Raman spectra for different NC shapes: (a) cubic, (b) spherical, (c) oblate spherical NCs in the orthorhombic phase and (d) spherical NC in the tetragonal phase. Symbols represent the experimentally observed confined acoustic phonon modes from Figure 5.12.

the energy of the exciton resonance E_X in electronvolt, and the length L of the cube with the same volume as a considered NC in nanometer

$$E_X = 1.652 + \frac{11}{2.8 + L^2}. \tag{5.3}$$

In the experiment, the excitation energy is set to the exciton resonance. In conclusion, Raman scattering on confined acoustic phonons provides valuable insights alongside traditional techniques such as absorption spectroscopy and scanning transmission electron microscopy, offering an additional method for characterizing NCs in terms of their shape, structural phase, and size. Moreover, this approach is applicable to any NC composition where confined acoustic phonons are observed.

As we have identified numerous confined acoustic phonon modes that shift as a function of the excitation energy and, consequently, on the NC size, we now investigate whether a similar behavior can be observed for the optical phonon modes. Figures 5.14(a)-(d) present the resonant Raman spectrum for each sample. Within the higher energy range of 2.5 meV to 3 meV, up to three optical phonons are observed, with their energies marked by vertical arrows. The dependence of the optical phonon modes on the excitation energy is shown in Figure 5.14(e).

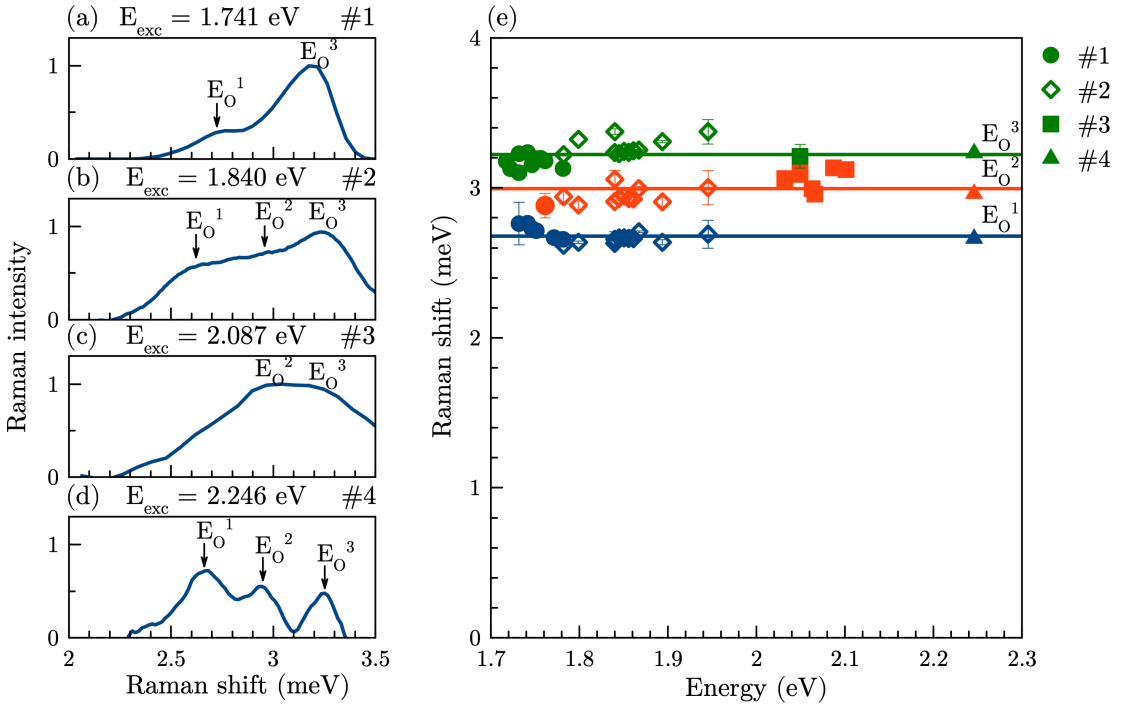

Figure 5.14: (a-d) Resonant Raman spectra of optical phonons in samples #1-4, excited with excitation energies near the exciton resonance, as indicated at the top of each panel. The Raman shifts corresponding to the optical phonons are indicated by arrows. Power densities are 0.1 W/cm^2 (sample #1), 0.3 W/cm^2 (sample #2 and #3), and 2 W/cm^2 (sample #4). (e) Raman shifts of the optical phonon modes in $CsPbI_3$ NCs.

Unlike the acoustic phonons, the energies of the optical phonons remain independent of the excitation energy, as shown in Figure 5.14(e). The three optical phonons modes can be described by a constant function, highlighting their independence from the excitation energy and, therefore, NC size. As optical phonon modes are not confined by the dimensions of the NCs, their Raman shifts remain unaffected by variations in the NC size.

In Section 5.2.2, we investigate whether the dispersion of the confined acoustic phonons on the NC size can also be observed in $CsPbBr_3$ NCs.

5.2.2 $CsPbBr_3$ nanocrystals

The optical properties for the $CsPbBr_3$ NCs are shown in Figure 5.1 and discussed in Section 5.1. A resonant Raman spectrum covering a broad energy range up to 9 meV for sample #3 is presented in Figure 5.15(a). The sample is excited at the exciton resonance, as shown in Figure 5.1(c), with an excitation energy of $E_{\mathrm{exc}} = 2.43\,\mathrm{eV}$.

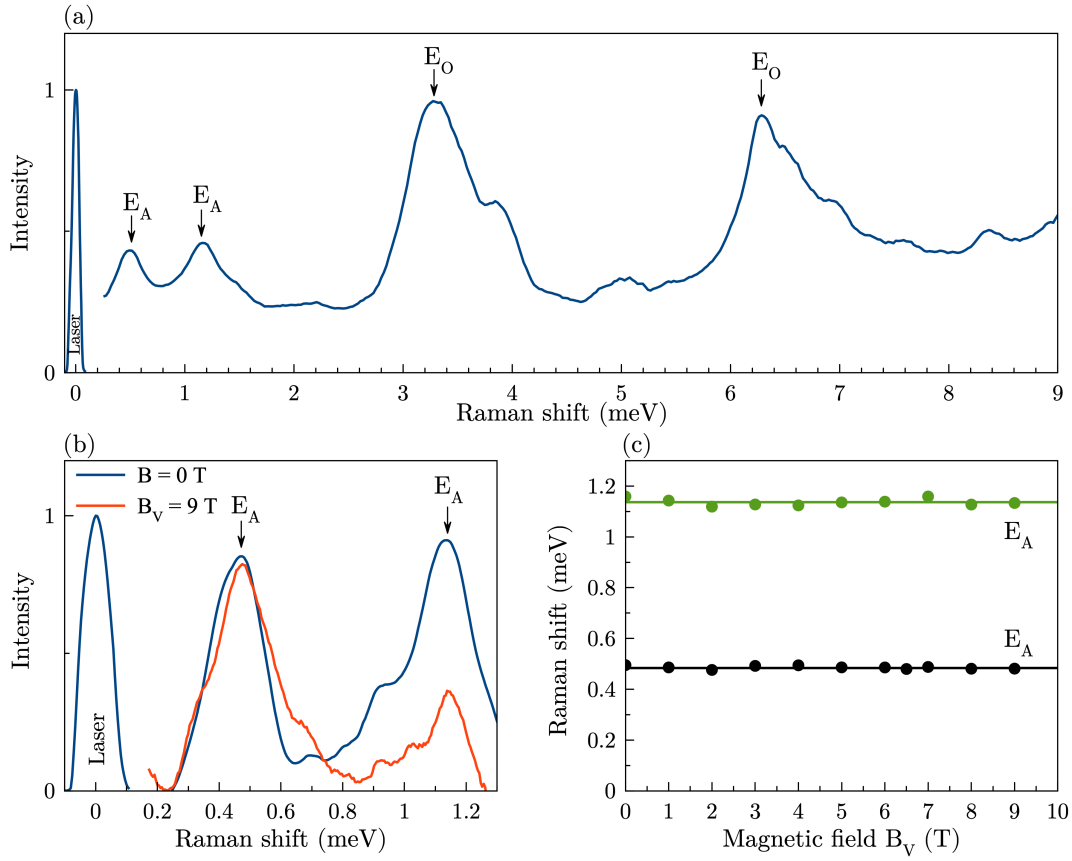

Figure 5.15: (a) Resonant Raman spectrum of sample #3 (8 nm) measured across a wide energy range at $T = 1.6\,\mathrm{K}$ with an excitation energy of $E_{\mathrm{exc}} = 2.43\,\mathrm{eV}$ and a power density of $P = 7\ \mathrm{W/cm^2}$. Arrows indicate the energies of the acoustic and optical phonons $E_{\mathrm{A,O}}$, respectively. (b) Comparison of the Raman spectra in the energy range of the acoustic phonons for transverse magnetic fields of $B = 0\,\mathrm{T}$ (blue) and $B_{\mathrm{V}} = 9\,\mathrm{T}$ (red). (c) Magnetic field dependence of the acoustic phonons E_{A}, fitted with constant functions.

In Figure 5.15(a), the resonant Raman spectrum reveals numerous spectral lines. Several of these lines, with energies above 2 meV, can be attributed to Raman scattering from optical phonons. In Reference [188], optical phonons with high intensity have been both experimentally and theoretically identified at energies of 3.1 meV and 6.2 meV. Close to the laser line, two peaks with Raman shifts of 0.50 eV and 1.16 eV can be identified, labeled as E_{A}. Section 5.2.1 demonstrated that the optical phonons show no correlation between their Raman shifts and the NC size, whereas a strong dependence is observed for the confined acoustic phonon modes in the smaller energy range of up to 1.3 meV. These two peaks, assigned to acoustic phonons, are traced in a transverse magnetic field in Voigt geometry. Figure 5.15(b) shows resonant Raman spectra measured at $B = 0\,\mathrm{T}$ and $B_{\mathrm{V}} = 9\,\mathrm{T}$ in Voigt geometry. As indicated by the arrows pointing at the maximum of the peaks, the Raman shifts remain almost unchanged in both zero and high magnetic fields.

In Figure 5.15(c), the evaluation of the Raman shifts for both peaks in magnetic field steps of $B_V = 1\,T$ is presented. The Raman shifts can be fitted with a constant function, confirming the Raman shift of the acoustic phonons E_A does not exhibit a magnetic field dependence.

The polarization dependence of the exciton interaction with acoustic phonons has also been examined for these three samples of $CsPbBr_3$ NCs. Similar to $CsPbI_3$, the peaks are clearly observed on Stokes side, while on anti-Stokes side, the peaks are broad and exhibit low intensity. Figures 5.16(a)-(c) show exemplary resonant Raman spectra for each sample on Stokes side, with the respective excitation energies near the exciton resonance indicated at the top of each panel. These three samples cover an energy range of approximately 150 meV. The spectra are fitted using multiple Gaussian functions, with the number of Gaussians corresponding to the identified acoustic phonon energies. These energies are indicated in the spectra by vertical arrows labeled E_A. The dependence of the Raman shifts of the acoustic phonons as a function of the excitation energy is presented in Figure 5.16(d). Different symbols represent the three samples: closed dots for sample #1, open diamonds for sample #2, and squares for sample #3.

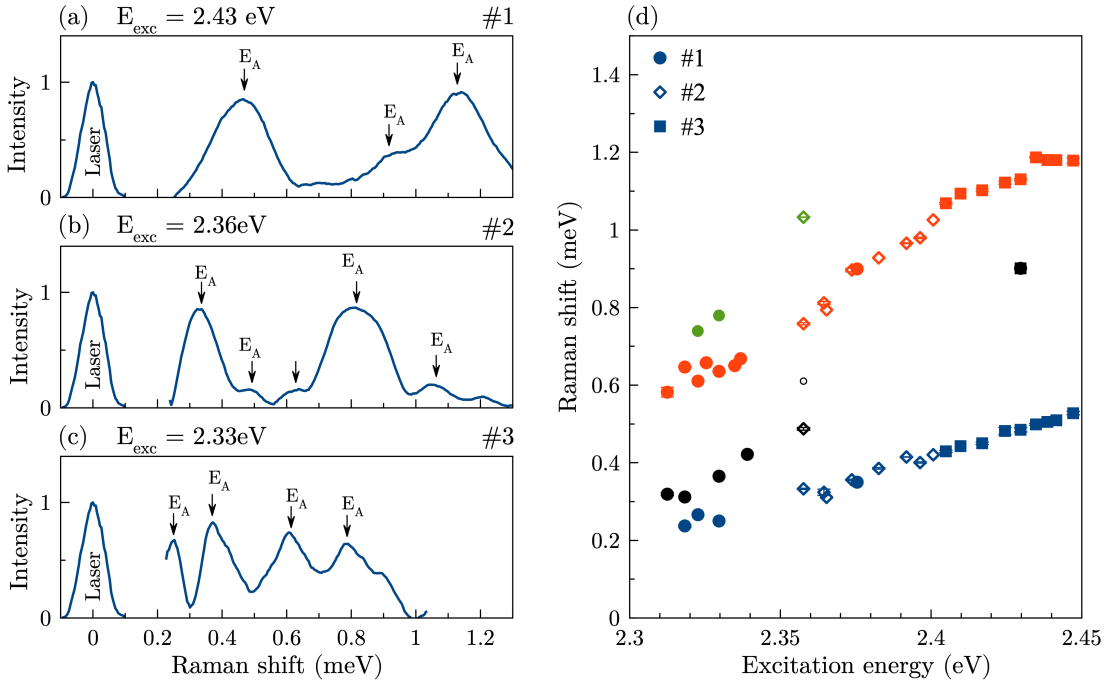

Figure 5.16: (a-c) Resonant Raman spectra of acoustic phonons in samples #1–3, excited near the exciton resonance with the specified excitation energies on top of each panel. Power densities are 7 W/cm^2 (sample #1) and 3 W/cm^2 (sample #2 and #3). The Raman shifts of the acoustic phonons are marked by arrows. (d) Size dependence of confined acoustic phonons resonances in $CsPbBr_3$ NCs.

In Figure 5.16(d), a strong dependence of the acoustic phonon modes on the excitation energy and NC size is observed for $CsPbBr_3$ NCs. As is also the case for the $CsPbI_3$ NCs, initially, the size dependence of the confined acoustic phonons resonances appears to be linear. As the next step, DFT calculations, as presented for $CsPbI_3$ NCs in the previous section, are needed to provide a more detailed understanding of the size dependence of confined acoustic phonons resonances, as well as the NC shape, structural phase, and size.

5.3 Conclusions

In this chapter, we selectively excited different subensembles of $CsPbBr_3$ and $CsPbI_3$NCs with varying mean sizes by tuning the laser energy. Using the technique of SFRS, we identified SFs originating from resident electrons, holes, and their combination in $CsPbBr_3$ NCs, revealing a strong dependence of the electron and hole g-factor on the NC size. While the general trend of the electron and hole g-factors aligns with that observed in bulk lead halide perovskites, the absolute values differ. In particular, the hole g-factor in sample #1 and #2 remain close to the bulk dependence, whereas, in the sample with the smallest NC sizes, quantum confinement leads to significant deviations from the bulk value. This indicates that the NC size of 8 nm is in a regime where quantum confinement strongly influences the spin properties.

Furthermore, resonant Raman spectra revealed scattering from acoustic and optical phonons in $CsPbBr_3$ and $CsPbI_3$ NCs. In low-dimensional semiconductor materials, acoustic phonons become optically-active due to the folding of their dispersion in momentum space, enabling us to observe optically-active acoustic phonons confined within a NC. While the energies of optical phonons remain unaffected by the NC size, confined acoustic phonons exhibit a strong dependence on the NC size. We analyzed the size dependence of the confined acoustic phonons resonances for small $CsPbI_3$ and large $CsPbBr_3$ NCs through their interaction with photogenerated excitons. To calculate the Raman spectra of the acoustic phonon modes for $CsPbI_3$ NCs, DFT calculations are performed for different shapes and structural phases of the NCs. The comparison between the calculated and experimental Raman spectrum confirms that the observed Raman signal originates from confined acoustic phonons modes within the NC. The best agreement between the experimental data and theoretical Raman spectra was found for oblate spherical NCs in the orthorhombic phase. This strong dependence of the optically-active confined acoustic phonons on the NC size in $CsPbI_3$ motivates further investigation of these acoustic phonons modes in $CsPbBr_3$ NCs through additional DFT calculations. Moreover, resonant Raman scattering could serve as a powerful tool to explore lead halide perovskites with alternative compositions, providing valuable information about the shape, structural phase, and size of the NCs.

Summary and Outlook

Throughout this thesis, the technique of spin-flip Raman scattering (SFRS) was employed as a spectroscopic tool to investigate the Landé factors in three-dimensional, two-dimensional, and zero-dimensional lead halide perovskites. In Chapter 3 a bulk single $MAPbI_3$ crystal was investigated with SFRS. For the strongly polarization-dependent SFRS spectra of single electron and hole spin-flips (SFs), a simple model combining a four-level excitation scheme with resident carriers in the ground states and excited three-particle states and a non-perfect Faraday geometry successfully reproduced the main features of the polarization dependencies. The systematic polarization analysis provides additional evidence that the observed SFRS signals originate from resident carriers in the lead halide perovskite crystal and offers a powerful approach for measuring the sign of g-factors in so far unexplored materials. Besides single SFs, SF processes of both combined carriers and those involving two electrons and holes were observed, highlighting the role of resident carriers as a distinct feature of lead halide perovskites. Additionally, a second electron and hole SF line, with an opposite g-factor anisotropy, was identified, arising from a different sample domain with a different axis orientation. The comparison of the SF intensities between the electrons and holes of the different structural domains indicate that the sample primarily composed of a single domain. This highlight the potential of SFRS to probe the domain structure in future studies of bulk perovskite single crystals.

In Chapters 4 and 5, the technique of SFRS was used to systematically investigate the impact of quantum confinement on the Landé factors of resident carriers in two-dimensional and zero-dimensional lead halide perovskites. The observed trends for the electron and hole g-factor in low-dimensional lead halide perovskites are summarized in Figure 5.17 and compared to the universal dependence of the electron and hole g-factors on the band gap energy in bulk lead halide perovskites. The comparison with bulk perovskites provides insights into how quantum confinement modifies the g-factor through shifts in the effective band gap energy, in contrast to changes in bulk perovskites induced by compositional substitution. For the 2D perovskites, samples with various inorganic layer thicknesses and halide compositions were investigated by the technique of SFRS to cover a broad energy range of approximately 1.3 eV. The general trend for both the electron and hole g-factors follows the bulk dependence: as the energy increases, g_e decreases, while g_h increases. As highlighted in the inset of Figure 5.17, a similar trend is also observed for $CsPbBr_3$ NCs. However, the absolute g-factor values for 2D perovskites and NCs show significant deviations from those reported in bulk lead halide perovskites, indicating that the quantum confinement has a strong influence on the spin properties. This enables the tuning of spin properties in lead halide perovskites through quantum confinement by adjusting the inorganic layer thickness in 2D perovskites or the NC size. Since the band gap energy can be precisely controlled by quantum confinement, this offers a more flexible alternative to the compositional modifications required in bulk perovskites, making low-dimensional lead halide perovskites particularly interesting for spintronic applications. Additional SFRS measurements on NCs with varying sizes or compositions would be valuable to extend the dependence of the g-factor beyond the narrow energy range covered by the three samples of $CsPbBr_3$ NCs. In the following, the individual results for the 2D perovskites and perovskites NCs will be highlighted.

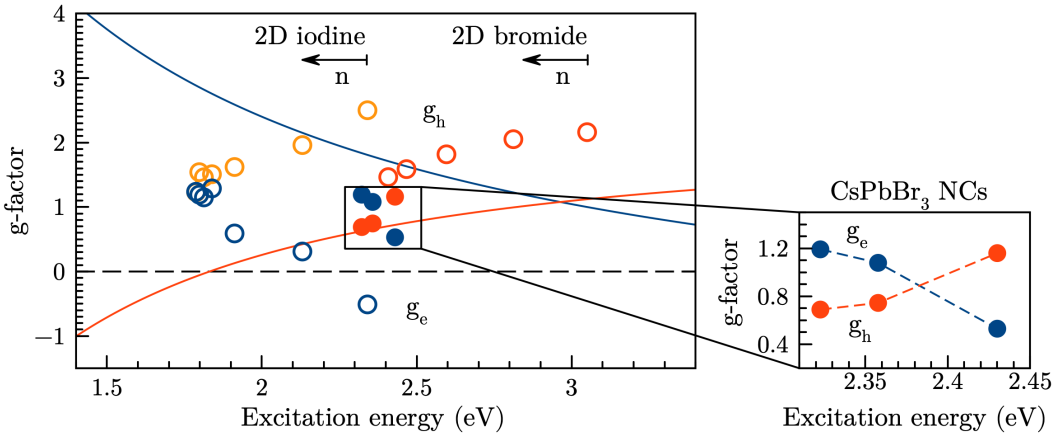

Figure 5.17: Electron and hole g-factors as a function of the excitation energy, combining the data from Figure 4.19 for 2D perovskites and from Figure 5.8 for $CsPbBr_3$ nanocrystals (NCs) in Voigt geometry. Open dots represent 2D perovskites, while closed dots correspond to NCs. Inset provides magnified view on the electron and hole g-factor dependence in NCs, with dashed lines as guides of the eye. Solid lines indicate the universal dependence of the electron and hole g-factors on the band gap energy in bulk lead halide perovskites, as described in Reference [62].

In Chapter 4, a hyperfine interaction between the electron and nuclear spin system in PEA_2PbI4 with $n = 1$ was identified through dynamic nuclear polarization, resulting in a maximum Overhauser field of $B_{N,e} = -0.6\,T$. In contrast to the investigated bulk $MAPbI_3$ signal in Chapter 3, no strong polarization dependence was observed. Consequently, the negative sign of the electron g-factor was determined based on the orientation of the Overhauser field as an alternative approach, despite the expectation of a stronger hyperfine interaction of the hole with the nuclei due to s-type wave function.

Chapter 5 builds up on the investigation of the impact of dimensionality on the carrier g-factor in $CsPbBr_3$ NCs. As the NC ensemble consists of various NC sizes, selectively exciting the exciton transition enables measurements of a specific NC size. In $CsPbI_3$ and $CsPbBr_3$ NCs, resonant Raman scattering revealed the presence of optically-active acoustic phonons confined within the NC. While the Raman shifts of optical phonons remain independent of the NC size, the Raman shifts of confined acoustic phonons were observed to vary with the NC size. Density functional theory (DFT) calculations for $CsPbI_3$ NCs confirmed that the Raman signals originate from confined acoustic phonons modes. By comparing the calculated and experimentally measured Raman spectra, basic properties of the NC, such as shape, structural phase, and size, can be extracted using a single technique. Therefore, resonant Raman scattering proves to be a powerful optical technique that reveals important characteristics of NCs. As these optically confined acoustic phonons were observed in two different sample compositions and surrounding materials, we are confident that this study could be extended to include other perovskite compositions and potentially other lower-dimensional systems of lead halide perovskite.

Bibliography

[1] M. R. Filip and F. Giustino, "The geometric blueprint of perovskites", Proceedings of the National Academy of Sciences **115**, 5397 (2018)
DOI: 10.1073/pnas.1719179115.

[2] J. P. Martínez-Pastor, P. P. Boix, and G. Xing, *Metal Halide Perovskites for Generation, Manipulation and Detection of Light* (Elsevier, 2023),
DOI: 10.1016/C2021-0-00815-4.

[3] P. Docampo and T. Bein, "A Long-Term View on Perovskite Optoelectronics", Accounts of Chemical Research **49**, 339 (2016)
DOI: 10.1021/acs.accounts.5b00465.

[4] H. Chen, Y. Chen, T. Zhang, X. Liu, X. Wang, and Y. Zhao, "Advances to High-Performance Black-Phase $FAPbI_3$ Perovskite for Efficient and Stable Photovoltaics", Small Structures **2**, 2000130 (2021)
DOI: 10.1002/sstr.202000130.

[5] S. D. Stranks, G. E. Eperon, G. Grancini, C. Menelaou, M. J. P. Alocer, T. Leitjtens, L. M. Herz, A. Petrozza, and H. J. Snaith, "Electron-Hole Diffusion Lengths Exceeding 1 Micrometer in an Organometal Trihalide Perovskite Absorber", Science **342**, 341 (2013)
DOI: 10.1126/science.1243982.

[6] G. Xing, N. Mathews, S. Sun, S. S. Lim, Y. M. Lam, M. Grätzel, S. Mhausalkar, and T. C. Sum, "Long-Range Balanced Electron- and Hole-Transport Lengths in Organic-Inorganic $CH_3NH_3PbI_3$", Science **342**, 344 (2013)
DOI: 10.1126/science.1243167.

[7] A. Kojima, K. Teshima, Y. Shirai, and T. Miyasaka, "Organometal Halide Perovskites as Visible-Light Sensitizers for Photovoltaic Cells", Journal of the American Chemical Society **131**, 6050 (2009)
DOI: 10.1021/ja809598r.

[8] H. Min, D. Lee, J. Kim, G. Kim, K. S. Lee, J. Kim, M. J. Paik, Y. K. Kim, K. S. Kim, M. G. Kim, T. J. Shin, and S. I. Seok, "Perovskite solar cells with atomically coherent interlayers on SnO_2 electrodes", Nature **598**, 444 (2021)
DOI: 10.1038/s41586-021-03964-8.

[9] Z. Zhang, Y. Liu, Q. Sun, H. Ban, Z. Liu, H. Yu, X. Li, L. Dai, W. Yang, Y. Shen, and M. Wang, "The importance of elemental lead to perovskites photovoltaics", Chemistry of Inorganic Materials **1**, 100017 (2023)
DOI: 10.1016/j.cinorg.2023.100017.

[10] Y. Jiang, X. Wang, and A. Pan, "Properties of Excitons and Photogenerated Charge Carriers in Metal Halide Perovskites", Advanced Materials **31**, 1806671 (2019)
DOI: 10.1002/adma.201806671.

[11] Q. A. Akkerman, V. D'Innocenzo, S. Accornero, A. Scarpellini, A. Petrozza, M. Prato, and L. Manna, "Tuning the Optical Properties of Cesium Lead Halide Perovskite Nanocrystals by Anion Exchange Reactions", Journal of the American Chemical Society **137**, 10276 (2015)
DOI: 10.1021/jacs.5b05602.

[12] C. Katan, N. Mercier, and J. Even, "Quantum and Dielectric Confinement Effects in Lower-Dimensional Hybrid Perovskite Semiconductors", Chemical Reviews **119**, 3140 (2019)
DOI: 10.1021/acs.chemrev.8b00417.

[13] J. Wang, C. Zhang, H. Liu, R. McLaughlin, Y. Zhai, S. R. Vardeny, X. Liu, S. McGill, D. Semenov, H. Guo, R. Tsuchikawa, V. V. Deshpande, D. Sun, and Z. V. Vardeny, "Spin-optoelectronic devices based on hybrid organic-inorganic trihalide perovskites", Nature Communications **10**, 129 (2019)
DOI: 10.1038/s41467-018-07952-x.

[14] J. Xu, K. Li, U. N. Huynh, M. Fadel, J. Huang, R. Sundararaman, V. Vardeny, and Y. Ping, "How spin relaxes and dephases in bulk halide perovskites", Nature Communications **15**, 188 (2024)
DOI: 10.1038/s41467-023-42835-w.

[15] C. Harkort, D. Kudlacik, N. E. Kopteva, D. R. Yakovlev, M. Karzel, E. Kirstein, O. Hordiichuk, M. V. Kovalenko, and M. Bayer, "Spin-flip Raman Scattering on Electrons and Holes in Two-Dimensional $(PEA)_2PbI_4$ Perovskites", Small **19**, 2300988 (2023)
DOI: 10.1002/smll.202300988, ©2023 Wiley.

[16] D. Giovanni, H. Ma, J. Chua, M. Grätzel, R. Ramesh, S. Mhaisalkar, N. Mathews, and T. C. Sum, "Highly Spin-Polarized Carrier Dynamics and Ultralarge Photoinduced Magnetization in $CH_3NH_3PbI_3$ Perovskite Thin Films", Nano Letters **15**, 1553 (2015)
DOI: 10.1021/nl5039314.

[17] M. O. Nestoklon, S. V. Goupalov, R. I. Dzhioev, O. S. Ken, V. L. Korenev, Y. G. Kusrayev, V. F. Sapega, C. de Weerd, L. Gomez, T. Gregorkiewicz, J. Lin, K. Suenaga, Y. Fujiwara, L. B. Matyushkin, and I. N. Yassievich, "Optical orientation and alignment of excitons in ensembles of inorganic perovskite nanocrystals", Physical Review B **97**, 235304 (2018)
DOI: 10.1103/PhysRevB.97.235304.

[18] E. Kirstein, D. R. Yakovlev, M. M. Glazov, E. Evers, E. A. Zhukov, V. V. Belykh, N. E. Kopteva, D. Kudlacik, O. Nazarenko, D. Dirin, M. V. Kovalenko, and M. Bayer, "Lead-Dominated Hyperfine Interaction Impacting the Carrier Spin Dynamics in Halide Perovskites", Advanced Materials **34**, 2105263 (2022)
DOI: 10.1002/adma.202105263.

[19] P. Odenthal, W. Talmadge, N. Gundlach, R. Wang, C. Zhang, D. Sun, Z.-G. Yu, Z. V. Vardeny, and Y. S. Li, "Spin-polarized exciton quantum beating in hybrid organic–inorganic perovskites", Nature Physics **13**, 894 (2017)
DOI: 10.1038/nphys4145.

[20] K. Ema, K. Umeda, M. Toda, C. Yajima, Y. Arai, H. Kunugita, D. Wolverson, and J. J. Davies, "Huge exchange energy and fine structure of excitons in an organic-inorganic quantum well material", Physical Review B **73**, 241310 (2006)
DOI: 10.1103/PhysRevB.73.241310.

[21] J. Debus, D. Kudlacik, V. Sapega, T. Shamirzaev, D. Yakovlev, D. Reuter, A. Wieck, A. Waag, and M. Bayer, "Basic Requirements of Spin-Flip Raman Scattering on Excitonic Resonances and Its Modulation through Additional High-Energy Illumination in Semiconductor Heterostructures", Physics of the Solid State **60**, 1611 (2018)
DOI: 10.1134/S1063783418080036.

[22] V. F. Sapega, T. Ruf, M. Cardona, K. Ploog, E. L. Ivchenko, and D. N. Mirlin, "Resonant Raman scattering due to bound-carrier spin flip in GaAs/$Al_xGa_{1-x}As$ quantum wells", Physical Review B **50**, 2510 (1994)
DOI: 10.1103/PhysRevB.50.2510.

[23] A. A. Sirenko, T. Ruf, M. Cardona, D. R. Yakovlev, W. Ossau, A. Waag, and G. Landwehr, "Electron and hole g factors measured by spin-flip Raman scattering in CdTe/$Cd_{1-x}Mg_xTe$ single quantum wells", Physical Review B **56**, 2114 (1997)
DOI: 10.1103/PhysRevB.56.2114.

[24] J. Debus, D. Dunker, V. F. Sapega, D. R. Yakovlev, G. Karczewski, T. Wojtowicz, J. Kossut, and M. Bayer, "Spin-flip Raman scattering of the neutral and charged excitons confined in a CdTe/(Cd,Mg)Te quantum well", Physical Review B **87**, 205316 (2013)
DOI: 10.1103/PhysRevB.87.205316.

[25] A. A. Sirenko, V. I. Belitsky, T. Ruf, M. Cardona, A. I. Ekimov, and C. Trallero-Giner, "Spin-flip and acoustic-phonon Raman scattering in CdS nanocrystals", Physical Review B **58**, 2077 (1998)
DOI: 10.1103/PhysRevB.58.2077.

[26] D. G. Thomas and J. J. Hopfield, "Spin-Flip Raman Scattering in Cadmium Sulfide", Phys. Rev. **175**, 1021 (1968)
DOI: 10.1103/PhysRev.175.1021.

[27] V. F. Sapega, M. Cardona, K. Ploog, E. L. Ivchenko, and D. N. Mirlin, "Spin-flip Raman scattering in GaAs/$Al_xGa_{1-x}As$ multiple quantum wells", Physical Review B **45**, 4320 (1992)
DOI: 10.1103/PhysRevB.45.4320.

[28] J. Debus, T. S. Shamirzaev, D. Dunker, V. F. Sapega, E. L. Ivchenko, D. R. Yakovlev, A. I. Toropov, and M. Bayer, "Spin-flip Raman scattering of the Γ–X mixed exciton in indirect band gap (In,Al)As/AlAs quantum dots", Physical Review B **90**, 125431 (2014)
DOI: 10.1103/PhysRevB.90.125431.

[29] J. Debus, D. Kudlacik, V. F. Sapega, D. Dunker, P. Bohn, F. Paßmann, D. Braukmann, J. Rautert, D. R. Yakovlev, D. Reuter, A. D. Wieck, and M. Bayer, "Nuclear spin polarization in the electron spin-flip Raman scattering of singly charged (In,Ga)As/GaAs quantum dots", Physical Review B **92**, 195421 (2015)
DOI: 10.1103/PhysRevB.92.195421.

[30] J. Debus, D. Kudlacik, P. Waldkirch, V. F. Sapega, S. Scholz, A. Ludwig, A. D. Wieck, and M. Bayer, "Efficiency enhancement of the coherent electron spin-flip Raman scattering through thermal phonons in (In,Ga)As/GaAs quantum dots", Physical Review B **95**, 201303 (2017)
DOI: 10.1103/PhysRevB.95.201303.

[31] D. Kudlacik, V. F. Sapega, D. R. Yakovlev, I. V. Kalitukha, E. V. Shornikova, A. V. Rodina, E. L. Ivchenko, G. S. Dimitriev, M. Nasilowski, B. Dubertret, and M. Bayer, "Single and Double Electron Spin-Flip Raman Scattering in CdSe Colloidal Nanoplatelets", Nano Letters **20**, 517 (2020)
DOI: 10.1021/acs.nanolett.9b04262.

[32] H. Akamine, S. Okumura, S. Farjami, M. Yasukazu, and M. Nishida, "Imaging of surface spin textures on bulk crystals by scanning electron microscopy", Scientific Reports **6**, 37265 (2016)
DOI: 10.1038/srep37265.

[33] S. Wieghold, J.-P. Correa-Baena, L. Nienhaus, S. Sun, K. E. Shulenberger, Z. Liu, J. S. Tresback, S. S. Shin, M. G. Bawendi, and T. Buonassisi, "Precursor Concentration Affects Grain Size, Crystal Orientation, and Local Performance in Mixed-Ion Lead Perovskite Solar Cells", ACS Applied Energy Materials **1**, 6801 (2018)
DOI: 10.1021/acsaem.8b00913.

[34] R. Ohmann, L. K. Ono, H.-S. Kim, H. Lin, M. V. Lee, Y. Li, N.-G. Park, and Y. Qi, "Real-Space Imaging of the Atomic Structure of Organic–Inorganic Perovskite", Journal of the American Chemical Society **137**, 16049 (2015)
DOI: 10.1021/jacs.5b08227.

[35] W. Zhou and Z. L. Wang, *Scanning Microscopy for Nanotechnology*, 1st ed. (Springer New York, NY, 2006),
DOI: 10.1007/978-0-387-39620-0.

[36] S. Wieghold and L. Nienhaus, "Nanoscale properties of lead halide perovskites by scanning tunneling microscopy", EcoMat **3**, e12081 (2021)
DOI: 10.1002/eom2.12081.

[37] A. V. Rodina and E. L. Ivchenko, "Theory of resonant Raman scattering due to spin flips of resident charge carriers and excitons in perovskite semiconductors", Physical Review B **106**, 245202 (2022)
DOI: 10.1103/PhysRevB.106.245202.

[38] D. Bimberg, *Semiconductor Nanostructures* (Springer Berlin, Heidelberg, 2008),
DOI: 10.1007/978-3-540-77899-8.

[39] L. Jacak, A. Wójs, and P. Hawrylak, *Quantum Dots* (Springer Berlin, Heidelberg, 1998),
DOI: 10.1007/978-3-642-72002-4.

[40] D. Roy, A. K. Srivastava, K. Mukhopadhyay, and E. P. Namburi, *0D, 1D, 2D & 3D Nano Materials: Synthesis and Applications*, edited by E. P. Namburi, R. J. H. Wanhill, and D. K. Setua (Springer Nature Singapore, 2024),
DOI: 10.1007/978-981-99-9791-6_3.

[41] C. De Mello Donega, *Nanoparticles: Workhorses of Nanoscience*, 2nd ed. (Springer Cham, 2024),
DOI: 10.1007/978-3-031-71460-3.

[42] H. Fröhlich, "Die spezifische wärme der elektronen kleiner metallteilchen bei tiefen temperaturen", Physica **4**, 406 (1937)
DOI: 10.1016/S0031-8914(37)80143-3.

[43] A. I. Ekimov, A. L. Efros, and A. A. Onushchenko, "Quantum size effect in semiconductor microcrystals", Solid State Communications **56**, 921 (1985)
DOI: 10.1016/S0038-1098(85)80025-9.

[44] R. Rossetti, S. Nakahara, and L. E. Brus, "Quantum size effects in the redox potentials, resonance Raman spectra, and electronic spectra of CdS crystallites in aqueous solution", The Journal of Chemical Physics **79**, 1086 (1983)
DOI: 10.1063/1.445834.

[45] C. B. Murray, D. J. Norris, and M. G. Bawendi, "Synthesis and characterization of nearly monodisperse CdE (E = sulfur, selenium, tellurium) semiconductor nanocrystallites", Journal of the American Chemical Society **115**, 8706 (1993)
DOI: 10.1021/ja00072a025.

[46] H. Jung, N. Ahn, and V. Klimov, "Prospects and challenges of colloidal quantum dot laser diodes", Nature Photonics **15**, 643 (2021)
DOI: 10.1038/s41566-021-00827-6.

[47] Y. Shu, X. Lin, H. Qin, Z. Hu, Y. Jin, and X. Peng, "Quantum Dots for Display Applications", Angewandte Chemie **132**, 22496 (2020)
DOI: 10.1002/ange.202004857.

[48] P. S. Grigoryev, V. V. Belykh, D. R. Yakovlev, E. Lhuillier, and M. Bayer, "Coherent Spin Dynamics of Electrons and Holes in $CsPbBr_3$ Colloidal Nanocrystals", Nano Letters **21**, 8481 (2021)
DOI: 10.1021/acs.nanolett.1c03292.

[49] F. Krieg, S. T. Ochsenbein, S. Yakunin, S. ten Brinck, P. Aellen, A. Süess, B. Clerc, D. Guggisberg, O. Nazarenko, Y. Shynkarenko, S. Kumar, C.-J. Shih, I. Infante, and M. V. Kovalenko, "Colloidal $CsPbX_3$ (X = Cl, Br, I) Nanocrystals 2.0: Zwitterionic Capping Ligands for Improved Durability and Stability", ACS Energy Letters **3**, 641 (2018)
DOI: 10.1021/acsenergylett.8b00035.

[50] E. Kolobkova, M. Kuznetsova, and N. Nikonorov, "Perovskite $CsPbX_3$ (X=Cl, Br, I) Nanocrystals in fluorophosphate glasses", Journal of Non-Crystalline Solids **563**, 120811 (2021)
DOI: 10.1016/j.jnoncrysol.2021.120811.

[51] S. R. Meliakov, V. V. Belykh, E. A. Zhukov, E. V. Kolobkova, M. S. Kuznetsova, M. Bayer, and D. R. Yakovlev, "Hole spin precession and dephasing induced by nuclear hyperfine fields in $CsPbBr_3$ and $CsPb(Cl,Br)_3$ nanocrystals in a glass matrix", Physical Review B **110**, 235301 (2024)
DOI: 10.1103/PhysRevB.110.235301.

[52] J. Wang, J. Zhang, Y. Zhou, H. Liu, Q. Xue, X. Li, C.-C. Chueh, H.-L. Yip, Z. Zhu, and A. K. Y. Jen, "Highly efficient all-inorganic perovskite solar cells with suppressed non-radiative recombination by a Lewis base", Nature Communications **11**, 177 (2020)
DOI: 10.1038/s41467-019-13909-5.

[53] Y. Ye, W. Zhang, Z. Zhao, J. Wang, C. Liu, Z. Deng, X. Zhao, and J. Han, "Highly Luminescent Cesium Lead Halide Perovskite Nanocrystals Stabilized in Glasses for Light-Emitting Applications", Advanced Optical Materials **7**, 1801663 (2019)
DOI: 10.1002/adom.201801663.

[54] S. Liu, M. He, X. Di, P. Li, W. Xiang, and X. Liang, "Precipitation and tunable emission of cesium lead halide perovskites ($CsPbX_3$, X = Br, I) QDs in borosilicate glass", Ceramics International **44**, 4496 (2018)
DOI: 10.1016/j.ceramint.2017.12.012.

[55] E. V. Kulebyakina, M. L. Skorikov, E. V. Kolobkova, M. S. Kuznetsova, M. N. Bataev, D. R. Yakovlev, and V. V. Belykh, "Temperature-dependent photoluminescence dynamics of $CsPbBr_3$ and $CsPb(Cl,Br)_3$ perovskite nanocrystals in a glass matrix", Physical Review B **109**, 235301 (2024)
DOI: 10.1103/PhysRevB.109.235301.

[56] D. Canneson, E. V. Shornikova, D. R. Yakovlev, T. Rogge, A. A. Mitioglu, M. V. Ballottin, P. C. M. Christianen, E. Lhuillier, M. Bayer, and L. Biadala, "Negatively Charged and Dark Excitons in $CsPbBr_3$ Perovskite Nanocrystals Revealed by High Magnetic Fields", Nano Letters **17**, 6177 (2017)
DOI: 10.1021/acs.nanolett.7b02827.

[57] S. R. Meliakov, E. A. Zhukov, V. V. Belykh, M. O. Nestoklon, E. V. Kolobkova, M. S. Kuznetsova, M. Bayer, and D. R. Yakovlev, "Temperature dependence of the electron and hole Landé g-factors in $CsPbI_3$ nanocrystals embedded in a glass matrix", Nanoscale **16**, 21496 (2024)
DOI: 10.1039/D4NR03132F.

[58] M. O. Nestoklon, E. Kirstein, D. R. Yakovlev, E. A. Zhukov, M. M. Glazov, M. A. Semina, E. L. Ivchenko, E. V. Kolobkova, M. S. Kuznetsova, and M. Bayer, "Tailoring the Electron and Hole Landé Factors in Lead Halide Perovskite Nanocrystals by Quantum Confinement and Halide Exchange", Nano Letters **23**, 8218 (2023)
DOI: 10.1021/acs.nanolett.3c02349.

[59] T. Nakaoka, T. Saito, J. Tatebayashi, and Y. Arakawa, "Size, shape, and strain dependence of the g factor in self-assembled In(Ga)As quantum dots", Physical Review B **70**, 235337 (2004)
DOI: 10.1103/PhysRevB.70.235337.

[60] M. T. Björk, A. Fuhrer, A. E. Hansen, M. W. Larsson, L. E. Fröberg, and L. Samuelson, "Tunable effective g factor in InAs nanowire quantum dots", Physical Review B **70**, 201307 (2005)
DOI: 10.1103/PhysRevB.72.201307.

[61] E. L. Ivchenko, *Optical Spectroscopy of Semiconductor Nanostructures*, ISBN: 978-1842651506 (Alpha Science, 2005).

[62] E. Kirstein, D. R. Yakovlev, M. M. Glazov, E. A. Zhukov, D. Kudlacik, I. V. Kalitukha, V. F. Sapega, G. S. Dimitriev, M. A. Semina, M. O. Nestoklon, E. L. Ivchenko, N. E. Kopteva, D. N. Dirin, O. Nazarenko, M. V. Kovalenko, A. Baumann, J. Höcker, V. Dyakonov, and M. Bayer, "The Lande factors of electrons and holes in lead halide perovskites: universal dependence on the band gap", Nature Communications **13**, 3062 (2022)
DOI: 10.1038/s41467-022-30701-0.

[63] V. M. Goldschmidt, "Die Gesetze der Krystallochemie", Naturwissenschaften **14**, 477 (1926)
DOI: 10.1007/BF01507527.

[64] M. Kim, A. Alfano, G. Perotto, M. Serri, N. Dengo, A. Mezzetti, S. Gross, M. Prato, M. Salerno, A. Rizzo, R. Sorrentino, E. Cescon, G. Meneghesso, F. Di Fonzo, A. Petrozza, T. Gatti, and F. Lamberti, "Moisture resistance in perovskite solar cells attributed to a water-splitting layer", Communications Materials **2**, 6 (2021)
DOI: 10.1038/s43246-020-00104-z.

[65] J. Li, H.-L. Cao, W.-B. Jiao, Q. Wang, M. Wei, I. Cantone, J. Lü, and A. Abate, "Biological impact of lead from halide perovskites reveals the risk of introducing a safe threshold", Nature Communications **11**, 310 (2020)
DOI: 10.1038/s41467-019-13910-y.

[66] E. Kirstein, N. E. Kopteva, D. R. Yakovlev, E. A. Zhukov, E. V. Kolobkova, M. S. Kuznetsova, V. V. Belykh, I. A. Yugova, M. M. Glazov, M. Bayer, and A. Greilich, "Mode locking of hole spin coherences in $CsPb(Cl, Br)_3$ perovskite nanocrystals", Nature Communications **14**, 699 (2023)
DOI: 10.1038/s41467-023-36165-0.

[67] V. I. Korepanov, S.-Y. Chan, H.-C. Hsu, and H.-o. Hamaguchi, "Phonon confinement and size effect in Raman spectra of ZnO nanoparticles", Heliyon **5**, e01222 (2019)
DOI: 10.1016/j.heliyon.2019.e01222.

[68] L. Saviot, B. Champagnon, E. Duval, I. A. Kudriavtsev, and A. I. Ekimov, "Size dependence of acoustic and optical vibrational modes of CdSe nanocrystals in glasses", Journal of Non-Crystalline Solids **197**, 238 (1996)
DOI: 10.1016/0022-3093(96)00164-0.

[69] L. Saviot, B. Champagnon, E. Duval, and A. I. Ekimov, "Size-selective resonant Raman scattering in CdS doped glasses", Physical Review B **57**, 341 (1998)
DOI: 10.1103/PhysRevB.57.341.

[70] S. V. Goupalov and I. A. Merkulov, "Confinement of Acoustic Phonons in CuCl Nanocrystal Quantum Dots", Physica Status Solidi b **224**, 649 (2001)
DOI: 10.1002/(SICI)1521-3951(200104)224:3<649::AID-PSSB649>3.0.CO;2-Y.

[71] M. Ikezawa, T. Okuno, Y. Masumoto, and A. A. Lipovskii, "Complementary detection of confined acoustic phonons in quantum dots by coherent phonon measurement and Raman scattering", Physical Review B **64**, 201315 (2001)
DOI: 10.1103/PhysRevB.64.201315.

[72] E. Kirstein, E. A. Zhukov, D. R. Yakovlev, N. E. Kopteva, C. Harkort, D. Kudlacik, O. Hordiichuk, M. V. Kovalenko, and M. Bayer, "Coherent Spin Dynamics of Electrons in Two-Dimensional $(PEA)_2PbI_4$ Perovskites", Nano Letters **23**, 205 (2023)
DOI: 10.1021/acs.nanolett.2c03975.

[73] D. Kudlacik, N. E. Kopteva, M. Kotur, D. R. Yakovlev, K. V. Kavokin, C. Harkort, M. Karzel, E. A. Zhukov, E. Evers, V. V. Belykh, and M. Bayer, "Optical Spin Orientation of Localized Electrons and Holes Interacting with Nuclei in a $FA_{0.9}Cs_{0.1}PbI_{2.8}Br_{0.2}$ Perovskite Crystal", ACS Photonics **11**, 2757 (2024)
DOI: 10.1021/acsphotonics.4c00637.

[74] C. Harkort, I. V. Kalitukha, D. Kudlacik, N. E. Kopteva, D. R. Yakovlev, B. Turedi, D. N. Dirin, M. V. Kovalenko, and M. Bayer, "Spin-flip Raman scattering on electrons and holes in $MAPbI_3$ single crystals", In preparation (2025).

[75] C. Harkort, I. V. Kalitukha, N. E. Kopteva, M. O. Nestoklon, L. S. Goupalov, L. Saviot, D. Kudlacik, D. R. Yakovlev, E. V. Kolobkova, M. S. Kuznetsova, and M. Bayer, "Optically-active confined acoustic phonons in $CsPbI_3$ nanocrystals explored by resonant Raman scattering", Submitted (2025).

[76] M. Fox, *Optical properties of solids*, 2nd ed. ISBN: 978–0–19–957336–3 (Oxford University Press, 2010).

[77] C. F. Klingshirn, *Semiconductor optics*, 4th ed. (Springer Berlin, Heidelberg, 2012),
DOI: 10.1007/978-3-642-28362-8.

[78] S. Grisard, "From spectroscopy to coherent control: photon echoes of excitons in organic-inorganic perovskites and (In, Ga)As quantum dots", Dissertation (TU Dortmund University, 2023),
DOI: 10.17877/DE290R-24148.

[79] W. G. Zeier, A. Zevalkink, Z. M. Gibbs, G. Hautier, M. G. Kanatzidis, and G. J. Snyder, "Thinking Like a Chemist: Intuition in Thermoelectric Materials", Angewandte Chemie **55**, 6826 (2016)
DOI: 10.1002/anie.201508381.

[80] F. Brivio, K. T. Butler, A. Walsh, and M. van Schilfgaarde, "Relativistic quasiparticle self-consistent electronic structure of hybrid halide perovskite photovoltaic absorbers", Physical Review B **89**, 155204 (2014)
DOI: 10.1103/PhysRevB.89.155204.

[81] K. Momma and F. Izumi, "VESTA3 for three-dimensional visualization of crystal, volumetric and morphology data", Journal of Applied Crystallography **44**, 1272 (2011)
DOI: 10.1107/S0021889811038970.

[82] S. Gražulis, D. Chateigner, R. T. Downs, A. F. T. Yokochi, M. Quirós, L. Lutterotti, E. Manakova, J. Butkus, P. Moeck, and A. Le Bail, "Crystallography Open Database – an open-access collection of crystal structures", Journal of Applied Crystallography **42**, 726 (2009)
DOI: 10.1107/S0021889809016690.

[83] R. Prasanna, A. Gold-Parker, T. Leijtens, B. Conings, A. Babayigit, H.-G. Boyen, M. F. Toney, and M. D. McGehee, "Band Gap Tuning via Lattice Contraction and Octahedral Tilting in Perovskite Materials for Photovoltaics", Journal of the American Chemical Society **139**, 11117 (2017)
DOI: 10.1021/jacs.7b04981.

[84] R. E. Brandt, V. Stevanović, D. S. Ginley, and T. Buonassisi, "Identifying defect-tolerant semiconductors with high minority-carrier lifetimes: beyond hybrid lead halide perovskites", MRS Communications **5**, 265 (2015)
DOI: 10.1557/mrc.2015.26.

[85] J. E. Kirstein, "Coherent spin dynamics and carrier-nuclear interaction in lead halide perovskite crystals", Dissertation (TU Dortmund University, 2022),
DOI: 10.17877/DE290R-22888.

[86] P. Y. Yu and M. Cardona, *Fundamentals of Semiconductors - Physics and Materials Properties*, 4th ed. (Springer Berlin, Heidelberg, 2010),
DOI: 10.1007/978-3-642-00710-1.

[87] M. I. Dyakonov, *Spin Physics in Semiconductors*, 1st ed. (Springer Berlin, Heidelberg, 2017),
DOI: 10.1007/978-3-540-78820-1.

[88] S. Boyer-Richard, C. Katan, B. Traoré, R. Scholz, J.-M. Jancu, and J. Even, "Symmetry-Based Tight Binding Modeling of Halide Perovskite Semiconductors", Journal of Physical Chemistry Letters **7**, 3833 (2016)
DOI: 10.1021/acs.jpclett.6b01749.

[89] B. Sutherland and E. Sargent, "Perovskite photonic sources", Nature Photonics **10**, 295 (2016)
DOI: 10.1038/nphoton.2016.62.

[90] S. Tao, I. Schmidt, G. Brocks, J. Jiang, I. Tranca, K. Meerholz, and S. Olthof, "Nature Communications", Absolute energy level positions in tin- and lead-based halide perovskites **10**, 2560 (2019)
DOI: 10.1038/s41467-019-10468-7.

[91] F. F. Targhi, Y. S. Jalili, and F. Kanjouri, "$MAPbI_3$ and $FAPbI_3$ perovskites as solar cells: Case study on structural, electrical and optical properties", Results in Physics **10**, 616 (2018)
DOI: 10.1016/j.rinp.2018.07.007.

[92] A. M. Glazer, "Simple ways of determining perovskite structures", Acta Crystallographica Section A: Foundations of Crystallography (Formerly: Crystal Physics, Diffraction, Theoretical and General Crystallography) **31**, 756 (1975)
DOI: 10.1107/S0567739475001635.

[93] S. Schryver and A. Lamichhane, "Temperature-driven structural phase transitions in $CsPbBr_3$", Solid State Communications **371**, 115237 (2023)
DOI: 10.1016/j.ssc.2023.115237.

[94] C. C. Stoumpos and M. G. Kanatzidis, "The Renaissance of Halide Perovskites and Their Evolution as Emerging Semiconductors", Accounts of Chemical Research **48**, 2791 (2015)
DOI: 10.1021/acs.accounts.5b00229.

[95] C. C. Stoumpos, C. D. Malliakas, and M. G. Kanatzidis, "Semiconducting Tin and Lead Iodide Perovskites with Organic Cations: Phase Transitions, High Mobilities, and Near-Infrared Photoluminescent Properties", Inorganic Chemistry **52**, 9019 (2013)
DOI: 10.1021/ic401215x.

[96] Z. Li, M. Yang, J.-S. Park, S.-H. Wei†, J. J. Berry, and K. Zhu, "Stabilizing Perovskite Structures by Tuning Tolerance Factor: Formation of Formamidinium and Cesium Lead Iodide Solid-State Alloys", Chemistry of Materials **28**, 284 (2016)
DOI: 10.1021/acs.chemmater.5b04107.

[97] T. Oku, "Crystal structures of perovskite halide compounds used for solar cells", Reviews on Advanced Materials Science **59**, 264 (2020)
DOI: 10.1515/rams-2020-0015.

[98] M. Bayer, G. Ortner, O. Stern, A. Kuther, A. A. Gorbunov, A. Forchel, P. Hawrylak, S. Fafard, K. Hinzer, T. L. Reinecke, S. N. Walck, J. P. Reithmaier, F. Klopf, and F. Schäfer, "Fine structure of neutral and charged excitons in self-assembled In(Ga)As/(Al)GaAs quantum dots", Physical Review B **65**, 195315 (2002)
DOI: 10.1103/PhysRevB.65.195315.

[99] P. Tamarat, M. I. Bodnarchuk, J.-B. Trebbia, R. Erni, M. V. Kovalenko, J. Even, and B. Lounis, "The ground exciton state of formamidinium lead bromide perovskite nanocrystals is a singlet dark state", Nature Materials **18**, 717 (2019)
DOI: 10.1038/s41563-019-0364-x.

[100] M. Fu, P. Tamarat, H. Huang, J. Even, A. L. Rogach, and B. Lounis, "Neutral and Charged Exciton Fine Structure in Single Lead Halide Perovskite Nanocrystals Revealed by Magneto-optical Spectroscopy", Nano Letters **17**, 2895 (2017)
DOI: 10.1021/acs.nanolett.7b00064.

[101] M. A. Becker, R. Vaxenburg, G. Nedelcu, P. C. Sercel, A. Shabaev, M. J. Mehl, J. G. Michopoulos, S. G. Lambrakos, N. Bernstein, J. L. Lyons, T. Stöferle, R. F. Mahrt, M. V. Kovalenko, D. J. Norris, G. Rainò, and A. L. Efros, "Bright triplet excitons in caesium lead halide perovskites", Nature **553**, 189 (2018)
DOI: 10.1038/nature25147.

[102] L. N. Quan, M. Yuan, R. Comin, O. Voznyy, E. M. Beauregard, S. Hoogland, A. Buin, A. R. Kirmani, K. Zhao, A. Amassian, D. H. Kim, and E. H. Sargent, "Ligand-Stabilized Reduced-Dimensionality Perovskites", Journal of the American Chemical Society **138**, 2649 (2016)
DOI: 10.1021/jacs.5b11740.

[103] L. Mao, C. C. Stoumpos, and M. G. Kanatzidis, "Two-Dimensional Hybrid Halide Perovskites: Principles and Promises", Journal of the American Chemical Society **141**, 1171 (2018)
DOI: 10.1021/jacs.8b10851.

[104] X. Gao, X. Zhang, W. Yin, H. Wang, Y. Hu, Q. Zhang, Z. Shi, V. L. Colvin, W. W. Yu, and Y. Zhang, "Ruddlesden–Popper Perovskites: Synthesis and Optical Properties for Optoelectronic Applications", Advanced Science **6**, 1900941 (2019)
DOI: 10.1002/advs.201900941.

[105] Y.-Q. Zhao, Q.-R. Ma, B. Liu, Z.-L. Yu, J. Yang, and M.-Q. Cai, "Layer-dependent transport and optoelectronic property in two-dimensional perovskite: $(PEA)_2PbI_4$", Nanoscale **10**, 8677 (2018)
DOI: 10.1039/C8NR00997J.

[106] M. Baranowski, M. Dyksik, and P. Plochocka, "2D Metal Halide Perovskites: A New Fascinating Playground for Exciton Fine Structure Investigations", Scientiae Radices **1**, 3 (2022)
DOI: 10.58332/v22i1a01.

[107] A. Hafaiedh and N. Bouarissa, "Quantum confinement effects on energy gaps and electron and hole effective masses of quantum well AlN", Physica E: Low-dimensional Systems and Nanostructures **43**, 1638 (2011)
DOI: 10.1016/j.physe.2011.05.013.

[108] X. Hong, T. Ishihara, and A. V. Nurmikko, "Dielectric confinement effect on excitons in PbI_4-based layered semiconductors", Physical Review B **45**, 6961 (1992)
DOI: 10.1103/PhysRevB.45.6961.

[109] B. Cheng, T.-Y. Li, P. Maity, P.-C. Wei, D. Nordlund, K.-T. Ho, D.-H. Lien, C.-H. Lin, R.-Z. Liang, X. Miao, I. A. Ajia, J. Yin, D. Sokaras, A. Javey, I. S. Roqan, O. F. Mohammed, and J.-H. He, "Extremely reduced dielectric confinement in two-dimensional hybrid perovskites with large polar organics", Communications Physics **1**, 80 (2018)
DOI: 10.1038/s42005-018-0082-8.

[110] K. Galkowski, A. Mitioglu, A. Miyata, P. Plochocka, O. Portugall, G. E. Eperon, J. T.-W. Wang, T. Stergiopoulos, S. D. Stranks, H. J. Snaith, and R. J. Nicholas, "Determination of the exciton binding energy and effective masses for methylammonium and formamidinium lead tri-halide perovskite semiconductors", Energy & Environmental Science **9**, 962 (2016)
DOI: 10.1039/C5EE03435C.

[111] J. Lin, L. Gomez, C. de Weerd, Y. Fujiwara, T. Gregorkiewicz, and K. Suenaga, "Direct Observation of Band Structure Modifications in Nanocrystals of $CsPbBr_3$ Perovskite", Nano Letters **16**, 7198 (2016)
DOI: 10.1021/acs.nanolett.6b03552.

[112] H. Fu, L.-W. Wang, and A. Zunger, "Excitonic exchange splitting in bulk semiconductors", Physical Review B **59**, 5568 (1999)
DOI: 10.1103/PhysRevB.59.5568.

[113] M. Dyksik, H. Duim, D. K. Maude, M. Baranowski, M. A. Loi, and P. Plochocka, "Brightening of dark excitons in 2D perovskites", Science Advances **7**, eabk0904 (2021)
DOI: 10.1126/sciadv.abk0904.

[114] R. Ben Aich, I. Saïdi, S. Ben Radhia, K. Boujdaria, T. Barisien, L. Legrand, F. Bernardot, M. Chamarro, and C. Testelin, "Bright-Exciton Splittings in Inorganic Cesium Lead Halide Perovskite Nanocrystals", Physical Review Applied **11**, 034042 (2019)
DOI: 10.1103/PhysRevApplied.11.034042.

[115] N. E. Kopteva, D. R. Yakovlev, E. Yalcin, I. A. Akimov, M. O. Nestoklon, M. M. Glazov, M. Kotur, D. Kudlacik, E. A. Zhukov, E. Kirstein, O. Hordiichuk, D. N. Dirin, M. V. Kovalenko, and M. Bayer, "Highly-Polarized Emission Provided by Giant Optical Orientation of Exciton Spins in Lead Halide Perovskite Crystals", Advanced Science **11**, 2403691 (2024)
DOI: 10.1002/advs.202403691.

[116] F. Meier and B. Zakharchenya, *Modern Problems in Condensed Matter Sciences - Optical Orientation*, 1st ed. (Elsevier, 1984).

[117] M. M. Glazov, *Electron and Nuclear Spin Dynamics in Semiconductor Nanostructures* (Oxford University Press, 2018),
DOI: 10.1093/oso/9780198807308.001.0001.

[118] J. A. Steele, M. Lai, Y. Zhang, Z. Lin, J. Hofkens, M. B. J. Roeffaers, and P. Yang, "Phase Transitions and Anion Exchange in All-Inorganic Halide Perovskites", Accounts of Materials Research **1**, 3 (2020)
DOI: 10.1021/accountsmr.0c00009.

[119] C. Weisbuch and C. Hermann, "Optical detection of conduction-electron spin resonance in GaAs, $Ga_{1-x}In_xAs$, and $Ga_{1-x}Al_xAs$", Physical Review B **15**, 816 (1977)
DOI: 10.1103/PhysRevB.15.816.

[120] B. Odom, D. Hanneke, B. D'Urso, and G. Gabrielse, "Physical Review Letters", New Measurement of the Electron Magnetic Moment Using a One-Electron Quantum Cyclotron **97**, 030801 (2006)
DOI: 10.1103/PhysRevLett.97.030801.

[121] L. M. Roth, B. Lax, and S. Zwerdling, "Theory of Optical Magneto-Absorption Effects in Semiconductors", Physical Review **114**, 90 (1959)
DOI: 10.1103/PhysRev.114.90.

[122] Z. G. Yu, "Effective-mass model and magneto-optical properties in hybrid perovskites", Scientific Reports **6**, 28576 (2016)
DOI: 10.1038/srep28576.

[123] K. Cho, *Excitons*, 1st ed. (Springer Berlin, Heidelberg, 1979),
DOI: 10.1007/978-3-642-81368-9.

[124] I. A. Yugova, A. Greilich, D. R. Yakovlev, A. A. Kiselev, M. Bayer, V. V. Petrov, Y. K. Dolgikh, D. Reuter, and A. D. Wieck, "Universal behavior of the electron g factor in $GaAs/Al_xGa_{1-x}As$ quantum wells", Physical Review B **75**, 245302 (2007)
DOI: 10.1103/PhysRevB.75.245302.

[125] N. E. Kopteva, D. R. Yakovlev, E. Kirstein, E. A. Zhukov, D. Kudlacik, I. V. Kalitukha, V. F. Sapega, O. Hordiichuk, D. N. Dirin, M. V. Kovalenko, A. Baumann, J. Höcker, V. Dyakonov, S. A. Crooker, and M. Bayer, "Weak Dispersion of Exciton Landé Factor with Band Gap Energy in Lead Halide Perovskites: Approximate Compensation of the Electron and Hole Dependences", Small **20**, 2300935 (2024)
DOI: 10.1002/smll.202300935.

[126] A. Abragam, *The principles of Nuclear Magnetism*, ISBN: 9780198520146 (Oxford Science Publications, 1983).

[127] E. Chekhovich, M. Glazov, A. Krysa, M. Hopkinson, P. Senellart, A. Lemaître, M. S. Skolnick, and A. I. Tartakovskii, "Element-sensitive measurement of the hole–nuclear spin interaction in quantum dots", Nature Physics **9**, 74 (2013)
DOI: 10.1038/nphys2514.

[128] G. P. Srivastava, *The Physics of Phonons*, 2nd ed. (CRC Press, 2022), DOI: 10.1201/9781003141273.

[129] M. Cardona, *Phonons in Superlattices* (Springer, Boston, MA, 1989), DOI: 10.1007/978-1-4757-6565-6_8.

[130] H. K. Yadav, V. Gupta, K. Sreenivas, S. P. Singh, B. Sundarakannan, and R. S. Katiyar, "Low Frequency Raman Scattering from Acoustic Phonons Confined in ZnO Nanoparticles", Physical Review Letters **97**, 085502 (2006) DOI: 10.1103/PhysRevLett.97.085502.

[131] C. M. Iaru, J. J. Geuchies, P. M. Koenraad, D. Vanmaekelbergh, and A. Y. Silov, "Strong Carrier–Phonon Coupling in Lead Halide Perovskite Nanocrystals", ACS Nano **11**, 11024 (2017) DOI: 10.1021/acsnano.7b05033.

[132] M. C. Klein, F. Hache, D. Ricard, and C. Flytzanis, "Size dependence of electron-phonon coupling in semiconductor nanospheres: The case of CdSe", Physical Review B **42**, 11123 (1990) DOI: 10.1103/PhysRevB.42.11123.

[133] X. Ma, P. Shen, Y.-N. Wang, F. Pan, G. Chen, S. Xu, and H. Ye, "Local Phonon Modes Concerned with the Self-Trapped Exciton State in $CsPbBr_3$ Nanocrystals", The Journal of Physical Chemistry C **124**, 27130 (2020) DOI: 10.1021/acs.jpcc.0c07879.

[134] T. D. Krauss and F. W. Wise, "Coherent Acoustic Phonons in a Semiconductor Quantum Dot", Physical Review Letters **79**, 5102 (1997) DOI: 10.1103/PhysRevLett.79.5102.

[135] L. Kimerling, K. Kolenbrander, J. Michel, and J. Palm, *Light Emission from Silicon*, edited by H. Ehrenreich and F. Spaepen, Solid State Physics (Academic Press, 1996), pp. 333–381, DOI: 10.1016/S0081-1947(08)60606-2.

[136] R. Gross and A. Marx, *Festkörperphysik*, 2nd ed. (De Gruyter, 2014), DOI: 10.1524/9783110358704.

[137] A. Orlando, F. Franceschini, C. Muscas, S. Pidkova, M. Bartoli, M. Rovere, and A. Tagliaferro, "A Comprehensive Review on Raman Spectroscopy Applications", Chemosensors **9**, 262 (2021) DOI: 10.3390/chemosensors9090262.

[138] J. Toporski, T. Dieing, and O. Hollricher, *Confocal Raman Microscopy*, 2nd ed. (Springer Cham, 2018), DOI: 10.1007/978-3-319-75380-5.

[139] E. Smith and G. Dent, *Modern Raman Spectroscopy: A Practical Approach*, 2nd ed. (John Wiley & Sons Ltd., 2019), DOI: 10.1002/9781119440598.

[140] W. Hayes and R. Loudon, *Scattering of Light by Crystals*, ISBN: 9780486161471 (John Wiley & Sons Inc, 2012).

[141] V. I. Korepanov, "Localized phonons in Raman spectra of nanoparticles and disordered media", Journal of Raman spectroscopy **51**, 881 (2020) DOI: 10.1002/jrs.5815.

[142] V. V. Belykh, D. R. Yakovlev, M. M. Glazov, P. S. Grigoryev, M. Hussain, J. Rautert, D. N. Dirin, M. V. Kovalenko, and M. Bayer, "Coherent spin dynamics of electrons and holes in $CsPbBr_3$ perovskite crystals", Nature Communications **10**, 673 (2019)
DOI: 10.1038/s41467-019-08625-z.

[143] E. Kirstein, D. R. Yakovlev, E. A. Zhukov, J. Höcker, V. Dyakonov, and M. Bayer, "Spin Dynamics of Electrons and Holes Interacting with Nuclei in $MAPbI_3$ Perovskite Single Crystals", ACS Photonics **9**, 1375 (2022)
DOI: 10.1021/acsphotonics.2c00096.

[144] A. Rodina and E. Ivchenko, "Theory of acoustic-phonon involved exciton spin flip in perovskite semiconductors", Journal of Luminescence **272**, 120640 (2024)
DOI: 10.1016/j.jlumin.2024.120640.

[145] M. Nawrocki, R. Planel, G. Fishman, and R. Galazka, "Exchange-Induced Spin-Flip Raman Scattering in a Semimagnetic Semiconductor", Physical Review Letters **46**, 735 (1981)
DOI: 10.1103/PhysRevLett.46.735.

[146] A. V. Rodina and E. L. Ivchenko, "Theory of single and double electron spin-flip Raman scattering in semiconductor nanoplatelets", Physical Review B **102**, 235432 (2020)
DOI: 10.1103/PhysRevB.102.235432.

[147] D. Kudlacik, K. V. Kavokin, C. Lüders, K. Barthelmi, J. J. Schindler, H. Moldenhauer, P. Waldkirch, V. F. Sapega, D. R. Yakovlev, A. Waag, M. Bayer, and J. Debus, "Asymmetric spin transitions of nonthermalized Mn^{2+} ions in (Zn,Mn)Se-based quantum well", Physical Review B **101**, 155432 (2020)
DOI: 10.1103/PhysRevB.101.155432.

[148] H. A. Kramers and W. Heisenberg, "Über die Streuung von Strahlung durch Atome", Zeitschrift für Physik **31**, 681 (1925)
DOI: 10.1007/BF02980624.

[149] *Operating Instructions Acton Series SP-2500i*, http://ridl.cfd.rit.edu/products/manuals/Princeton%20Acton/SP-2500i.pdf.

[150] *MCS6A 5(6) Input 100ps Multi-stop TDC, Multiscaler, Time-Of-Flight User Manual*, (2019) https://www.fastcomtec.com/ftp/manuals/mcs6adoc.pdf.

[151] Thorlabs, *Noise Eaters / Laser Amplitude Stabilizers*, (2021) https://www.thorlabs.com/drawings/4a31cc64b8d53b7-4077BA7A-C5C9-231B-DB0CD0B990D552A7/NEL01A_M-Manual.pdf.

[152] M. N. Polyanskiy, "Refractiveindex.info database of optical constants", Sci. Data **11**, 94 (2024)
DOI: 10.1038/s41597-023-02898-2.

[153] M. Ahmad, G. Rehman, L. Ali, M. Shafiq, R. Iqbal, R. Ahmad, T. Khan, S. Jalali-Asadabadi, M. Maqbool, and I. Ahmad, "Structural, electronic and optical properties of $CsPbX_3$ (X=Cl, Br, I) for energy storage and hybrid solar cell applications", Journal of Alloys and Compounds **705**, 828 (2017)
DOI: 10.1016/j.jallcom.2017.02.147.

[154] R. Petit, *Electromagnetic Theory of Gratings*, 1st ed. (Springer Berlin, Heidelberg, 1980),
DOI: 10.1007/978-3-642-81500-3.

[155] *Technical Manual - Spectrometer Horiba Jobin-Yvon U1000*, (2011)

[156] D. Kudlacik, "Characterization of semiconductor nanostructures by spin-flip Raman spectroscopy", Dissertation (TU Dortmund University, 2018),
DOI: 10.17877/DE290R-19122.

[157] Hamamatsu, *Photomultiplier tubes*, https://www.hamamatsu.com/jp/en/product/optical-sensors/pmt/about_pmts.html.

[158] C. Yang, J. Yin, H. Li, K. Almasabi, L. Gutiérrez-Arzaluz, I. Gereige, J.-L. Brédas, O. M. Bakr, and O. F. Mohammed, "Engineering Surface Orientations for Efficient and Stable Hybrid Perovskite Single-Crystal Solar Cells", ACS Energy Letters **7**, 1544 (2022)
DOI: 10.1021/acsenergylett.2c00431.

[159] W. Peng, J. Yin, K.-T. Ho, O. Ouellette, M. De Bastiani, B. Murali, O. E. Tall, C. Shen, X. Miao, J. Pan, E. Alarousu, J.-H. He, B. S. Ooi, O. F. Mohammed, E. Sargent, and O. M. Bakr, "Ultralow Self-Doping in Two-dimensional Hybrid Perovskite Single Crystals", Nano Letters **17**, 4759 (2017)
DOI: 10.1021/acs.nanolett.7b01475.

[160] J. De Roo, M. Ibáñez, P. Geiregat, G. Nedelcu, W. Walravens, J. Maes, J. C. Martins, I. Van Driessche, M. V. Kovalenko, and Z. Hens, "Highly Dynamic Ligand Binding and Light Absorption Coefficient of Cesium Lead Bromide Perovskite Nanocrystals", ACS Nano **10**, 2071 (2016)
DOI: 10.1021/acsnano.5b06295.

[161] S. R. Meliakov, E. A. Zhukov, V. V. Belykh, M. O. Nestoklon, E. V. Kolobkova, M. S. Kuznetsova, M. Bayer, and D. R. Yakovlev, "Landé g-factors of electron and holes strongly confined in $CsPbI_3$ perovskite nanocrystals in glass", arXiv, 2410.11882 (2024)
DOI: 10.48550/arXiv.2410.11882.

[162] L. Protesescu, S. Yakunin, M. I. Bodnarchuk, F. Krieg, R. Caputo, C. H. Hendon, R. X. Yang, A. Walsh, and M. V. Kovalenko, "Nanocrystals of Cesium Lead Halide Perovskites ($CsPbX_3$, X = Cl, Br, and I): Novel Optoelectronic Materials Showing Bright Emission with Wide Color Gamut", Nano Letters **15**, 3692 (2015)
DOI: 10.1021/nl5048779.

[163] N. E. Kopteva, D. R. Yakovlev, E. Yalcin, I. Akimov, M. Kotur, B. Turedi, D. N. Dirin, M. V. Kovalenko, and M. Bayer, "Optical orientation of excitons and charged carriers in $MAPbI_3$ perovskite single crystals in the orthorhombic phase", arXiv, 2502.04902 (2025)
DOI: 10.48550/arXiv.2502.04902.

[164] V. S. Chirvony and J. P. Martínez-Pastor, "Trap-Limited Dynamics of Excited Carriers and Interpretation of the Photoluminescence Decay Kinetics in Metal Halide Perovskites", The Journal of Physical Chemistry Letters **9**, 4955 (2018)
DOI: 10.1021/acs.jpclett.8b01241.

[165] A. Bercegol, F. J. Ramos, A. Rebai, T. Guillemot, D. Ory, J. Rousset, and L. Lombez, "Slow Diffusion and Long Lifetime in Metal Halide Perovskites for Photovoltaics", The Journal of Physical Chemistry C **122**, 24570 (2018)
DOI: 10.1021/acs.jpcc.8b08252.

[166] G. Garcia-Arellano, G. Trippé-Allard, L. Legrand, T. Barisien, D. Garrot, E. Deleporte, F. Bernardot, C. Testelin, and M. Chamarro, "Energy Tuning of Electronic Spin Coherent Evolution in Methylammonium Lead Iodide Perovskites", The Journal of Physical Chemistry Letters **12**, 8272 (2021)
DOI: 10.1021/acs.jpclett.1c01790.

[167] P. Whitfield, N. Herron, W. Guise, K. Page, Y. Q. Cheng, I. Milas, and M. K. Crawford, "Structures, Phase Transitions and Tricritical Behavior of the Hybrid Perovskite Methyl Ammonium Lead Iodide", Scientific Reports **6**, 35685 (2016)
DOI: 10.1038/srep35685.

[168] S. Anghel, A. V. Poshakinskiy, D. R. Yakovlev, E. Kirstein, N. E. Kopteva, O. Hordiichuk, M. V. Kovalenko, M. Bayer, and M. Betz, "Fast Diffusion of Spin Polarized Excitons in Organic–Inorganic Lead Halide Perovskites", ACS Photonics **10**, 4169 (2023)
DOI: 10.1021/acsphotonics.3c00891.

[169] J. Debus, V. F. Sapega, D. Dunker, D. R. Yakovlev, D. Reuter, A. D. Wieck, and M. Bayer, "Spin-flip Raman scattering of the resident electron in singly charged (In,Ga)As/GaAs quantum dot ensembles", Physical Review B **90**, 235404 (2014)
DOI: 10.1103/PhysRevB.90.235404.

[170] J. F. Scott and T. C. Damen, "Anomalous Double Spin-Flip Raman Scattering in CdS, and a Visible Spin-Flip Laser", Physical Review Letters **29**, 107 (1972)
DOI: 10.1103/PhysRevLett.29.107.

[171] Y. Oka and M. Cardona, "Resonant spin-flip Raman scattering on donor and acceptor states in ZnTe", Physical Review B **23**, 4129 (1981)
DOI: 10.1103/PhysRevB.23.4129.

[172] M. D. Smith, B. A. Connor, and H. I. Karunadasa, "Tuning the Luminescence of Layered Halide Perovskites", Chemical Reviews **119**, 3104 (2019)
DOI: 10.1021/acs.chemrev.8b00477.

[173] C. M. M. Soe, G. P. Nagabhushana, R. Shivaramaiah, H. Tsai, W. Nie, J.-C. Blancon, F. Melkonyan, D. H. Cao, B. Traore, L. Pedesseau, M. Kepenekian, C. Katan, J. Even, T. J. Marks, A. Navrotsky, A. D. Mohite, C. C. Stoumpos, and M. G. Kanatzidis, "Structural and thermodynamic limits of layer thickness in 2D halide perovskites", Proceedings of the National Academy of Sciences **116**, 58 (2018)
DOI: 10.1073/pnas.1811006115.

[174] E. S. Vasileiadou, I. Hadar, M. Kepenekian, J. Even, Q. Tu, C. D. Malliakas, D. Friedrich, I. Spanopoulos, J. M. Hoffman, V. P. Dravid, and M. G. Kanatzidis, "Shedding Light on the Stability and Structure–Property Relationships of Two-Dimensional Hybrid Lead Bromide Perovskites", Chemistry of Materials **33**, 5085 (2021)
DOI: 10.1021/acs.chemmater.1c01129.

[175] E. Kirstein, E. A. Zhukov, D. R. Yakovlev, N. E. Kopteva, E. Yalcin, I. A. Akimov, O. Hordiichu, D. N. Dirin, M. V. Kovalenko, and M. Bayer, "Coherent Carrier Spin Dynamics in $FAPbBr_3$ Perovskite Crystals", The Journal of Physical Chemistry Letters **15**, 2893 (2024)
DOI: 10.1021/acs.jpclett.4c00098.

[176] G. Rainò, G. Nedelcu, L. Protesescu, M. I. Bodnarchuk, M. V. Kovalenko, R. F. Mahrt, and T. Stöferle, "Single Cesium Lead Halide Perovskite Nanocrystals at Low Temperature: Fast Single-Photon Emission, Reduced Blinking, and Exciton Fine Structure", ACS Nano **10**, 2485 (2016)
DOI: 10.1021/acsnano.5b07328.

[177] P. C. Sercel, J. L. Lyons, D. Wickramaratne, R. Vaxenburg, N. Bernstein, and A. L. Efros, "Exciton Fine Structure in Perovskite Nanocrystals", Nano Letters **19**, 4068 (2019)
DOI: 10.1021/acs.nanolett.9b01467.

[178] M. O. Nestoklon, "Tight-binding description of inorganic lead halide perovskites in cubic phase", Computational Materials Science **196**, 110535 (2021)
DOI: 10.1016/j.commatsci.2021.110535.

[179] R. Kashikar, B. Khamari, and B. R. K. Nanda, "Second-neighbor electron hopping and pressure induced topological quantum phase transition in insulating cubic perovskites", Physical Review Materials **2**, 124204 (2018)
DOI: 10.1103/PhysRevMaterials.2.124204.

[180] J. Satta, C. Melis, C. M. Carbonaro, A. Pinna, M. Salado, D. Salazar, and P. C. Ricci, "Raman spectra and vibrational analysis of $CsPbI_3$: A fast and reliable technique to identify lead halide perovskite polymorphs", Journal of Materiomics **7**, 127 (2021)
DOI: 10.1016/j.jmat.2020.08.004.

[181] M. Jamal, M. Bilal, I. Ahmad, and S. Jalali-Asadabadi, "IRelast package", Journal of Alloys and Compounds **735**, 569 (2018)
DOI: 10.1016/j.jallcom.2017.10.139.

[182] D. Connétable and O. Thomas, "First-principles study of the structural, electronic, vibrational, and elastic properties of orthorhombic NiS", Physical Review B **79**, 094101 (2009)
DOI: 10.1103/PhysRevB.79.094101.

[183] A. P. Sutton, *Hooke's law and elastic constants*, 1st ed. (Oxford University Press, 2020),
DOI: 10.1093/oso/9780198860785.003.0003.

[184] M. Levy, *Introduction to fundamentals of elastic constants*, edited by M. Levy, H. E. Bass, and R. Stern, Vol. 39 (Academic Press, 2001),
DOI: 10.1016/S1079-4042(01)80084-9.

[185] L. Saviot, "Free Vibrations of Anisotropic Nano-Objects with Rounded or Sharp Corners", Nanomaterials **11**, 1838 (2021)
DOI: 10.3390/nano11071838.

[186] S. V. Goupalov, L. Saviot, and E. Duval, "Comment on "Infrared and Raman selection rules for elastic vibrations of spherical nanoparticles"", Physical Review B **74**, 197401 (2006)
DOI: 10.1103/PhysRevB.74.197401.

[187] L. Saviot and D. B. Murray, "Acoustic vibrations of anisotropic nanoparticles", Physical Review B **79**, 214101 (2009)
DOI: 10.1103/PhysRevB.79.214101.

[188] A. E. J. Hoffman, R. Ali Saha, S. Borgmans, P. Puech, T. Braeckevelt, M. B. J. Roeffaers, J. A. Steele, J. Hofkens, and V. Van Speybroeck, "Understanding the phase transition mechanism in the lead halide perovskite $CsPbBr_3$ via theoretical and experimental GIWAXS and Raman spectroscopy", APL Materials **11**, 041124 (2023)
DOI: 10.1063/5.0144344.

List of Abbreviations

CB conduction band.

CCD charge-coupled device.

DFT density functional theory.

DNP dynamic nuclear polarization.

FWHM full width at half maximum.

GaAs gallium arsenide.

GT Glan-Thompson.

he heavy-electron.

le light-electron.

NC nanocrystal.

NE noise eater.

PEA phenylethylammonium.

PL photoluminescence.

PMT photomultiplier tube.

QW quantum well.

RP Ruddlesdon-Popper.

SF spin-flip.

SFRS spin-flip Raman scattering.

TiSa titan-sapphire.

TRKR time-resolved Kerr rotation.

VB valence band.

List of Symbols

$E_{\mathbf{g}}$ Band gap energy.

μ_B Bohr magneton.

$\sigma^{\pm}$ Circular polarizations.

$E_{\mathbf{exc}}$ Excitation energy.

g Landé g-factor.

$g_{\mathbf{e}}$ Electron Landé g-factor.

$g_{\mathbf{h}}$ Hole Landé g-factor.

$g_{\mathbf{X}}$ Exciton Landé g-factor.

k Wave vector of light.

H/V Linear polarizations (horizontal/vertical).

B Magnetic field.

μ_N Nuclear magneton.

n Number of inorganic layers (lead halide octahedra).

P Power density.

$\Delta_{\mathbf{so}}$ Spin-orbit coupling energy.

T Temperature.

θ Tilt angle.

$\Delta E_{\mathbf{Z}}$ Zeeman energy.

Appendix

A1 2D perovskites - $(PEA)_2FA_{n-1}Pb_nBr_{3n+1}$

Figures A1 to A3 summarize the experimentally determined g-factors for the electron and hole in $(PEA)_2FA_{n-1}Pb_nBr_{3n+1}$. Panel (a) shows the spin-flip Raman scattering (SFRS) spectra for both Faraday and Voigt geometry. The magnetic field dependencies of the observed spin-flips (SFs) are presented in panels (b) and (c), while their anisotropies are displayed in panel (d). The solid lines are fits with Equation 3.12. Note that the experimental parameters are provided in the caption of each figure.

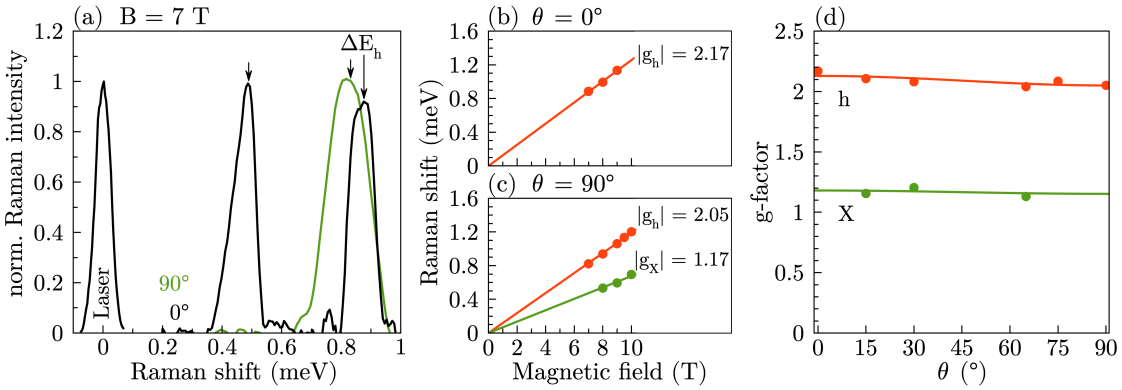

Figure A1: (a) SFRS spectra for $(PEA)_2FAPb_2Br_7$ ($n = 2$) in Faraday ($\theta = 0°$, black) and Voigt geometry ($\theta = 90°$, green) excited with $E_{exc} = 2.812$ eV and $P = 2$ W/cm^2. (b, c) Raman shifts of the SFs lines in magnetic field for hole and exciton in Faraday (b) and Voigt geometry (c). The fit to linear functions (solid lines) allow to determine the carrier g-factors.

According to Section 4.2.1 the g-factor value and anisotropy for excitons and combined SF processes are similar. However, they can be distinguished by their polarization properties. Exciton SFs typically exhibit a polarization dependence [24], whereas combined carrier SF processes do not. As we do not observe pronounced polarization properties in 2D perovskites with SFRS, this suggests that the SF process is most probably associated with a combined one rather than an exciton. However, if the electron SF is not observed in the SFRS spectrum, it is unlikely to detect a combined SF processes involving an electron, as combined SF processes are less probable than single SF processes [37]. Therefore, we attribute the signal to the exciton. Although this distinction is of minor importance as our primary focus is on electron and hole g-factors, as presented in Figure 4.19.

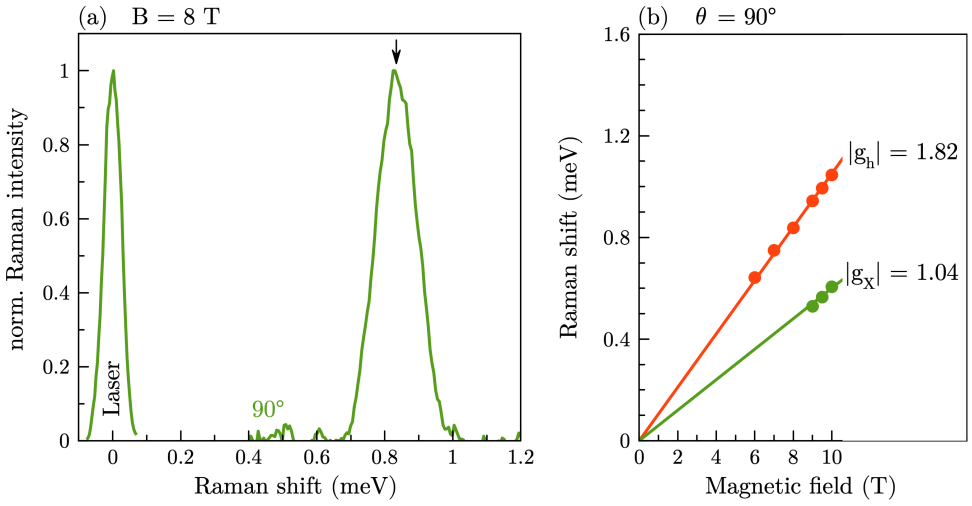

Figure A2: (a) SFRS spectrum for $(PEA)_2FA_2Pb_3Br_{10}$ ($n = 3$) in Voigt geometry ($\theta = 90°$, green) excited with $E_{exc} = 2.60$ eV and $P = 5$ W/cm^2. (b) Raman shifts of the SFs lines in magnetic field for hole and exciton in Voigt geometry. The fit to linear functions (solid lines) allow to determine the carrier g-factors. (d) g-factor anisotropies fitted with Equation 3.12

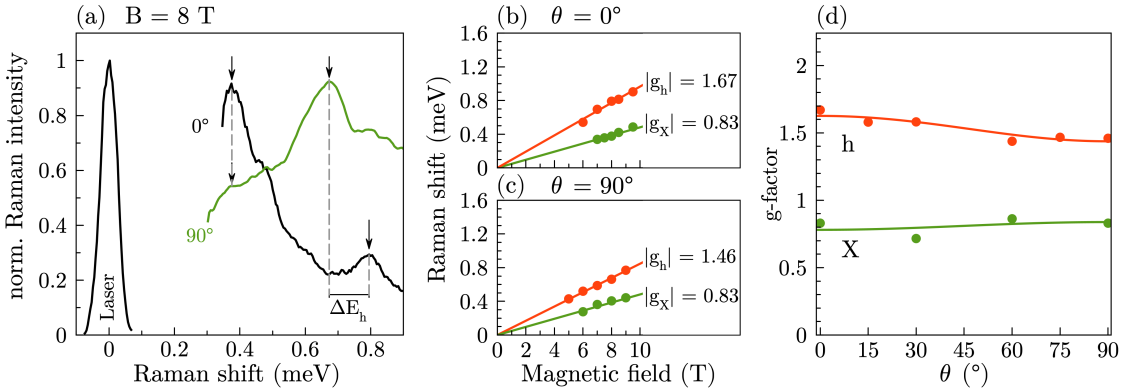

Figure A3: (a) SFRS spectra for $(PEA)_2FA_4Pb_5Br_{16}$ ($n = 5$) in Faraday ($\theta = 0°$, black) and Voigt geometry ($\theta = 90°$, green) excited with $E_{exc} = 2.409$ eV and $P = 2.3$ W/cm^2. (b, c) Raman shifts of the SF lines in magnetic field for hole and exciton in Faraday (b) and Voigt geometry (c). The fit to linear functions (solid lines) allow to determine the carrier g-factors. (d) g-factor anisotropies fitted with Equation 3.12.

A2 2D perovskites - $(PEA)_2(MA)_{n-1}Pb_nI_{3n+1}$

Figures A4 to A8 present the experimental results for SRFS on 2D $(PEA)_2(MA)_{n-1}Pb_nI_{3n+1}$ with n ranging from two to seven. The same representation as in Appendix A1 is used. To enhance the visibility of the SFs, SFRS spectra of tilted field geometries relative to Faraday geometry are selected.

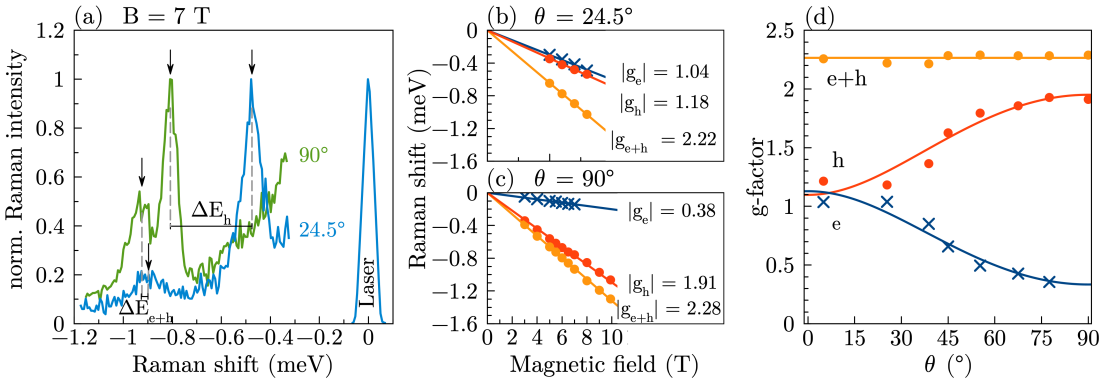

Figure A4: (a) SFRS spectra for $(PEA)_2MAPb_2I_7$ ($n = 2$) in tilted magnetic field ($\theta = 24.5°$, blue) and Voigt geometry ($\theta = 90°$, green) excited with $E_{exc} = 2.132$ eV and $P = 2$ W/cm^2. (b, c) Raman shifts of the SFs lines in magnetic field for the hole and combined carrier in tilted field (b) and Voigt geometry (c). The electron g-factors are calculated from the difference in Raman shift between the combined and hole SFs, as indicated by the crosses. The fit to linear functions (solid lines) allow to determine the carrier g-factors. (d) g-factor anisotropies fitted with Equation 3.12.

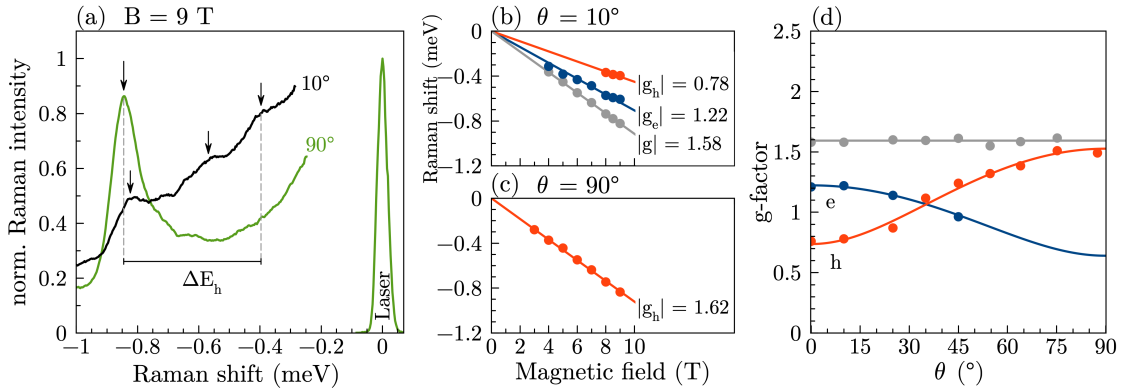

Figure A5: (a) SFRS spectra for $(PEA)_2MA_2Pb_3I_{10}$ ($n = 3$) in close-to-Faraday geometry ($\theta = 10°$, black) and Voigt geometry ($\theta = 90°$, green) at $B = 9$ T excited with $E_{exc} = 1.913$ eV and $P = 0.3$W/cm^2. SFs of electron and hole are indicated for both geometries by vertical arrows, their differences in Raman shifts due to the magnetic field geometry are denoted as ΔE. (b, c) Raman shifts of the SF lines in magnetic field for electron and hole in close-to-Faraday (b) and Voigt geometry (c). The fit to linear functions (solid lines) allow to determine the carrier g-factors. (d) g-factor anisotropies fitted with Equation 3.12.

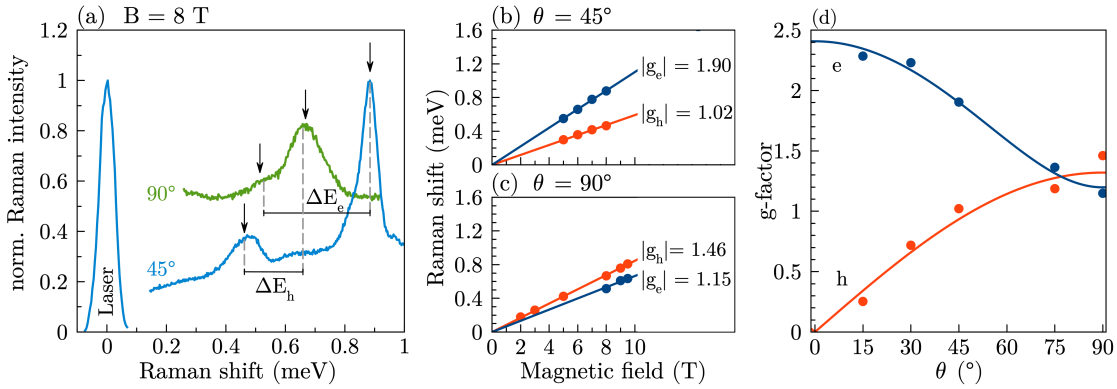

Figure A6: (a) SFRS spectra for $(PEA)_2MA_4Pb_5I_{16}$ ($n = 5$) in tilted magnetic field ($\theta = 45°$, blue) and Voigt geometry ($\theta = 90°$, green) excited with $E_{exc} = 1.814$ eV and $P = 0.6$ W/cm^2. (b, c) Raman shifts of the SFs lines in magnetic field for electron and hole in tilted field (b) and Voigt geometry (c). The fit to linear functions (solid lines) allow to determine the carrier g-factors. (d) g-factor anisotropies fitted with Equation 3.12.

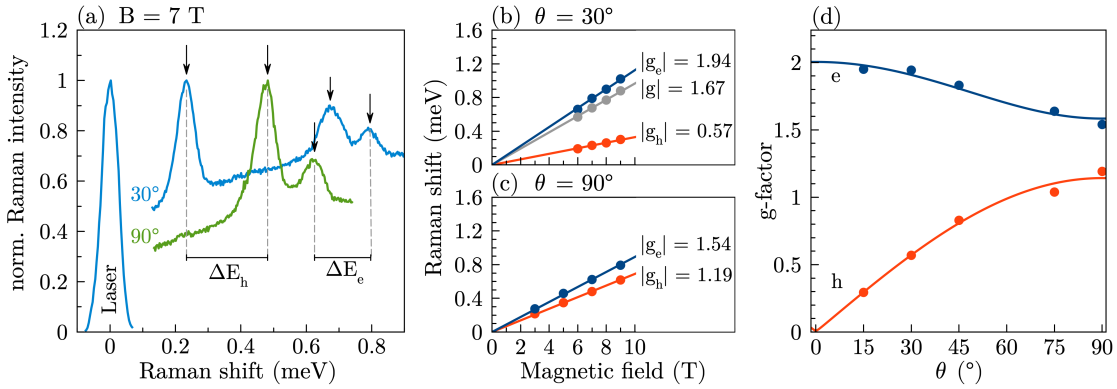

Figure A7: (a) SFRS spectra for $(PEA)_2MA_5Pb_6I_{19}$ ($n = 6$) in tilted magnetic field ($\theta = 30°$, blue) and Voigt geometry ($\theta = 90°$, green) excited with $E_{exc} = 1.798$ eV and $P = 0.6$ W/cm^2. (b, c) Raman shifts of the SFs lines in magnetic field for electron and hole in tilted field (b) and Voigt geometry (c). The fit to linear functions (solid lines) allow to determine the carrier g-factors. (d) g-factor anisotropies fitted with Equation 3.12.

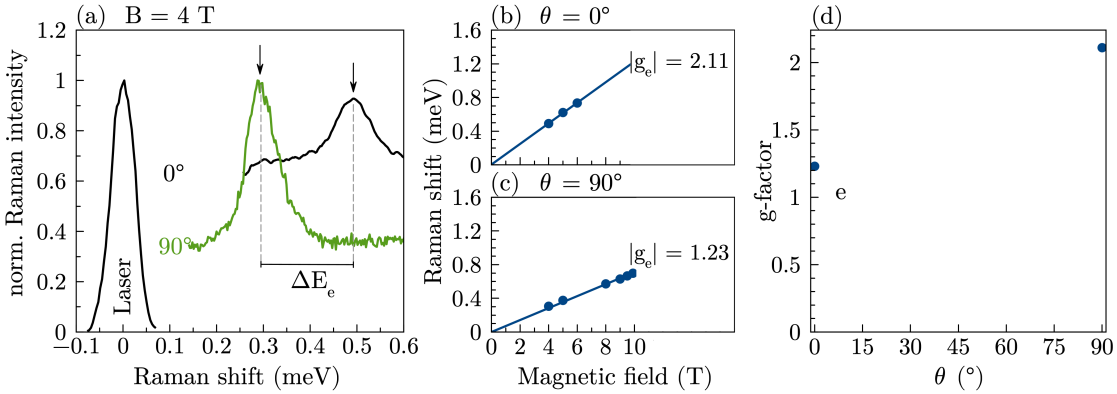

Figure A8: (a) SFRS spectra for $(PEA)_2MA_6Pb_7I_{22}$ ($n = 7$) in Faraday ($\theta = 0°$, black) and Voigt geometry ($\theta = 90°$, green) excited with $E_{exc} = 1.789$ eV and $P = 0.6$ W/cm^2. (b, c) Raman shifts of the SFs lines in magnetic field for electron and hole in tilted field (b) and Voigt geometry (c). The fit to linear functions (solid lines) allow to determine the carrier g-factors. (d) g-factor anisotropy.

Acknowledgements

Now, I would like to express my gratitude to everyone who supported me during my work on this thesis. First of all, I thank my supervisor, Dmitri Yakovlev, for giving me the opportunity to work in his research group. Despite his numerous research topics, he always took the time to patiently explain and discuss the next steps in my work. I am also grateful to the other leaders of the E2 chair, Manfred Bayer, Marc Aßmann, Jörg Debus and Ilya Akimov for providing such an exceptional research environment. I appreciate the time and effort Doris Reiter dedicated as the second reviewer of my thesis. A special thanks goes to my other supervisors, Dennis Kudlacik and Natasha Kopteva. Dennis, as my 'lab supervisor', patiently showed me everything in the lab on spin-flip Raman spectroscopy, sharing his knowledge and experience. Natasha, thank you for countless discussions in the office and your insights into physics. I will never forget the shared excitement we experienced when unraveling the 'phonon story'. I am also grateful for the opportunity to collaborate on joint projects with Erik Kirstein, Evgeny Zhukov, and Ina Kalithuka, as well as the time spent in the lab with Marek Karzel, Ina Kalithuka, Mariam Harati, Juliane Rütter, and Simon Siegeroth. Together, we shared countless hours in the darkness and noise of Lab C. I extend my gratitude to our theory colleague, Misha Nestoklon, for his support on phonons in perovskite nanocrystals. I would like to thank Stefan Grisard for insightful discussions that contributed to the development of the model presented in Chapter 3. Many thanks to Lars Wieschollek and Daniel Tüttmann for consistently providing me with helium. Further thanks to Lars Wieschollek for answering my questions regarding the experimental equipment and to Michaela Wäscher for her administrative support. I thank all my E2 colleagues for the friendly environment. Here, I would like to thank particularly Lars Klompmaker, who supervised my Bachelor's thesis and first introduced me to the E2 chair, Alex Hollberg as my temporary office colleague, and to everyone in office CP-01-184 for the good times and support before my defense. I am also grateful to everyone who helped me proofreading this thesis, including Stefan Grisard, Natasha Kopteva, Dennis Kudlacik, Alex Hollberg, and Andreas Farenbruch. To my friends I met during my studies and beyond, thank you! Monday evenings were always the highlight of the week, thanks to the dancing lessons together with Stefan Grisard, Rilana, and Sebastian Pape-Reichhardt. Above all, I want to thank my parents, Bettina and Rainer, for their unconditional support in my life. Finally, and most importantly, my fiancé Stefan, whom I met during my bachelor studies and who has been by my side ever since. You have always believed in me and supported me during my PhD.

Eidesstattliche Versicherung

Ich versichere hiermit an Eides statt, dass ich die vorliegende Dissertation mit dem Titel „The Effect of Quantum Confinement on the Spin Properties of Lead Halide Perovskites Probed by Resonant Raman Spectroscopy“selbstständig und ohne unzulässige fremde Hilfe erbracht habe. Ich habe keine anderen als die angegebenen Quellen und Hilfsmittel benutzt, sowie wörtliche und sinngemäße Zitate kenntlich gemacht. Die Arbeit hat in gleicher oder ähnlicher Form noch keiner Prüfungsbehörde vorgelegen.

Ort, Datum | Unterschrift

Belehrung

Wer vorsätzlich gegen eine die Täuschung über Prüfungsleistungen betreffende Regelung einer Hochschulprüfungsordnung verstößt, handelt ordnungswidrig. Die Ordnungswidrigkeit kann mit einer Geldbuße von bis zu 50 000 € geahndet werden. Zuständige Verwaltungsbehörde für die Verfolgung und Ahndung von Ordnungswidrigkeiten ist der Kanzler/die Kanzlerin der Technischen Universität Dortmund. Im Falle eines mehrfachen oder sonstigen schwerwiegenden Täuschungsversuches kann der Prüfling zudem exmatrikuliert werden (§ 63 Abs. 5 Hochschulgesetz).

Die Abgabe einer falschen Versicherung an Eides statt wird mit Freiheitsstrafe bis zu 3 Jahren oder mit Geldstrafe bestraft.

Die Technische Universität Dortmund wird ggf. elektronische Vergleichswerkzeuge (wie z. B. die Software „turnitin“) zur Überprüfung von Ordnungswidrigkeiten in Prüfungsverfahren nutzen.

Die oben stehende Belehrung habe ich zur Kenntnis genommen.

Ort, Datum | Unterschrift